

(1967).

<sup>2</sup>P. R. Fields, R. F. Barnes, R. K. Sjoblom, and J. Milsted, *Phys. Letters* **24B**, 340 (1967).<sup>3</sup>P. G. Steward, University of California Lawrence Radiation Laboratory Report No. UCRL-18127, 1968 (unpublished).<sup>4</sup>K. S. Toth, R. L. Hahn, M. A. Ijaz, and W. M. Sample, *Phys. Rev. C* **2**, 1480 (1970).<sup>5</sup>T. Sikkeland, A. Ghiorso, and M. J. Nurmia, *Phys. Rev.* **172**, 1232 (1968).<sup>6</sup>G. R. Choppin, B. G. Harvey, and S. G. Thompson, *J. Inorg. Nucl. Chem.* **2**, 66 (1956).<sup>7</sup>A. Ghiorso and T. Sikkeland, *Phys. Today* **20**, 25 (1967).<sup>8</sup>V. E. Viola and G. T. Seaborg, *J. Inorg. Nucl. Chem.* **28**, 697 (1966).<sup>9</sup>E. K. Hyde, I. Perlman, and G. T. Seaborg, *The Nuclear Properties of the Heavy Elements* (Prentice-Hall, Englewood Cliffs, New Jersey, 1964), Vol. I, pp. 120 and 268.<sup>10</sup>O. Nathan and S. G. Nilsson, in *Alpha-, Beta-, and Gamma-Ray Spectroscopy*, edited by K. Siegbahn (North-Holland Publishing Company, Amsterdam, The Netherlands, 1965), Chap. X.<sup>11</sup>J. O. Rasmussen and C. J. Gallagher, *J. Inorg. Nucl. Chem.* **3**, 333 (1957). Normalized to fit half-lives of known even-even  $\alpha$  emitters in this region.

PHYSICAL REVIEW C

VOLUME 2, NUMBER 5

NOVEMBER 1970

## Average-Resonance Method of Neutron-Capture $\gamma$ -Ray Spectroscopy: States of $^{106}\text{Pd}$ , $^{156}\text{Gd}$ , $^{158}\text{Gd}$ , $^{166}\text{Ho}$ , and $^{168}\text{Er}$ †

L. M. Bollinger and G. E. Thomas  
*Argonne National Laboratory, Argonne, Illinois 60439*  
(Received 22 June 1970)

The average-resonance method of neutron-capture  $\gamma$ -ray spectroscopy is critically examined by means of measurements on stable isotopes of palladium, gadolinium, holmium, and erbium. A mathematical model of the capture process is developed. This model shows that the intensities of the lines in average-resonance-capture spectra can yield the parities and set narrow limits on the spins of states in almost all nuclides with  $A > 100$  if the  $\gamma$ -ray strength function is a smooth function of  $\gamma$ -ray energy and if the random fluctuations in intensity result only from the Porter-Thomas distribution of partial radiation widths. The measurements give extensive data for  $^{106}\text{Pd}$ ,  $^{156}\text{Gd}$ ,  $^{158}\text{Gd}$ ,  $^{166}\text{Ho}$ , and  $^{168}\text{Er}$ , and some for  $^{103}\text{Pd}$ ,  $^{105}\text{Pd}$ ,  $^{155}\text{Gd}$ ,  $^{157}\text{Gd}$ ,  $^{165}\text{Er}$ ,  $^{167}\text{Er}$ , and  $^{169}\text{Er}$ . These data are examined for information relating to the mechanisms of radiative capture. All of the data are consistent with the hypothesis that the radiation widths are a smooth function of  $\gamma$ -ray energy and that the random fluctuations in intensity are well described by the Porter-Thomas distribution. The intensities of  $E1$  transitions vary with  $\gamma$ -ray energy more rapidly than  $E_{\gamma}^3$ , as expected from a giant-resonance description of the radiative process. The intensity of  $M1$  radiation was measured over a 2-MeV range for  $^{106}\text{Pd}$  and  $^{168}\text{Er}$ , and the reduced  $M1$  widths for  $^{106}\text{Pd}$  form a giant-resonance-like curve that peaks at  $\sim 7.8$  MeV. Ratios of widths for  $E1$  and  $M1$  radiation and for  $E1$  and  $E2$  radiation are obtained for several nuclides. These properties of radiative capture are used to obtain spectroscopic information about final states. The most complete results are for  $^{166}\text{Ho}$ , for which 16 rotational bands are identified and interpreted in terms of the collective model. Similar but less extensive data are obtained for  $^{156}\text{Gd}$ ,  $^{158}\text{Gd}$ , and  $^{168}\text{Er}$ . The measurements on  $^{106}\text{Pd}$  show that the shapes of the observed  $\gamma$ -ray lines may be used to determine the parities of final states.

### I. INTRODUCTION

Spectroscopic information about low-energy nuclear energy levels has been obtained from neutron-capture  $\gamma$  rays for many years. Thermal-neutron-capture spectra<sup>1,2</sup> have been most widely used in this way, and recently the spectra from capture in individual neutron resonances<sup>3,4</sup> have also become important. The most reliable data obtainable from these spectra are the *energies* of low-energy states, since the high-energy  $\gamma$ -ray lines in the spectra are formed by transitions from the initial

capture state directly to the final state of interest. Thus, the energy of the final state is just equal to the difference between the initial excitation energy and the transition energy of the observed  $\gamma$ -ray line. Usually, only  $E1$  and  $M1$  transitions are strong enough to be observable.

The *intensities* of high-energy radiative transitions have also been used to determine the parities of the final states under the assumption that  $E1$  transitions are much stronger than  $M1$  transitions. However, heretofore this approach has not been very effective, because the width of a primary ra-

diative transition from a highly excited state is a random variable with a very broad distribution, namely, the Porter-Thomas<sup>5</sup> distribution. Thus, the intensity associated with a single initial state (or an arbitrary excitation energy such as results from thermal-neutron capture) usually does not give an unambiguous indication of the nature of the radiation. Only when the transition is abnormally strong can one conclude with assurance that the transition is  $E1$  in character.

In principle, the uncertainty caused by random fluctuations can be eliminated by measuring the  $\gamma$ -ray spectra for many individual resonances that are selected by means of a neutron spectrometer. However, for many nuclides the neutron sources now in use are not strong enough that the measurement of the requisite number of spectra is feasible. For example, consider the typical nucleus in which the average width for  $E1$  transitions is five times the average width for  $M1$  transitions, and assume that spectra are measured for six resonances. Then, if  $E1$  and  $M1$  transitions are equally probable, only 13% of the  $M1$  transitions and 82% of the  $E1$  transitions can be identified with greater than 90% confidence from the measured widths.<sup>6</sup>

In the work reported here, we have bypassed the difficulty caused by Porter-Thomas fluctuations by direct measurement of the *average*  $\gamma$ -ray spectrum that results when neutrons in a relatively broad

band of energy are captured in many resonances. For convenience, we will term the spectrum from average-resonance capture an  $(\bar{n}, \gamma)$  spectrum. The basic ideas of the measurement have been outlined in earlier publications<sup>7,8</sup> and will be reviewed in Sec. II.

The primary purpose of this paper is to examine critically the capabilities and limitations of the  $(\bar{n}, \gamma)$  method as a technique of nuclear spectroscopy. For this reason, the technical aspects of the measurements and the interpretation of the spectra are emphasized, rather than the interpretation of the energy levels observed. Since measurements have been made on a very large number of nuclides, this paper will be the first of a series.

## II. EXPERIMENTAL APPARATUS AND PROCEDURES

Our  $(\bar{n}, \gamma)$  spectra are obtained by using a high-resolution Ge(Li) spectrometer to measure the capture  $\gamma$  rays emitted by a sample that is surrounded by <sup>10</sup>B and placed in a high-flux region of a nuclear reactor. The boron selectively removes low-energy neutrons, and the  $1/E$  spectrum of the incident neutron flux assures a low intensity of energetic neutrons. The combination limits the energies of the neutrons captured in the sample to a band that is broad enough to contain many resonances but

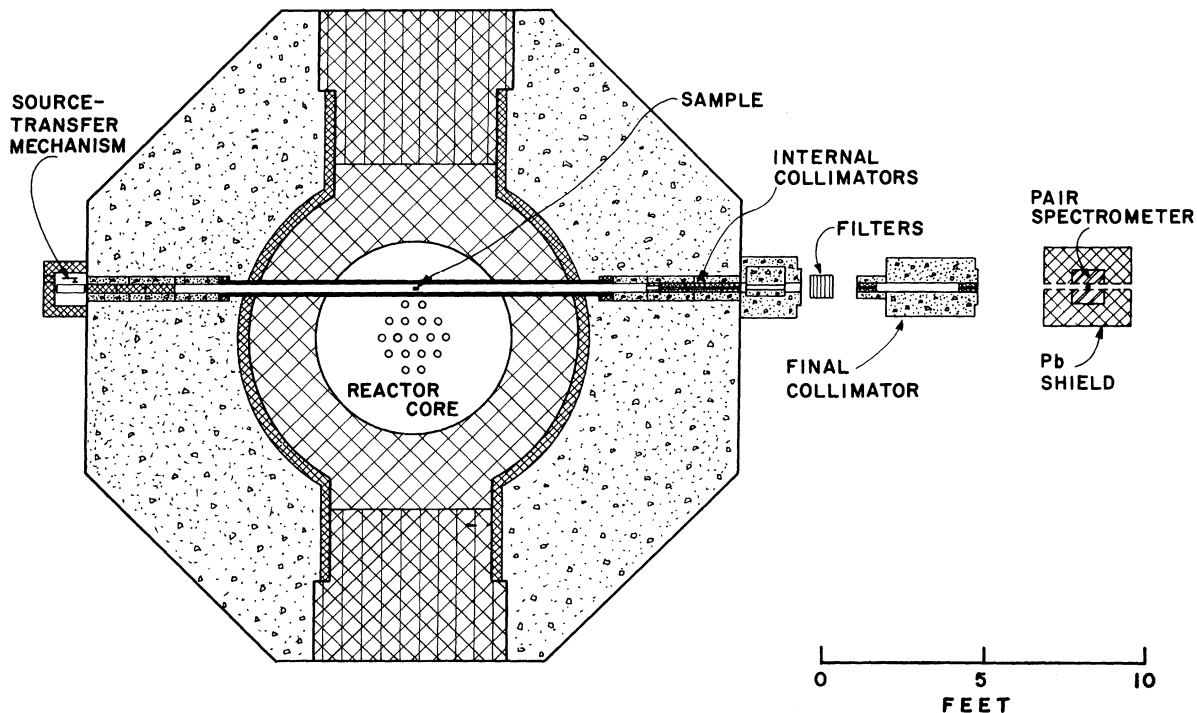


FIG. 1. Schematic view of the internal-target facility (Ref. 9) at the reactor CP-5. At the sample position, the thermal-neutron flux is  $3 \times 10^{13}$  neutron  $\text{cm}^{-2} \text{sec}^{-1}$  and the Cd ratio for a gold foil is 7.

narrow enough to preserve the excellent resolution of the Ge(Li) detector and low enough in energy to restrict the capture process to  $s$ -wave and perhaps  $p$ -wave interactions.

The experimental system used in the measurement of  $(\bar{n}, \gamma)$  spectra is an internal-target facility (Fig. 1) at the reactor CP-5. The boron-surrounded sample being studied is placed in the center of a 4.5-in.-diam aluminum tube that passes through the reactor tangent to the core. At this sample position there is a relatively high flux of both thermal neutrons and epithermal neutrons with a  $1/E$  energy spectrum.  $\gamma$  rays from the sample stream out of the reactor to a Ge(Li)  $\gamma$ -ray spectrometer located about 20 ft from the sample. A refined collimation system ensures that the Ge(Li) detector views the sample of interest but not the walls of the through tube in which it is mounted.

The internal-target facility used in our measurements has been described previously by Thomas, Blatchley, and Bollinger (TBB),<sup>9</sup> but many of the components and characteristics of the system have had to be improved in order to make it possible to measure average-resonance-capture spectra of the desired quality.

**Detector system.** The most important changes have been in the  $\gamma$ -ray spectrometer<sup>10</sup> and its associated electronics. The improved detection system is the annihilation-pair spectrometer shown in Fig. 2. Here we use a Ge(Li) detector whose size (4.5 cm long  $\times$  1.2 cm  $\times$  1.2 cm) is designed to give optimum efficiency both for detection of the incoming  $\gamma$  ray and for escape of the 511-keV annihilation

quanta. This Ge(Li) detector is placed in the center of a large annular NaI(Tl) scintillator with a 5.8-cm i.d., a 25-cm o.d., and 30.5-cm length. The annulus is split into four optically independent quadrants. An event is stored in the pulse-height analyzer only when there is a threefold coincidence between pulses in the Ge(Li) detector and in two opposite quadrants of the NaI annulus. The over-all efficiency for detecting the pair of annihilation quanta is  $\sim 30\%$ . The detection system may also be used as an anticoincidence spectrometer, but this mode of operation was not used in this investigation.

The electronic system (Fig. 3) used for the detector pulses is based on the high-counting-rate circuits developed by Strauss *et al.*<sup>11</sup> This system has a low-noise cooled field-effect transistor (FET) preamplifier followed by a main amplifier with a maximum gain of 20. There is a continuous gain control and a zero adjustment on the linear gate, so that any portion of the spectrum can be studied in detail. Before acceptance, each pulse is sent through a pulse-shape discriminator circuit that rejects pulses whose shape is distorted by pileup or by edge effects in the detector. These special features allow the system to be used at very high counting rates without a degradation of the resolution function. In our measurements the singles counting rate in the Ge(Li) detector is typically 10 000/sec.

Pulses from the NaI detectors are treated with conventional circuits. Single-channel analyzers are used to require that the pulses from the anni-

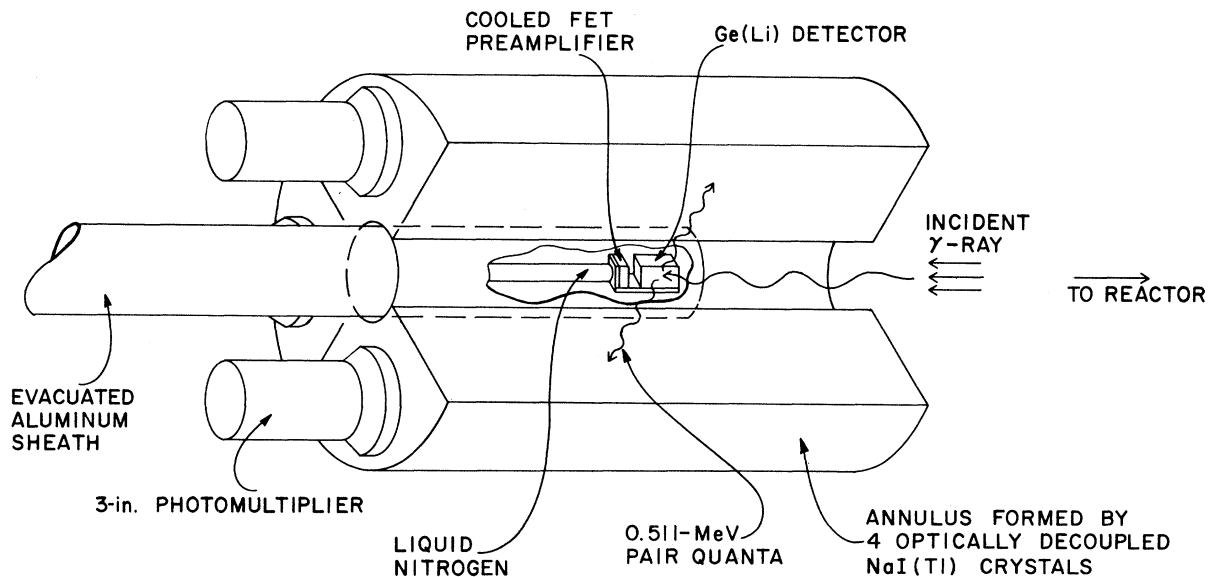


FIG. 2. The annihilation-pair spectrometer. The detector assembly is shielded from room background by 9 in. of lead, 1 in. of  $B_4C$ , and 6 in. of borated polyethylene.

hilation quanta are of approximately full size; this requirement improves the signal-to-background ratio. The requirement of a threefold coincidence removes more background and has the added advantage of reducing dead-time losses in the 4096-channel pulse-height analyzer.

Both the zero level and the gain of the analog-to-digital converter (ADC) are stabilized on pulses from a precision pulser developed by Strauss *et al.*<sup>12</sup> The ADC runs continuously so that it is stabilized even while data are being read out of the analyzer. Also, pulses from the precision pulser are stored in the analyzer to help determine if the analyzer is operating properly.

The data stored in the analyzer are read out on paper tape. A fast plotter is also available.

*Sample heating.* A troublesome practical difficulty in our resonance-capture measurements has been the nuclear heating of the sample and its surroundings. The liner of the through tube in the reactor originally heated to a temperature of about 450°C. This problem has been eliminated by cooling the liner to room temperature by means of a water jacket.

Even when placed within the cooled liner, however, the sample itself can become very hot because of the heat released by the ( $n, \alpha$ ) reaction in the  $^{10}\text{B}$  absorber. Consequently, the temperature of the sample material is typically about 700°C. This high temperature creates special difficulties in the study of materials with low melting points; some materials have been studied in the liquid state. If necessary, however, the sample can be

cooled to  $\sim 100^\circ\text{C}$  by placing it in close thermal contact with the cooled liner.

*Background radiations.* A bothersome source of background counts was eliminated by a refinement of the collimation system. In the spectra given in Ref. 9 one sees a large hump with a maximum intensity at about 7.7 MeV. This hump was probably caused by the small-angle Compton scattering in the original collimator of the 7.72-MeV  $\gamma$  ray from neutron capture in the aluminum wall of the through tube. In any case, the hump disappeared when the original lead collimator was shielded from this radiation by means of a long tapered graphite collimator placed between the sample and the lead collimator. The graphite collimator is shaped so that no part of it is visible to the detector.

Another kind of background that was eliminated by the improvement in the experimental system consists of the many lines from Fe, Cr, etc., that were present in the early measurements described in Ref. 9. This improvement probably resulted from the addition of massive shielding that eliminates neutrons from the neighborhood of the detector.

The principal background lines that remain are those from the sample holder and absorber, namely, lines from capture in  $^{12}\text{C}$  and  $^{10}\text{B}$ . Also, there are a few weak lines from small impurities of Cu and Ni in the boron absorber and from  $^{13}\text{C}$  in the sample holder; and the ground-state transition in  $^{28}\text{Al}$  is weakly present, probably as the result of elastic scattering in the sample of capture  $\gamma$  rays from the aluminum wall of the through tube. In

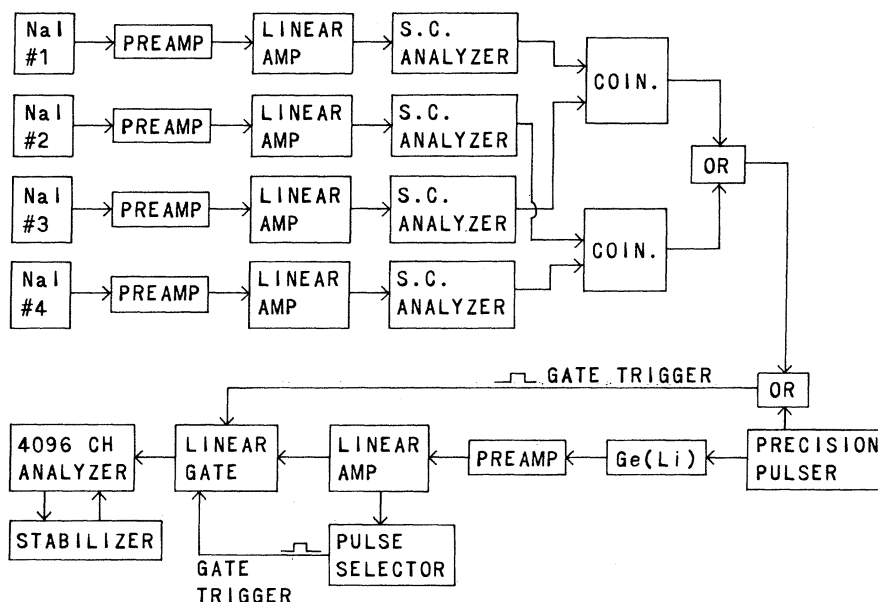


FIG. 3. Block diagram of the electronic system for the detector.

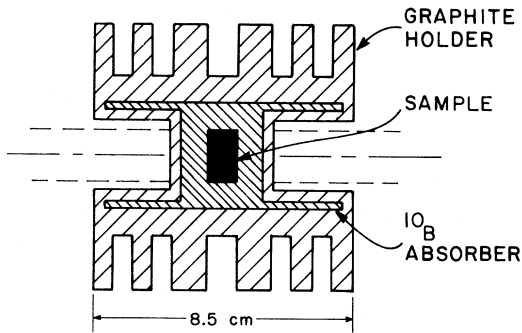


FIG. 4. Representative sample holder. The  $^{10}\text{B}$  is in the form of amorphous boron powder and the graphite is reactor-grade material. The coaxial volume visible at the detector is shown by the dashed lines.

addition, some spectra have weak capture- $\gamma$ -ray lines from nitrogen (when the helium gas-flow system of the through tube malfunctions), from Fe (presumably because of an excessive room background of thermal neutrons released occasionally at a neighboring experiment), and from Cl (presumably from perspiration deposited on the walls of the sample during its preparation).

The capture of thermal neutrons in the surface of the  $^{10}\text{B}$  absorber generates intense lines (especially at 478 keV) and to minimize these it is desirable to use samples with the shape shown in Fig. 4. Here the function of the cylinders of  $^{10}\text{B}$  that extend out from the main body of the absorber is to minimize the flux of the thermal neutrons striking the surfaces that are visible to the detector. The purpose of the grooved enclosure of graphite surrounding the sample is to make a large surface area from which the heat can be re-

moved by convection of the helium gas filling the through tube.

In spite of the special shape of the sample, the intensity of the 478-keV  $\gamma$  ray from the  $^{10}\text{B}(n, \alpha)$  reaction is so great that it must be greatly reduced by placing  $\gamma$ -ray absorbers in the beam at the position shown in Fig. 1. Typically, the absorber is 0.9 cm of thorium and 20 cm of borated polyethylene. The polyethylene is also used to reduce the intensity of neutrons (especially fast neutrons) incident on the detector.

A representative  $(\bar{n}, \gamma)$  spectrum obtained in the way outlined above is given in Fig. 5. For these data, the sample was normal palladium metal and the absorber thickness was  $0.63 \text{ g/cm}^2$  of  $^{10}\text{B}$ . The spectrum was accumulated in a running time of 86 h. Even though the sample consisted of several isotopes, the statistical accuracy is seen to be excellent for the strong lines. The background is very small at high energies, but it starts to increase at  $\gamma$ -ray energies less than about 7.6 MeV. This increase is probably caused by small-angle Compton scattering (in the sample) of  $\gamma$  rays from capture in the aluminum walls of the through tube. The background is also enhanced at low energies by the tails of the lines in the spectrum, particularly the tails formed by the escape of bremsstrahlung from the detector.

*Calibration.* In an analysis of an  $(\bar{n}, \gamma)$  spectrum, one is most interested in two quantities - the energies and the intensities of the  $\gamma$ -ray lines. In our work the standard for both of these is the reaction  $^{14}\text{N}(n, \gamma)^{15}\text{N}$ . Typically, a spectrum for this reference reaction was measured just before or just after each sample run by filling the through tube with nitrogen gas in place of the helium that is normally

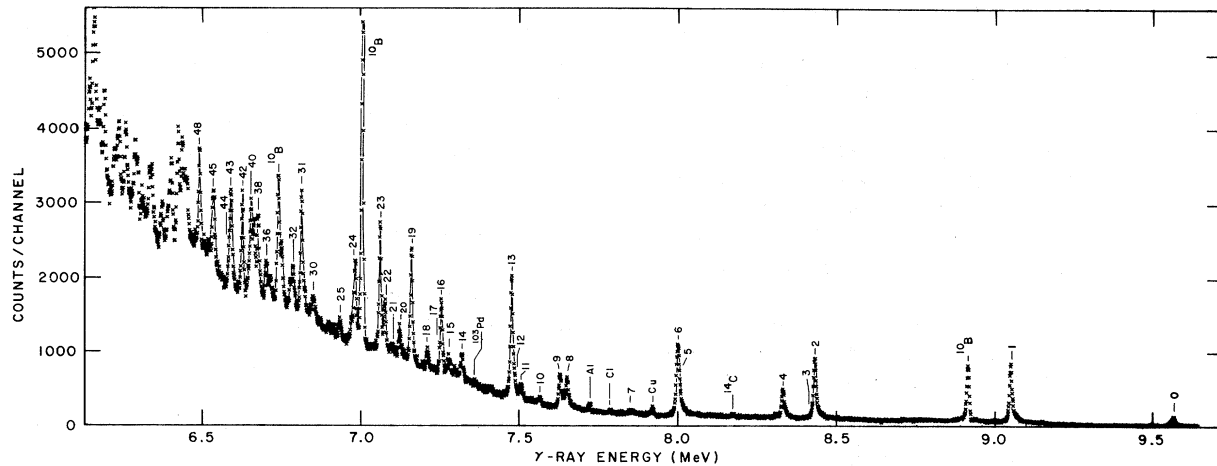


FIG. 5. Average-resonance-capture spectrum for palladium. Most of the lines above 6.9 MeV result from the reaction  $^{105}\text{Pd}(n, \gamma)^{106}\text{Pd}$ . The line numbers are the same as those used in Tables XIV and XV. The background lines mentioned in the text are labeled.

used. Since the zero-level displacement and the gain of the electronic system are continuously stabilized on the precision pulser, they are accurately the same for the nitrogen and sample spectra. The energy calibration of the detector system was established by using the nitrogen-line energies reported by Greenwood.<sup>13</sup> Uncertainties in measured energies are discussed in Sec. IV I.

The efficiency of the detector system, including the effect of the absorbers in the  $\gamma$ -ray beam, was determined from the measured intensities of the  $^{14}\text{N}(\bar{n}, \gamma)$  lines by using the absolute intensities given by TBB.<sup>9</sup>

*Determination of energies and intensities.* The intensities and energies of  $\gamma$  rays in the measured spectra were obtained by the old-fashioned method of unpeeling the individual lines by visually fitting known line shapes to the observed peaks. The first step in the analysis is to determine the background level by drawing a smooth curve through the measured intensities in regions between  $\gamma$ -ray lines, making allowance for the influence of the tails of nearby lines when necessary. Then the corrected intensity (measured intensity minus background) is plotted by machine on semilogarithmic paper. And finally, this corrected spectrum is fitted by reference lines whose shape is determined from a few well-isolated lines in the spectrum of interest. When necessary, the width of the reference line is varied slowly with  $\gamma$ -ray energy, and different classes of lines are allowed to have different shapes. This rather primitive procedure was adopted in this first major investigation of average-resonance-capture spectra in order to develop a thorough understanding of the kinds of problems involved in the analysis.

For our needs, at least, the only drawback of the unpeeling procedure (in comparison, for example, with a least-squares fit carried out by a digital computer) is that our estimates of error are somewhat subjective. However, this is not serious since the errors obtained from a more refined calculation often are not very meaningful because of systematic uncertainties in the background level or line shape. Also, an accurate knowledge of the experimental error in intensity is usually unimportant because the Porter-Thomas fluctuations are larger.

The time required to unpeel a complex spectrum is not excessive; indeed, it is often less than the time expended in the various steps involved in a machine fit.

### III. ANALYSIS OF SPECTRA

#### A. Neutron-Capture Spectrum

The main objective of this paper is to show how

the *intensities* and the *shapes* of the  $\gamma$ -ray lines in average-resonance-capture spectra may be used to obtain spectroscopic information about low-energy nuclear states. For this purpose we need to have at least a qualitative understanding of how these  $(\bar{n}, \gamma)$  spectra are formed. Let us start by writing down a general relationship for the intensity  $\gamma_{ij}(E_n)$  of primary transitions to a final state  $j$  from a band of initial states  $i$  of spin  $J_i$  formed by capture of neutrons incident with energy  $E_n$ .

In order to reduce the number of geometrical variables, we will assume that the neutrons incident on the  $^{10}\text{B}$  absorber arrive with equal intensity from all directions. Also, in the energy range with which we are concerned, the neutron intensity may be assumed to vary as  $E_n^{-1}$ . Then the  $\gamma$ -ray intensity is

$$\gamma_{ij}(E_n) = k \epsilon_\gamma \rho_i \frac{\bar{\Gamma}_{ij}}{\Gamma_\gamma} E_n^{-1} \iiint TK \sin \theta d\theta dx dy, \quad (1)$$

where  $k$  is a constant,  $\epsilon_\gamma$  is the over-all efficiency of the detection system,  $\rho_i$  is the density of states at the initial state  $i$ ,  $\bar{\Gamma}_{ij}$  is the average value of the radiation width for the transition  $i-j$ ,  $\Gamma_\gamma$  is the total radiation width of the initial state,  $T$  is the neutron transmission of the absorber, and  $\rho_i K$  is the average probability that a neutron incident on the sample is captured. The quantities  $T$  and  $K$  are both functions of  $E_n$  and of the three variables  $\theta$ ,  $x$ , and  $y$  that define the path of the incident neutron, where  $\theta$  is the angle relative to the axis of the sample and  $x$  and  $y$  are the coordinates of the point at which the neutron path crosses the mid-plane.

In principle, Eq. (1) can be evaluated in a straightforward way by means of numerical calculations. However, because of the geometrical complexity of the sample relative to the incident neutrons, this calculation is fairly involved and it has not been done. Instead, we have attempted to understand the essential features of the average-capture spectrum by making various simplifying assumptions. Let us start with the assumption that the paths of all incident neutrons pass through the center of the sample. Also, assume that the capture probability  $K(\theta, x, y, E_n)$  may be removed from the integral and replaced by an effective value  $\bar{C}(E_n)$  corresponding to an average sample thickness  $\bar{n}$  and an average over the distribution of neutron widths. Then Eq. (1) becomes

$$\gamma_{ij}(\bar{E}_n) \approx k \epsilon_\gamma \frac{\bar{\Gamma}_{ij}}{\Gamma_\gamma} \rho_i E_n^{-1} \bar{C}(E_n) \int_\theta T(\theta, E_n) \sin \theta d\theta, \quad (2a)$$

$$\propto (\bar{C} \bar{T} / \Gamma_\gamma E_n) \langle \Gamma_{ij} / D_i \rangle, \quad (2b)$$

where  $\bar{T}$  is the average transmission of the absorber-

er and  $D_i \equiv \rho_i^{-1}$  is the average level spacing at the initial state. Here we see one of the essential features of an average-resonance-capture spectrum – through  $\bar{C}/\Gamma_\gamma$  the average intensity depends on the parameters of the capturing resonances, but it does not depend directly on the partial radiation width; rather it depends on the  $\gamma$ -ray strength function  $\langle \Gamma_{i\gamma}/D_i \rangle$ , a ratio that may be expected to exhibit a fairly regular behavior.

The integral in Eq. (2a) has been solved numerically under the simplifying assumptions given above, but otherwise with the geometrical intricacies of the  $^{10}\text{B}$  absorber taken into account. The average transmission  $\bar{T}$  obtained for an absorber  $0.47\text{-g/cm}^2$  thick is given in Fig. 6(a); and  $\bar{T}/E_n$ , the spectrum of neutrons transmitted to the inner sample, is given in Fig. 6(b). Note that, since the absorption cross section of  $^{10}\text{B}$  varies as  $E_n^{-1/2}$ , these curves of  $\bar{T}$  and  $\bar{T}E_n^{-1}$  may be used for any

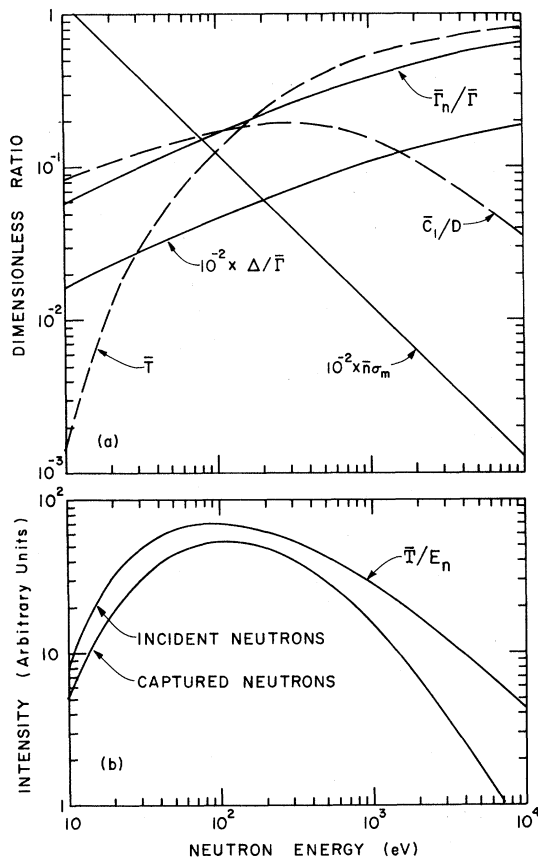


FIG. 6. Various quantities involved in calculating a neutron-capture spectrum. The parameters used to obtain these results are those for a holmium sample with  $D = 10.2$  eV,  $g = \frac{1}{2}$ ,  $\Gamma_\gamma = 0.085$  eV,  $S_0 = 1.6 \times 10^{-4}$ ,  $\theta = 1000^\circ\text{K}$ ,  $\bar{n}\sigma_p = 0.5$ ,  $\bar{n} = 0.030 \times 10^{24}$  atoms/cm $^2$ , and an absorber thickness of  $0.47$  g/cm $^2$  of  $^{10}\text{B}$ . For these parameters, Eqs. (9) and (10) give almost the same neutron-capture spectra.

absorber thickness (neglecting scattering) if the energy scale is multiplied by the factor  $(t/0.47)^2$ , where  $t$  is the thickness of  $^{10}\text{B}$  in g/cm $^2$ .

The quantity  $\bar{C}$  in Eq. (2) is closely related to the transmission-dip area  $A_E$  that is widely used in neutron-resonance analysis; indeed,  $\bar{C}$  might well be called the “capture area” of a resonance. A general relationship for the part of  $C$  that is associated with the first interaction of the incident neutron is

$$C_1 \approx \int (1 - e^{-\bar{n}\sigma}) \frac{\sigma_\gamma}{\sigma} dE_n, \quad (3)$$

where  $\sigma_\gamma$  and  $\sigma$  are the capture and total cross sections of a resonance at energy  $E_n$ , and the range of integration covers the full range of neutron energy involved in the average-resonance-capture measurement.

Going on now to consider  $C$  as a whole, a first worry is that multiple scattering in the sample may make the problem too complex to be treated analytically. However, for the heavy nuclides and the neutron-energy range in which we are interested, the energy of the scattered neutron is distributed over a considerable range and, since the average energy lost in scattering is much greater than the resonance width  $\Gamma$  or the Doppler width  $\Delta$ , a neutron scattered in a resonance is rarely captured in the same resonance; also, in many samples most of the scattered neutrons are scattered in an off-resonance region of energy. Consequently, we may proceed by assuming that the spectrum of scattered neutrons is the same as the spectrum of neutrons incident on the sample, and hence that the spectrum of neutrons captured after one or more scatterings is much the same as the spectrum of neutrons captured on the initial interaction. Then the whole capture area  $C$  is satisfactorily given by  $C \approx \nu C_1$ , where  $C_1$  is given by Eq. (3) and  $\nu > 1$  is a constant (independent of  $E_n$ ) that gives the factor by which multiple scattering increases the effective neutron flux incident on the sample.

Fortunately, we may obtain an important simplification in Eq. (3) by assuming that the shape of the resonance cross section is dominated by Doppler broadening due to motion of the target nuclei. This is a realistic approximation since the high temperature of the sample and the relatively high neutron energy in the typical  $(\bar{n}, \gamma)$  measurement cause the Doppler width  $\Delta$  to be about 10 times the total width (as seen in Fig. 6). Thus, the capture area  $C$  may be written as

$$C \approx \nu \Delta \frac{\Gamma_\gamma}{\Gamma_\gamma + \Gamma_n} \int_{-\infty}^{\infty} [1 - T_0 \exp(-\bar{n}\sigma_m e^{-x^2})] \times \frac{\bar{n}\sigma_m e^{-x^2}}{\bar{n}\sigma_m e^{-x^2} + \bar{n}\sigma_p} dx, \quad (4)$$

where  $T_0$  and  $\sigma_p$  are, respectively, the off-resonance transmission and cross section (both assumed to be constant) and  $\Gamma_n$  is the neutron width. The maximum Doppler-broadened cross section  $\sigma_m$  is given by  $\sigma_m = \frac{1}{2}\sqrt{\pi}\sigma_0\Gamma/\Delta$ , where  $\sigma_0$  is the peak cross section without Doppler broadening.<sup>14</sup>

Now Eq. (4) can easily be evaluated in two special cases of interest. First, consider the thin-sample case in which  $\bar{n}\sigma_m \ll 1$  (but  $\bar{n}\sigma_p$  is not necessarily small). Here

$$C \rightarrow \pi^{1/2} \frac{1-T_0}{\sigma_p} \frac{\Gamma_\gamma}{\Gamma} \nu \sigma_m \Delta = \frac{\pi}{2} \frac{1-T_0}{\sigma_p} \nu \sigma_0 \Gamma_\gamma \quad (5)$$

and, from Eq. (2b),

$$\gamma_{ij}(E_n) \propto \sigma_0 \frac{\bar{T}}{E_n} \left\langle \frac{\Gamma_{ij}}{D_i} \right\rangle. \quad (6)$$

Second, consider the thick-sample case in which  $\bar{n}\sigma_m \gg 1$  and  $\bar{n}\sigma_p \gg 1$ . Then, one can show that

$$C \rightarrow 2\nu\Delta \frac{\Gamma_\gamma}{\Gamma} \ln^{1/2} \left( \frac{\sigma_m}{\sigma_p} \right), \quad (7)$$

and

$$\gamma_{ij}(E_n) \propto \frac{\Delta}{\Gamma} \left[ \ln^{1/2} \left( \frac{\sigma_m}{\sigma_p} \right) \right] \frac{\bar{T}}{E_n} \left\langle \frac{\Gamma_{ij}}{D_i} \right\rangle. \quad (8)$$

Figure 7 compares the asymptotic relationships (5) and (7) with the result of a numerical evaluation of the integral in Eq. (4), all three being computed for the representative values  $\bar{n}\sigma_p = 0.5$  and  $\sigma_p = 10$  b. Here one sees that the asymptotic relationships give a good approximation to Eq. (4) when  $\bar{n}\sigma_m \ll 1$  or  $\bar{n}\sigma_m \gg 1$ . Also (although the figure does not illustrate this point), the shape of the curve of  $C_1\Gamma\Gamma_\gamma^{-1}\Delta^{-1}$  versus  $\bar{n}\sigma_m$  does not depend sensitively on  $\bar{n}\sigma_p$ . This is seen most easily from Eqs. (5) and (7) where a decrease of  $\bar{n}\sigma_p$  from 0.5 to 0.05, for example, merely causes the curve of  $C_1\Gamma\Gamma_\gamma^{-1}$

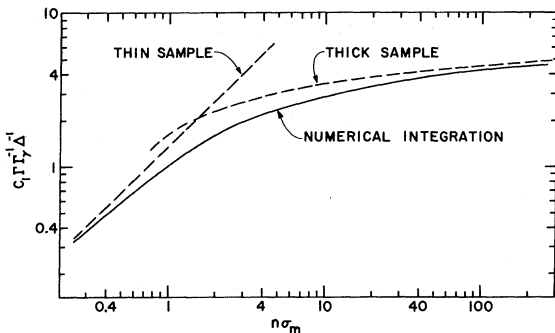


FIG. 7. Comparison between the exact and the asymptotic expressions for the capture area of a resonance. The exact values of  $f(\bar{n}\sigma_m) \equiv C_1\Gamma\Gamma_\gamma^{-1}\Delta^{-1}$  were obtained by numerical integration of Eq. (4). The asymptotic thin-sample and thick-sample curves are plots of Eqs. (5) and (7), respectively. All three curves were calculated for  $\bar{n}\sigma_p = 0.5$ ,  $\sigma_p = 10$  b.

$\times \Delta^{-1}$  to be displaced upward by 24% when  $\bar{n}\sigma_m \ll 1$  and to be displaced to the left by one decade when  $\bar{n}\sigma_m \gg 1$ .

Under the simplifying assumption  $\Delta \gg \Gamma$ , Eq. (2) may be written in the form

$$\gamma_{ij}(E_n) \propto \langle \Delta \Gamma^{-1} f(\bar{n}\sigma_m) \rangle \frac{\bar{T}}{E_n} \left\langle \frac{\Gamma_{ij}}{D_i} \right\rangle, \quad (9)$$

where  $f(\bar{n}\sigma_m) \equiv C_1\Gamma\Gamma_\gamma^{-1}\Delta^{-1}$  is defined by Eq. (4). The quantity  $\Delta \Gamma^{-1} f(\bar{n}\sigma_m)$  is averaged over the distribution of neutron widths, usually a Porter-Thomson distribution.

The neutron-energy-dependent part of Eq. (9) gives the spectrum of captured neutrons. Figure 6(b) shows the capture spectrum for a thick sample of a heavy nuclide with the representative parameters specified in the caption of the figure. The energy dependences of the various ratios of parameters involved in the capture process are given in Fig. 6(a).

One of the most significant things about Fig. 6 is that the spectrum of *captured* neutrons is almost as broad as the spectrum of neutrons *incident* on the sample, even though the energy dependence of  $\sigma_0$  might have been expected to make the capture spectrum much narrower. The reason for this is best seen from Eq. (7). Here  $\Delta \propto E_n^{1/2}$ ,  $\sigma_m \propto E_n^{-1}$  for *s*-wave neutrons, and (when  $\bar{n}\sigma_m \gg 1$ ) the logarithmic term varies so slowly that its change may almost be neglected. Thus, in much of the energy range of interest in our measurements, the average probability  $\bar{C}/D$  of neutron capture in the sample increases with increasing  $E_n$ —in contrast to the decrease that would obtain if  $\Delta \ll \Gamma$ . This effect is shown quantitatively [Fig. 6(a)] by the curve for  $\bar{C}_1/D$ .

The assumption that the resonances have a pure Gaussian shape ( $\Delta \gg \Gamma$ ) causes Eq. (9) to underestimate  $\gamma(E)$ . Numerical calculations show that much better accuracy is achieved by replacing  $\Delta$  by the sum  $(\Delta + \Gamma)$ . Then the expression for  $\gamma(E)$  becomes

$$\gamma_{ij}(E_n) \propto \left\langle \frac{\Delta + \Gamma}{\Gamma} f(\bar{n}\sigma'_m) \right\rangle \frac{\bar{T}}{E_n} \left\langle \frac{\Gamma_{ij}}{D_i} \right\rangle, \quad (10)$$

where  $\sigma'_m = \frac{1}{2}\sqrt{\pi}\sigma_0\Gamma/(\Delta + \Gamma)$ . The accuracy of Eq. (10) may be judged from several numerical examples. Let  $r$  be the ratio of the values of  $\gamma(E)$  calculated from Eq. (10) to those from an exact relationship in which the Gaussian shape is replaced by a Doppler-broadened Breit-Wigner shape. Also, let  $\bar{n}\sigma_0 = 10$  and  $\bar{n}\sigma_p = 0.5$ . Then,  $r = 1.01$  for  $\Delta/\Gamma = 7.4$ ,  $r = 0.94$  for  $\Delta/\Gamma = 1$ , and  $r = 0.59$  for  $\Delta/\Gamma = 0$ ; usually the value of  $r$  decreases with increasing values of  $\bar{n}\sigma_0$ . Thus, since  $\Delta/\Gamma > 1$  in the energy range of interest if  $D < 200$ , Eq. (10) is quite accurate for most heavy nuclides.

Since Eq. (10) will be used extensively in this and following papers, it seems worth while to point out its limitations. As discussed in more detail in the following paragraphs, these result from (a) geometrical approximations, (b) use of samples extending outside the volume viewed by the detector, (c) the assumption that  $\nu$  and  $\sigma_p$  are independent of  $E_n$ , and (d) neglect of the energy correlations for multiply-scattered neutrons.

(a) Often the most important error associated with Eq. (10) is caused by the geometrical approximations that lead to the use of an average sample thickness  $\bar{n}$ . Both the complexity of the shape and the possibility of multiple interactions cause problems. Typically, the geometrical approximations cause an uncertainty of about  $\pm 10\%$  in the width of the neutron-capture spectrum.

(b) The diameter of the sample is often somewhat larger than the diameter of the area viewed by the detector. When this is the case, the outer part of the sample acts as a neutron shield for the inner part from which  $\gamma$  rays are detected. The shielding effect increases with decreasing neutron energy because the maximum cross section  $\sigma_m$  increases with decreasing energy. This effect tends to make the neutron-capture spectrum broader than is calculated with Eq. (10), but the effect is not prominent enough to be easily detected.

(c) The assumption that  $\nu$  and  $\sigma_p$  are independent of neutron energy may not be accurate at low energy, but it is an unimportant source of error for most purposes.

(d) The neglect of correlations in the energies of multiply-scattered neutrons tends to cause Eq. (10) to underestimate  $\gamma(E_n)$ . This effect is important only when the neutron energy lost by scattering is of the same order of magnitude as the resonance width. The effect is unimportant for the even-odd targets studied in this paper, but it may be a significant source of error for the even-even targets that have large values of  $gS_0D$ , where  $S_0$  is the  $s$ -wave neutron strength function and  $g$  is the usual statistical weight factor.

The qualitative reliability of the analysis leading to Eq. (10) may be tested by comparing calculated and measured shapes of  $\gamma$ -ray lines, as illustrated in Fig. 8 for transitions in  $^{196}\text{Pt}$  and  $^{156}\text{Gd}$ . The resonance parameters (based on the tabulations of Goldberg *et al.*<sup>15</sup> and of Seth<sup>16</sup>) and sample properties used in the calculations are given in Tables I and II. Each calculated line shape in Fig. 8 was obtained by convoluting the calculated neutron-capture spectrum with a Gaussian resolution function whose width is inferred from the nearby 7006-keV line produced by thermal-neutron capture in the  $^{10}\text{B}$  absorber, and each curve was normalized to the experimental data in the neighborhood of the

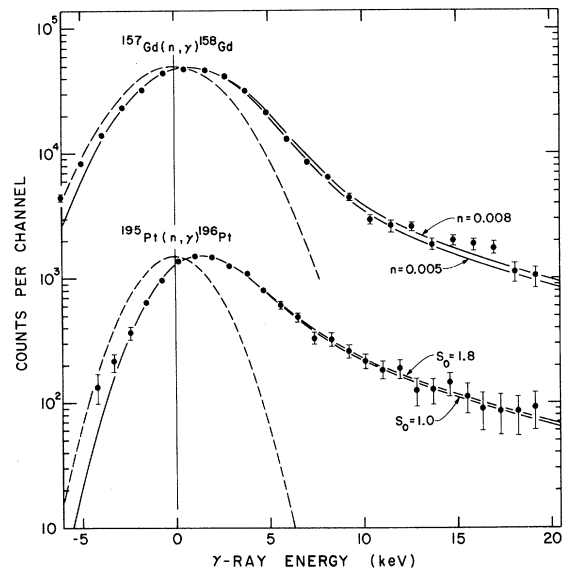


FIG. 8. Comparison between calculated and measured shapes of  $\gamma$ -ray lines. The parameters used are those given for  $^{158}\text{Gd}$  and  $^{196}\text{Pt}$  in Tables I and II, except for the values given on the figure.

peak. Notice that the calculated shape for  $^{196}\text{Pt}$  is quite insensitive to the neutron strength function. This feature obtains for almost all thick samples because, as may be argued from Eqs. (6) and (8),

TABLE I. Neutron-resonance parameters used in calculations of neutron-capture spectra. Most of the values were deduced from Ref. 14, but Ref. 15 was also used as a guide for values of the neutron strength function  $S_0$ . The quantity  $D$  is the average level spacing per spin state, deduced from the low-energy range of data where few resonances are missed. The numbers in parentheses are estimates of the factors by which  $S_0$  and  $D$  are uncertain.

Target nucleus	$10^4 \times S_0$	$D$ (eV)	$\Gamma_\gamma$ (meV)
$^{102}\text{Pd}$	0.5 (1.5)	50 (2)	$150 \pm 20$
$^{104}\text{Pd}$	0.5 (1.5)	100 (2)	$130 \pm 20$
$^{106}\text{Pd}$	0.5 (1.4)	18 (1.3)	$156 \pm 10$
$^{154}\text{Gd}$	2.0 (1.2)	80 (2)	$110 \pm 15$
$^{155}\text{Gd}$	2.6 (1.2)	3.9 (1.1)	$110 \pm 5$
$^{156}\text{Gd}$	2.0 (1.2)	56 (1.4)	$110 \pm 15$
$^{157}\text{Gd}$	2.6 (1.2)	11.0 (1.2)	$97 \pm 5$
$^{164}\text{Er}$	1.5 (1.2) <sup>a</sup>	16 (1.4)	$87 \pm 9$
$^{166}\text{Er}$	1.5 (1.2) <sup>a</sup>	43 (1.3)	$87 \pm 9$
$^{167}\text{Er}$	2.0 (1.2) <sup>a</sup>	6.8 (1.2)	$87 \pm 5$
$^{168}\text{Er}$	1.5 (1.2) <sup>a</sup>	78 (1.4)	$87 \pm 9$
$^{169}\text{Ho}$	1.6 (1.2)	10.2 (1.2)	$85 \pm 5$
$^{195}\text{Pt}$	1.3 (1.3)	24 (1.2)	$110 \pm 5$

<sup>a</sup> Estimates based on the results of H. Liou, Columbia University Report No. NYO-72-190, UC-34 PHYSICS, TID-4500, 1970 (unpublished).

TABLE II. Properties of the samples used in average-resonance-capture measurements.

Sample No.	Material	Weight (g)	Diameter (cm)	Thickness (cm)	Absorber thickness (g/cm <sup>2</sup> <sup>10</sup> B)
1	Ho	12.5	1.31	1.27	0.039
2	Ho	12.7	1.31	1.27	0.111
3	Ho	14.1	1.31	1.27	0.47
4	Er	57.4	2.86	1.00	0.027
5	Er	34.6	2.22	1.00	0.174
6	Er	29.8	2.06	1.01	0.43
7	<sup>164</sup> Er <sub>2</sub> O <sub>3</sub>	1.14	1.27	0.64	0.4
8	Gd	30.5	1.32	2.03	0.48
9	Pd	51.0	2.07	1.27	0.23
10	Pd	25.7	2.07	0.64	0.63

it results from the saturation of  $f(\bar{n}\sigma_m)$  at low energy (where  $\Gamma \approx \Gamma_\gamma$ ) and the saturation of  $\sigma_0$  at high energies (where  $\Gamma \approx \Gamma_n$ ). For the same reasons, the line shape is also insensitive to the value of  $D$ .

The calculation for <sup>156</sup>Gd shows that the line shape is somewhat more sensitive to the sample thickness  $\bar{n}$ . However, the sample dimensions set definite restrictions on the possible range of  $\bar{n}$ .

The experimental and calculated line shapes in Fig. 8 are seen to be in excellent agreement, and the agreement is satisfactory for all other targets studied. Thus, although the detailed shape of the neutron-capture spectrum is obscured by resolution broadening, the agreement between the calculated and measured line shapes shows that the *average* neutron-capture rate at low energy ( $E_n \approx 1$  keV) is correctly calculated relative to the rate at high energy ( $\sim 10$  keV). This result is taken as a demonstration that Eq. (10) is basically sound and that we may use it to deduce various characteristics of the measured  $\gamma$ -ray intensities. The internal consistency of all the other data and calculations presented later in this paper also provide strong support for the reliability of Eq. (10).

#### B. Average Intensity

We are now ready to show how the measured  $\gamma$ -ray intensity depends on the spin and parity of the *final* state. Often the final state may be reached by way of several transition paths, as is shown in Fig. 9 for a representative nucleus. Thus, our first task is to determine the relative intensities of these various possibilities.

Neglecting resolution broadening, we see from Eq. (10) that (for any one of the paths) the average intensity  $I_{ij}$  produced by neutron capture in the energy range  $E_1 - E_2$  is

$$I_{ij} = \int_{E_1}^{E_2} \gamma_{ij}(E_n) dE_n \\ = k\epsilon_\gamma \left\langle \frac{\Gamma_{ij}}{D_i} \right\rangle \int_{E_1}^{E_2} \left\langle \frac{\Delta + \Gamma}{\Gamma} f(\bar{n}\sigma'_m) \right\rangle \frac{\bar{T}}{E_n} dE_n. \quad (11)$$

We now adopt the *working hypothesis* that the high-energy transitions are governed by statistical laws and that the intensities are independent of the details of nuclear structure. In particular, we assume that the  $\gamma$ -ray strength function  $\langle \Gamma_{ij}/D_i \rangle$  is a smoothly-varying function of  $\gamma$ -ray energy and that it is independent of the spins of the initial and final states, although it may depend on the multipolarity and the parity change of the transition. A discussion of the validity of these assumptions is deferred until a later section, since the principal justification for them must come from the data.

Under the above assumptions, all allowed paths for a particular type of transition are equally intense except for the influence of the ratio  $f/\Gamma$ ,

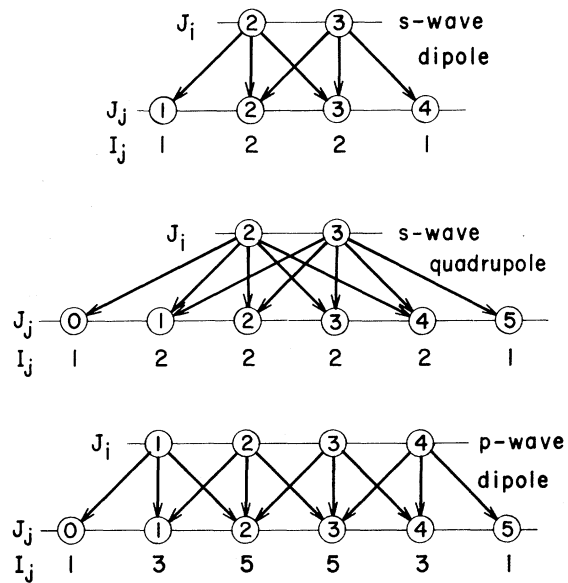


FIG. 9. Decay patterns for <sup>106</sup>Pd. The numbers inside the circles give the spins for initial states  $i$  and final states  $j$ , and the numbers outside give the relative values of the average intensities of transitions to final states with spin  $J_j$ .

which depends on the neutron-resonance parameters. [For simplicity, these arguments refer to Eq. (9) rather than (10).] Let us first consider  $s$ -wave capture under the assumption that the neutron strength function is independent of  $J_i$ , an assumption that implies  $\Gamma_n \propto (2J_i + 1)$ . Then  $\gamma_{ij}$  depends on the character of the initial state only through the factor  $\Gamma^{-1}$  in Eq. (9), since  $\sigma_m \propto \sigma_0 \Gamma$  is independent of  $J_i$ . Two special cases are of interest: (a) for low energies,  $\Gamma_\gamma \gg \Gamma_n$ , so that  $\gamma_{ij} \propto \Gamma_\gamma^{-1} = \text{constant}$ ; and (b) for high energies  $\Gamma_\gamma \ll \Gamma_n$ , so that  $\gamma_{ij} \propto g \propto (2J_i + 1)$ . Thus, since most of the neutrons are captured at energies for which  $\Gamma_\gamma \approx \bar{\Gamma}_n$  in the typical target, the average intensity  $I_{ij}$  is expected to be rather insensitive to  $J_i$ .

The degree of insensitivity may be seen from the following example. Consider a  $^{166}\text{Ho}$  sample with the characteristics of No. 3 of Table II except that the target nucleus has an arbitrary spin  $J_0$ ; and let  $D_i = 10(2J_0 + 1)/(2J_i + 1) \approx 5g^{-1}$ . Then, from Eq. (11) we calculate that the ratio of the  $s$ -wave capture rate in states with  $J_i = J_0 + \frac{1}{2}$  to that in states with  $J_i = J_0 - \frac{1}{2}$  is 1.47, 1.19, 1.12, and 1.07 for  $J_0 = \frac{1}{2}, \frac{3}{2}, \frac{5}{2},$  and  $\frac{7}{2}$ , respectively. As expected from the general argument given above, the example shows that the ratio of capture rates decreases rapidly with increasing  $J_0$ ; and only when  $J_0 = \frac{1}{2}$  is the intensity for initial spin  $J_0 - \frac{1}{2}$  sufficiently different from the intensity for  $J_0 + \frac{1}{2}$  that the difference is easily distinguishable from random errors.

Similar arguments apply to  $p$ -wave neutron capture, but here the characteristic condition is  $n\sigma_m \ll 1$  and  $\Gamma_n \ll \Gamma_\gamma$ . Thus, the neutron-capture rate would be quite independent of  $J_i$  except for the fact that channel-spin considerations cause the neutron widths of the two inner  $J$  values (of the four possible values for targets with spin  $> 1$ ) to be twice as great as they would be otherwise.

The ideas outlined above may now be used to determine the expected patterns of the intensity  $I_j$  of transitions to various final states  $j$ . To a good approximation, when  $J_0 \geq \frac{3}{2}$  the pattern depends only on the number of paths to a given final state—except for  $p$ -wave capture, for which the paths from the inner  $J_i$  values are counted twice. Representative patterns are given in Fig. 9.

Let us conclude this discussion by considering a nucleus with  $J_0 \geq \frac{3}{2}$  for which only  $s$ -wave capture and dipole transitions are significant. Then the above discussion on the intensity  $I_j$  of transitions to a final state  $j$  with spin  $J_j$  may be summarized by the relation

$$I_j \propto \left\langle \frac{\Gamma_{ij}}{D_i} \right\rangle Q_j, \quad (12)$$

where  $Q_j$  is the number of transition paths to the

final state. From theory and previous measurements we expect the strength function  $\langle \Gamma_{ij}/D_i \rangle$  for  $E1$  radiation to be an order of magnitude greater than for  $M1$  radiation. Thus, in a plot of  $I_j$  versus  $E_\gamma$  the points are expected to fall along four smooth curves—one pair for  $E1$  transitions and another pair for  $M1$  transitions, with the curves in each pair being separated in intensity by a factor of 2. One of the main aims of this investigation is to demonstrate that the intensities in  $(\bar{n}, \gamma)$  spectra do in fact obey these simple rules and that this behavior may be used to determine the parities and to set limits on the spins of the final states.

### C. Random Fluctuations in $\gamma$ -Ray Intensity

The patterns of  $\gamma$ -ray intensity discussed above will not be observable, of course, unless the well-known random fluctuations in the intensity of individual transitions can be greatly reduced by averaging over a large enough number of initial states. To estimate the magnitude of the residual fluctuations in an average-resonance-capture spectrum, we start with Eq. (2) and the recognition that  $\bar{C}$  (a function of  $\Gamma_n$ ) and  $\Gamma_{ij}$  are both random variables. Then, by standard statistical methods one can show that the relative variance in the  $\gamma$ -ray intensity  $\gamma_{ij}(E_n)$  produced by neutron capture in an energy interval  $\delta E_n$  at an energy  $E_n$  is

$$\left\langle \left( \frac{\Delta \gamma_{ij}}{\bar{\gamma}_{ij}} \right)^2 \right\rangle = \left[ \left\langle \left( \frac{\Delta \Gamma_{ij}}{\bar{\Gamma}_{ij}} \right)^2 \right\rangle + \left\langle \left( \frac{\Delta C_i}{\bar{C}_i} \right)^2 \right\rangle \right] \left( \frac{D_i}{\delta E_n} \right), \quad (13a)$$

$$= (2 + \mu)(D/\delta E_n). \quad (13b)$$

In Eq. (13b) the ratio  $\delta E_n/D_i$  is simply the number of neutron resonances in the interval  $\delta E_n$ , the factor 2 comes from the assumed Porter-Thomas distribution of the partial radiation widths, and  $\mu \equiv \langle (\Delta C_i/\bar{C}_i)^2 \rangle$  depends in a complicated way on the nuclear and geometrical parameters of the capturing sample. For the special case  $\Gamma_n \ll \Gamma$  and  $\bar{n}\sigma_m \ll 1$ , we have  $\mu \approx 2$ ; and  $\Gamma_n \approx \Gamma$  implies  $\mu \approx 0$ ; and in general,  $0 < \mu < 2$ . For most of our measurements the energy-averaged value  $\bar{\mu} = 0.7$  is not far from the truth.

Now we are ready to write down a relationship for the variance  $\langle (\Delta I_{ij})^2 \rangle$  of the *total* intensity within a broad neutron-energy range  $E_1 - E_2$ . Again, standard methods give

$$\left\langle \left( \frac{\Delta I_{ij}}{I_{ij}} \right)^2 \right\rangle = (2 + \bar{\mu}) D_i \int_{E_1}^{E_2} [\gamma(E_n)]^2 dE_n \times \left[ \int_{E_1}^{E_2} \gamma(E_n) dE_n \right]^{-2}. \quad (14)$$

The integrals in Eq. (14) depend, of course, on the

shape of the spectrum of captured neutrons, which may not be known accurately. Fortunately, however, the ratio of integrals is insensitive to the shape. For example, the ratio for a triangular distribution of  $\gamma(E_n)$  is only  $\frac{4}{3}$  times the ratio for a constant value of  $\gamma(E_n)$ , when the range of integration is over the full width of the triangle.

The essential character of Eq. (14) may be emphasized by letting the lower limit of integration be  $E_1 = 0$  and rewriting the equation in the form

$$\left\langle \left( \frac{\Delta I_{ij}}{I_{ij}} \right)^2 \right\rangle = (2 + \bar{\mu}) \frac{D_{ij}}{w_e} \frac{2}{\nu_e}, \quad (15)$$

where the effective width  $w_e$  is the energy range that would correspond to the relative variance if the spectrum of captured neutrons (averaged over many resonances) were independent of neutron energy, and  $\nu_e$  is the number of resonances that would correspond to the relative variance if the neutron-capture rates were the same for all resonances. For convenience, in the remainder of this paper we will use the notation  $\Delta I/I \equiv \langle (\Delta I)^2 \rangle^{1/2} / \bar{I}$  when referring to the relative rms uncertainty in the intensity.

The results of calculations of  $w_e$  are given in Fig. 10 as a function of the range of integration  $E_2$  and the width  $w_n$  of the spectrum of captured neutrons. Notice that the curves of  $w_e/w_n$  versus  $E_2/w_n$  do not depend sensitively on  $w_n$ . Thus, it appears that one can make a reliable estimate of  $\Delta I/I$  in spite of uncertainties in the width of the neutron-capture spectrum.

A possible complication in applying Eq. (14) to a determination of  $\Delta I/I$  for experimental  $\gamma$ -ray lines is that the value of  $E_2$  is not definite, because of

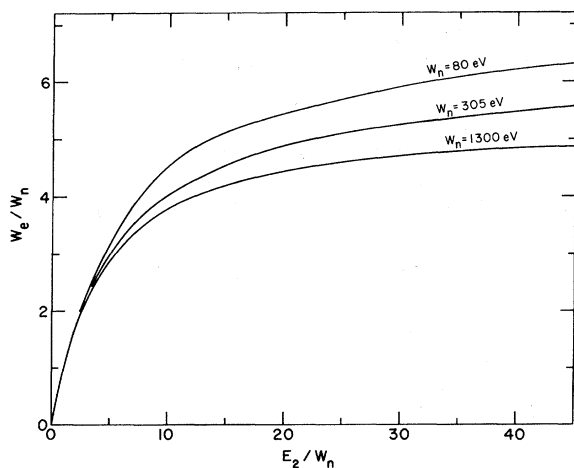


FIG. 10. Curves of  $w_e/w_n$  versus  $E_2/w_n$  for several neutron-capture spectra. The parameters used in the calculations are given in Tables I and II.

the influence of resolution broadening and because we determine  $\gamma$ -ray intensities by means of a visual fitting procedure (as described in Sec. II) that does not make use of a well-defined region of neutron energy. Fortunately, however, these uncertainties do not have much influence on the derived value of  $w_e$ . The width of the energy band that influences a determination of the intensity is roughly the observed width of the  $(\bar{n}, \gamma)$  line, which is usually about 8 keV. Thus, since  $8 \text{ keV} \gg w_n$  for almost all targets, the shape of the curves in Fig. 10 assures that  $w_e$  does not depend sensitively on what value of  $E_2$  is used.

The various quantities discussed above are summarized in Table III for the targets used in the measurements described in this paper. Here the resolution width  $w_\gamma$  was determined from the width of the  $^{10}\text{B}(n, \gamma)$  line at 7006 keV. Values of  $w_n$  are the full widths at half maximum (FWHM) of the neutron-capture spectra calculated from Eq. (10) for the neutron-resonance parameters given in Table I. The corresponding values of  $w_e$  were inferred from Fig. 10 for  $E_2 = w_\gamma$ , and values of  $(\Delta I/I)_{\text{PT}}$  and  $\nu_e$  were calculated from Eq. (15). The values of  $\bar{\mu}$  required in Eq. (15) were obtained by numerical calculations that are accurate to only 20 or 30%. However, because of the form of Eq. (15), the rather large uncertainties in  $\bar{\mu}$  usually cause an uncertainty of less than 5% in  $(\Delta I/I)_{\text{PT}}$ . The over-all uncertainty in  $(\Delta I/I)_{\text{PT}}$  is thought to be about 15% when the neutron-resonance parameters are known reasonably well.

In the last four columns of Table III the theoretical values of  $(\Delta I/I)_{\text{PT}}$  are compared with the rms scatter observed in several sets of measured intensities that are treated in several alternate ways. Although a quantitative treatment of this subject is deferred to Sec. V E, it should be noted at this time that the experimental values are in generally good agreement with the theoretical values. This agreement establishes the qualitative validity of our analysis of the neutron-capture process.

Since  $w_e$  is largely determined by  $w_n$ , it is obviously desirable to have a qualitative understanding of the factors that control the width  $w_n$ . The most important factor is the absorber thickness  $t$ , since the width of the spectrum of neutrons incident on the sample is proportional to  $t^2$ . As may be inferred from Eq. (9), the width  $w_n$  is a less sensitive monotonically increasing function of the quantities  $\Gamma_\gamma/S_0D$  and  $\bar{n}gS_0DA^{1/2}$ , where  $S_0$  is the  $s$ -wave strength function,  $g$  the statistical weight factor associated with the neutron resonances, and  $A$  is the atomic weight. Thus, to minimize the random fluctuations in an average-resonance-capture measurement, one should use a large sample and a thick absorber.

TABLE III. Summary of characteristics of neutron-capture spectra. Here  $w_\gamma$  is the experimental resolution width and  $w_n$  is the width of the neutron-capture spectrum, both FWHM;  $w_e$  is the effective width of the capture spectrum and  $\nu_e$  is the effective number of resonances in the spectrum, as defined by Eq. (15). The relative rms uncertainty in intensity expected from Porter-Thomas fluctuations is  $(\Delta I/I)_{PT}$ , whereas  $(\Delta I/I)_{obs}$ ,  $(\Delta I/I)_1$ , and  $(\Delta I/I)_2$  are related experimental quantities deduced from the data in the ways discussed in Sec. V E.

Emitting nucleus	Sample No.	$w_\gamma$ (keV)	$w_n$ (eV)	$w_e$ (keV)	$\nu_e$	$(\frac{\Delta I}{I})_{PT}$	$(\frac{\Delta I}{I})_{obs}$	$(\frac{\Delta I}{I})_1$	$(\frac{\Delta I}{I})_2$
$^{103}\text{Pd}$	10	7.9	330	1.67	22	0.30			
$^{105}\text{Pd}$	10	7.9	610	2.56	20	0.32			
$^{106}\text{Pd}$	9	7.7	142	0.88	34	0.24			
$^{106}\text{Pd}$	10	7.9	500	2.25	76	0.163	0.13	$0.15 \pm 0.05$	$0.152 \pm 0.05$
$^{155}\text{Gd}$	8	6.3	280	1.42	13	0.40			
$^{156}\text{Gd}$	8	6.3	305	1.51	240	0.083	0.15	$0.13 \pm 0.04$	$0.086 \pm 0.023$
$^{157}\text{Gd}$	8	6.3	490	2.08	32	0.25			
$^{158}\text{Gd}$	8	6.3	365	1.70	113	0.133			
$^{165}\text{Er}$	7	5.8	270	1.36	61	0.182			
$^{165}\text{Er}$	6	6.5	180	1.03	41	0.22			
$^{167}\text{Er}$	6	6.5	440	1.96	39	0.23			
$^{168}\text{Er}$	4	5.5	3	0.03	3	0.78			
$^{168}\text{Er}$	5	7.7	80	0.56	59	0.185	0.27	$0.26 \pm 0.07$	$0.18 \pm 0.06$
$^{168}\text{Er}$	6	6.5	290	1.45	143	0.118	0.21	$0.18 \pm 0.05$	$0.15 \pm 0.05$
$^{169}\text{Er}$	6	6.5	420	1.87	38	0.23			
$^{166}\text{Ho}$	1	5.4	7	0.05	8	0.51			
$^{166}\text{Ho}$	2	5.4	86	0.56	45	0.21	0.19	$0.22 \pm 0.04$	$0.23 \pm 0.04$
$^{166}\text{Ho}$	3	7.9	523	2.30	167	0.110	0.22	$0.19 \pm 0.04$	$0.14 \pm 0.03$

#### D. Shapes of $\gamma$ -Ray Lines

Section III A lays the groundwork for a discussion of the experimentally observed shapes of the  $\gamma$ -ray lines in average-resonance-capture spectra. Consider first the lines formed by  $s$ -wave capture followed by  $E1$  radiation. Here the main part of the line is obscured by resolution broadening, but the high-energy tail is effectively resolved. In this tail, most samples satisfy the conditions  $\Gamma_\gamma \ll \Gamma_n$ ,  $\bar{n}\sigma_m \ll 1$ , and  $\bar{T} \approx 1$ , so that we expect  $\gamma_{ij} \propto E_n^{-2}$ , according to Eq. (6). Our data are consistent with this expectation.

The line shape associated with  $p$ -wave capture is more interesting. The  $p$ -wave resonances satisfy the condition  $\bar{n}\sigma_m < 1$  for the whole range of neutron energy, so that the capture probability  $\bar{C}(E_n)$  should be proportional to  $\sigma_0$ . The neutron width for the  $p$ -wave resonances is given by  $\Gamma_n = S_1 D x^2 / (1 + x^2)$ , where  $x \equiv kR$  is the product of the wave number  $k$  and the nuclear radius  $R$ . For the neutron-energy range involved in our measurements, this width is well approximated by  $\Gamma_n \approx 2.3 \times 10^5 S_1 D_i q_j E_n^{3/2}$ , where  $S_1$  is the  $p$ -wave neutron strength function and  $q_j = 1$  or  $2$ , depending on whether one or two channel spins contribute to the formation of the initial state.

For the typical nucleus, the  $p$ -wave neutron widths are so small that  $\Gamma_n \ll \Gamma_\gamma$  up to quite a high energy. Thus the neutron capture rate (and hence the  $\gamma$ -ray intensity) varies as  $\bar{T}/E_n^{1/2}$ . This slow dependence on  $E_n$  is quite unlike the  $E_n^{-2}$  depen-

dence of  $s$ -wave capture, and the long tail that is characteristic of  $p$ -wave capture should be clearly recognizable if the line is strong enough that its tail is detectable.

The difference between the energy dependences of  $s$ -wave and  $p$ -wave capture leads one to expect that the  $\gamma$ -ray line shape should depend on the parity of the final state. If the parities of the target and final states are opposite, the dominant process is  $s$ -wave capture followed by  $E1$  radiation, so that

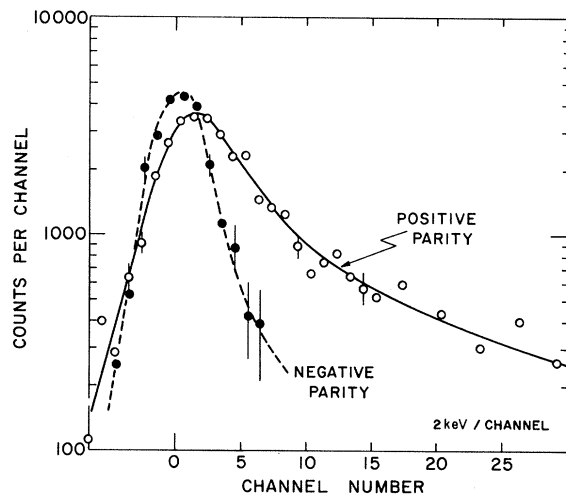


FIG. 11. Dependence of the shapes of  $\gamma$ -ray lines from  $^{105}\text{Pd}(\bar{n}, \gamma)^{106}\text{Pd}$  on the parity of the final state. The data were obtained with sample No. 10 of Table II.

the  $\gamma$ -ray line is relatively narrow and symmetrical; whereas, if the parities of the states are the same, there may be significant contributions from  $s$ -wave capture followed by  $M1$  radiation and also from  $p$ -wave capture followed by  $E1$  radiation, so that the  $\gamma$ -ray line may be relatively broad and have a long high-energy tail. Figure 11 shows that the difference between the line shapes for positive- and negative-parity states is very large for some nuclides. An important result of this investigation is the demonstration that this difference is a valuable source of information about parities for low-energy states in many nuclides.

#### IV. SPECTROSCOPIC RESULTS

##### A. $^{165}\text{Ho}(n, \gamma)^{166}\text{Ho}$

##### 1. Average-Resonance-Capture Data

The average-resonance-capture ( $\bar{n}, \gamma$ ) spectrum for the reaction  $^{165}\text{Ho}(n, \gamma)^{166}\text{Ho}$  provides a good illustration of the use of the *intensity* of  $\gamma$ -ray lines to obtain spectroscopic information. Measurements were made on three samples—one with a thick  $^{10}\text{B}$  absorber, one with a thin absorber, and one with a very thin absorber. Quantitative information about the samples is given in Table II.

Parts of the  $\gamma$ -ray spectra obtained are given in Figs. 12 and 13. Notice in Fig. 12 that the  $\gamma$ -ray line width increases and the signal-to-background ratio decreases with increasing absorber thickness.

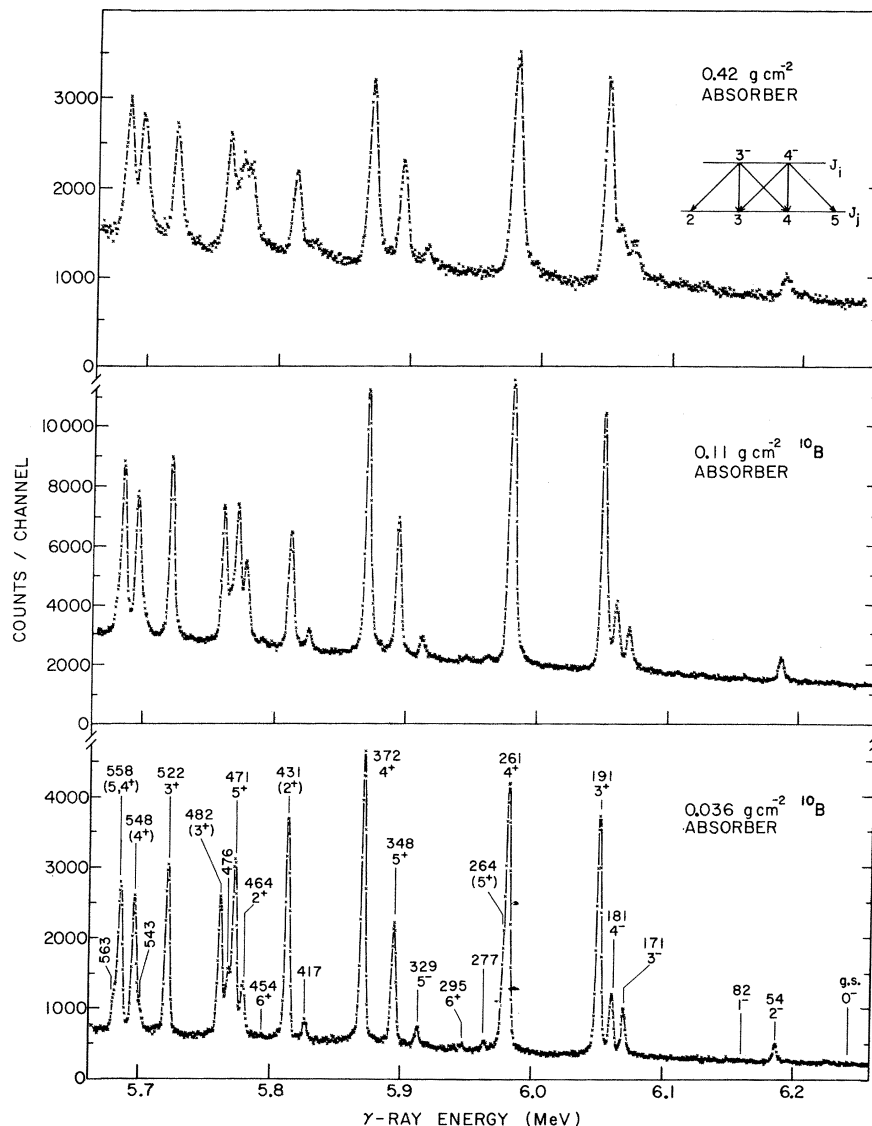


FIG. 12. Spectra for  $^{165}\text{Ho}(\bar{n}, \gamma)^{166}\text{Ho}$ . The  $J^\pi$  values given on the lowest curve are those reported by Motz *et al.* (Ref. 17).

The diagram in the upper right of Fig. 12 shows how the spectrum is formed. Since  $^{165}\text{Ho}$  is a nucleus for which the  $s$ -wave strength function is relatively large and the  $p$ -wave strength function is expected to be small, only  $s$ -wave capture is expected to produce a significant intensity. Thus, since the target nucleus has spin and parity  $J^\pi = \frac{7}{2}^-$ , the initial states formed by neutron capture have  $J_i^\pi = 3^-$  or  $4^-$ . Dipole transitions from these initial states can feed final states with  $J_f = 2, 3, 4$ , or  $5$ . Tentatively, we will assume that quadrupole transitions are too weak to be important.

As was shown in Sec. III, the intensity of a transition path is expected to be independent of the spin of the final state and only slightly dependent on the spin  $J_i$  of the initial state, except for  $J_i = 0$ . Thus, the six transition paths shown in Fig. 12 should have approximately equal intensities and the  $\gamma$ -ray lines associated with final states with  $J_f = 3$  and  $4$  should be twice as strong as those for states with  $J_f = 2$  and  $5$ . Also,  $E1$  transitions to positive-parity states are expected to be 5–10 times as strong as  $M1$  transitions to negative-parity states. Consequently, from the observed intensities of the lines one would expect to be able to assign the parities of the low-energy states in  $^{166}\text{Ho}$  with ease and to be able to set narrow limits on the spins of the states. A qualitative examination of the spectra in Fig. 12 shows that these expectations are consistent with the observed intensities for the states of known spin and parity.

A tacit assumption involved in most neutron-capture  $\gamma$ -ray studies of heavy nuclides is that the high-energy lines are formed by *primary* transitions

from the initial state formed by neutron capture. This assumption can be tested in the  $(\bar{n}, \gamma)$  spectra by observing the  $\gamma$ -ray line shapes, since only the lines associated with primary transitions can have the characteristic line broadening caused by capture of epithermal neutrons. All of the well-resolved lines observed to date in our  $(\bar{n}, \gamma)$  spectra for many nuclei ( $\sim 1000$  lines) exhibit the expected broadening and thus all are formed by primary transitions.

The intensities and energies of the  $\gamma$ -ray lines in the average-resonance-capture spectra were calculated by means of the procedures outlined in Sec. II. The results for  $^{165}\text{Ho}(\bar{n}, \gamma)^{166}\text{Ho}$  are given in Table IV, where they are compared with the results Motz *et al.*<sup>17</sup> obtained from an extensive series of  $(n, \gamma)$  and  $(d, p)$  measurements.

Normally, the most accurate values of energies would be obtained from the  $(\bar{n}, \gamma)$  measurement with the thinnest absorber because it has a better signal-to-background ratio and a narrower linewidth than a measurement with a thick absorber. However, for holmium the energy scale of the run with the thinnest absorber was not calibrated accurately; thus, the energies were determined from the spectrum for the absorber of intermediate thickness ( $0.11 \text{ g/cm}^2$ ). Note that an  $(\bar{n}, \gamma)$  measurement with a thin absorber is preferable to a thermal-capture measurement for most purposes, because the  $(\bar{n}, \gamma)$  spectrum is usually less sensitive to impurities in the sample and the diminished Porter-Thomas fluctuations make it possible to observe lines that may be absent in the thermal-capture spectrum.

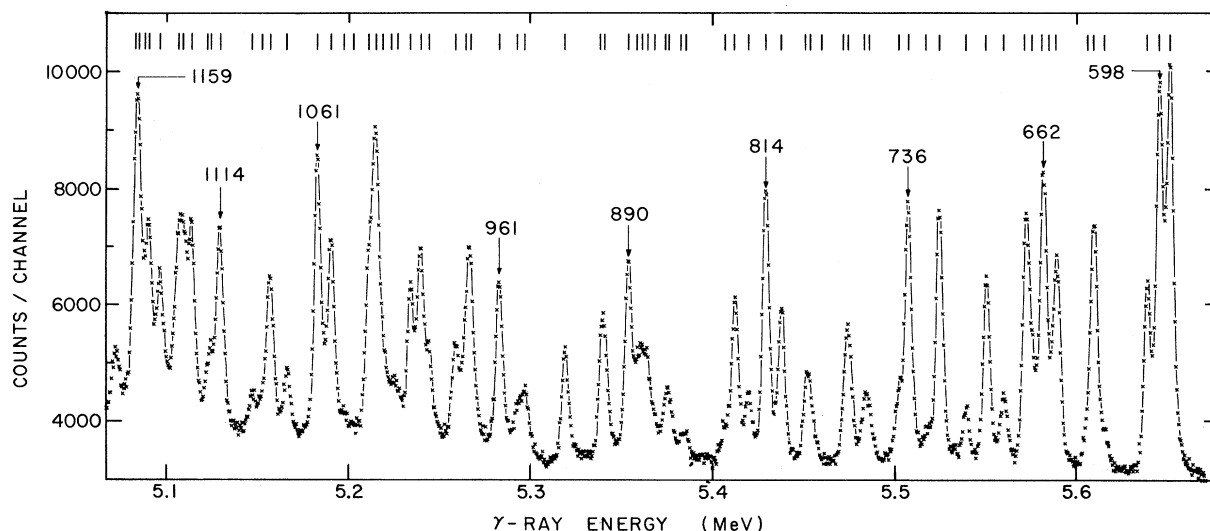


FIG. 13. Spectrum of  $^{165}\text{Ho}(\bar{n}, \gamma)^{166}\text{Ho}$  for a  $^{10}\text{B}$  absorber  $0.11 \text{ g/cm}^2$  thick. The numbers associated with some of the lines are excitation energies. The short vertical lines at the top of the figure show the positions of all the lines revealed by a quantitative analysis.

The apparent energies of the lines in an  $(\bar{n}, \gamma)$  spectrum are significantly greater than they would be for thermal-neutron capture because of the non-zero energies of the captured neutrons. The magnitude of this energy shift may be determined by a calculation of the kind illustrated by Fig. 8. The calculated energy shift is +0.65 keV for the holmium spectrum of interest. The  $\gamma$ -ray energies listed in Table IV have been corrected for this shift—that is, they (and all other values of  $E_\gamma$  in this paper) are intended to be the energies that would be measured for thermal-neutron capture.

Since the ground-state transition in  $^{166}\text{Ho}$  was not observed, the energy scale of the final states was established by assuming that the energy of the first excited state is 54.24 keV. Note that the excited-state energies obtained from the average-resonance-capture data are in excellent agreement with the accurate values obtained from the low-energy  $\gamma$  rays<sup>17</sup> up to about 500 keV. However, our val-

ues appear to be systematically too low at energies greater than 500 keV.

Whereas a measurement with a thin absorber is desirable for high detection sensitivity and for an accurate determination of energies, a thick absorber is needed to obtain a spectrum in which the Porter-Thomas fluctuations of the intensities are small. At the same time, the absorber must not be so thick that the signal-to-background is very poor. In a typical measurement with our experimental system, these competing requirements dictate that the absorber thickness should be about 0.4 g/cm<sup>2</sup> of  $^{10}\text{B}$ .

The behavior of the intensities of the lines observed in the run with the thickest absorber (0.47 g/cm<sup>2</sup>) are examined in Figs. 14 and 15. Let us first consider the energy dependence of the intensity. The initial step is to plot  $I_\gamma/E_\gamma^3$  versus  $E_\gamma$ , as in Fig. 14. Here one sees that the points associated with known positive-parity states are widely

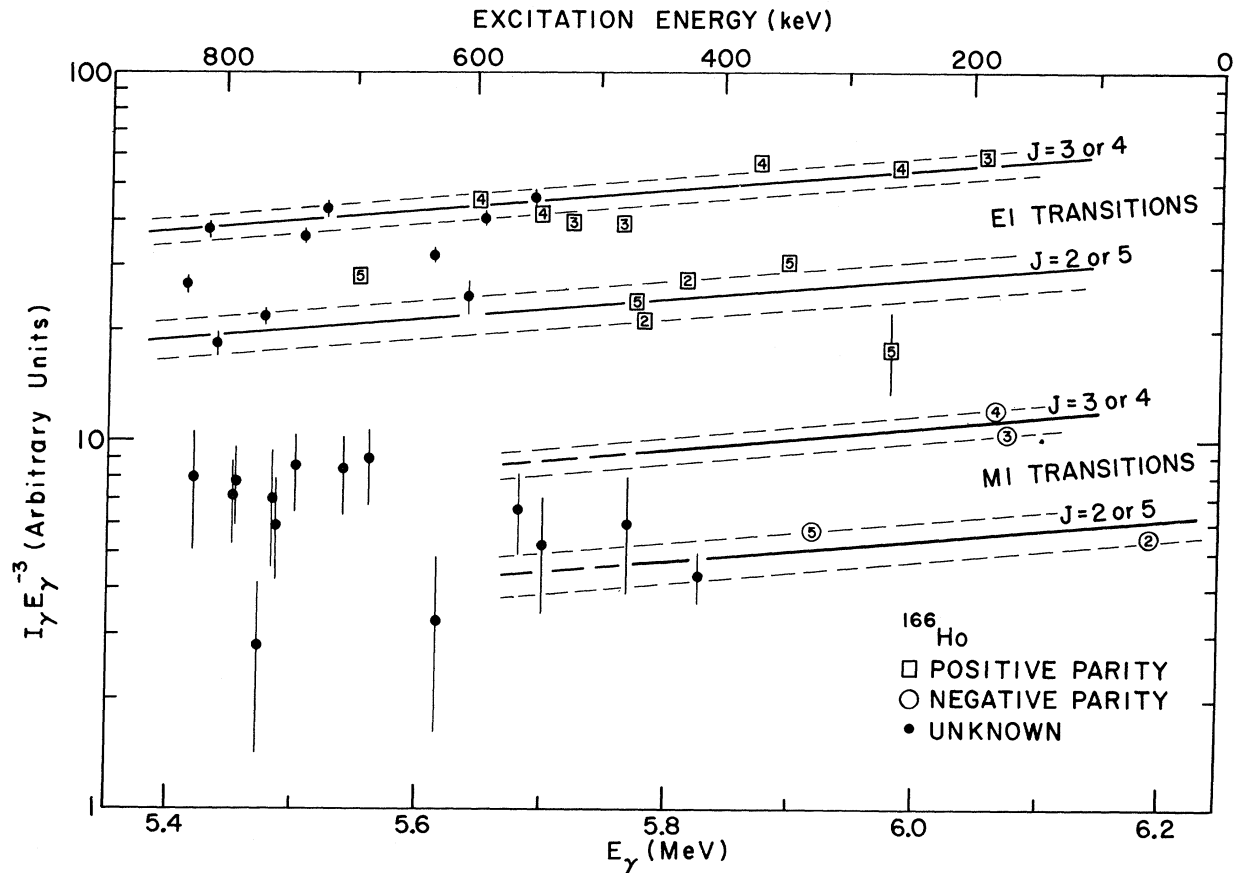


FIG. 14. Plot of  $I_\gamma E_\gamma^{-3}$  versus  $E_\gamma$  for  $^{166}\text{Ho}(\bar{n}, \gamma)^{166}\text{Ho}$ . The numbers within some of the points are the  $J$  values reported by Motz *et al.* (Ref. 17), and the indicated parities are also from Ref. 17. The error bars associated with the points are rms errors of measurement; where no error bar is given, the error is smaller than the size of the data point. The four solid lines through the data were inferred from Fig. 15, and the dashed lines associated with each solid line indicate the expected rms scatter caused by Porter-Thomas fluctuations.

separated from those for negative-parity states. Also, most of the intensities for states known to have  $J=3$  or 4 are roughly twice as great as those with  $J=2$  or 5. Thus, the data points appear to fall along four lines in the expected way. In order to obtain the most meaningful specification of the shapes and positions of these lines, we combine the data for the two sets of  $J$  values by plotting  $I_\gamma E_\gamma^{-3} Q_J^{-1}$  versus  $E_\gamma$ , where  $Q_J=1$  or 2 is the number of transition paths available. When the  $J$  value is known, there is no doubt about the choice of  $Q_J$ , of course. However, when  $J$  is not known,  $Q_J$  must be inferred from the measured average intensity; the justification for this somewhat subjective choice depends on the over-all internal consistency of the data, as discussed later in this section.

The plot of  $I_\gamma E_\gamma^{-3} Q_J^{-1}$  versus  $E_\gamma$  for the thick-absorber holmium data (Fig. 15) includes the data for all of the positive-parity states with  $E_x < 825$  keV except those in the range 650–675 keV, where the spectrum is judged to be too complex; similarly, the data for all negative-parity states with  $E_x < 450$  keV are used. The error associated with each point is an rms statistical error caused by the combined effects of Porter-Thomas fluctuations and errors in measurement. The magnitude of the Porter-Thomas fluctuation (namely  $\pm 11\%$  for an intensity resulting from only one transition path) was calculated in the way outlined in Sec. III C; and various assumptions and results of the calculation are given in Tables I, II, and III.

The points for the negative-parity states are at least consistent with the smooth energy dependence

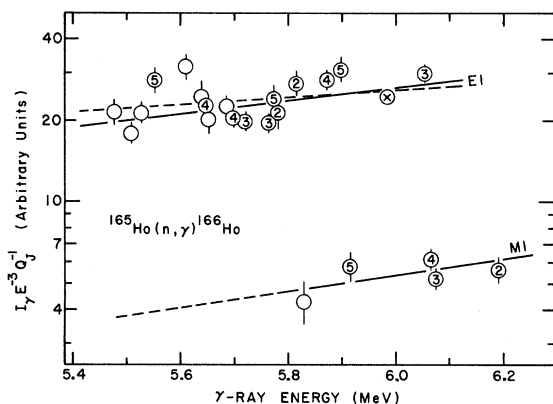


FIG. 15. Plot of  $I_\gamma E_\gamma^{-3} Q_J^{-1}$  versus  $E_\gamma$  for  $^{165}\text{Ho}(n, \gamma)^{166}\text{Ho}$ . The numbers within some of the points are the  $J$  values reported in Ref. 17. The point with an  $x$  within it is the combined result for the closely-spaced pair of states with  $J^\pi = 4^+$  and  $5^+$ . The indicated errors include the contributions from both Porter-Thomas fluctuations and errors of measurement. The dashed line was calculated from Eq. (16) with the parameters given in Ref. 20.

given by the straight line in Fig. 15, but the data are not extensive enough to provide a good test of this hypothesis.

For the  $E1$  transitions (unlike the  $M1$  transitions), we have some theoretical guidance of what energy dependence to expect. In particular, there is a mounting body of evidence<sup>7, 18, 19</sup> that the behavior of the high-energy  $E1$  transitions following neutron capture may be inferred at least approximately on the assumption that they are directly related to the well-known giant resonance in the photonuclear reaction. In this approach,<sup>18</sup> the  $\gamma$ -ray strength function  $\langle \Gamma_{ij}/D_i \rangle$  of all  $E1$  transitions is assumed to be describable in terms of the total cross section  $\sigma_t(\gamma)$  of the ground-state transition, and the giant-resonance shape of  $\sigma_t(\gamma)$  is assumed to extend down to the energy range of interest for the neutron-capture  $\gamma$  rays. Then the energy dependence of the  $\gamma$ -ray strength function may be calculated from the relationship

$$\left\langle \frac{\Gamma_{ij}}{D_i} \right\rangle \propto E_\gamma^2 \sigma_t(\gamma) = E_\gamma^4 \left[ \frac{\sigma_a^0 \Gamma_a^2}{(E_a^2 - E_\gamma^2)^2 + E_\gamma^2 \Gamma_a^2} + \frac{\sigma_b^0 \Gamma_b^2}{(E_b^2 - E_\gamma^2)^2 + E_\gamma^2 \Gamma_b^2} \right], \quad (16)$$

where the cross section  $\sigma_t(\gamma)$  is described by two Lorentzian terms (to take account of quadrupole splitting), and  $E_a$ ,  $E_b$ ,  $\Gamma_a$ ,  $\Gamma_b$ ,  $\sigma_a^0$ , and  $\sigma_b^0$  are resonance energies, widths, and peak cross sections that have been determined in photonuclear investigations.<sup>20</sup> Axel<sup>18</sup> has shown that this expression for  $\langle \Gamma_{ij}/D_i \rangle$  is approximately proportional to  $E_\gamma^5$  for the energy range corresponding to the high-energy neutron-capture  $\gamma$  rays of most nuclides.

The  $E1$  energy dependence calculated from Eq. (16) is given by the dashed curve in Fig. 15; note that it is effectively a straight line on a semilogarithmic plot. The  $E1$  data seem to be consistent with this curve, except for two or three widely scattered points. Whether or not this scatter is consistent with the calculated random errors (mainly Porter-Thomas fluctuations) may be judged from a  $\chi^2$  test of the best fit to the data. Consider first the quality of the fit for the dashed-line curve; if all 19 of the  $E1$  points are used, then the value of  $\chi^2$  is 52.6. This is to be compared with  $(19 - 2) = 17$  degrees of freedom. Such a large value of  $\chi^2$  indicates that something is almost surely wrong, since, for a least-squares fit under the specified assumptions, the probability for  $\chi^2$  to be as large as 52 is vanishingly small. Moreover, the value of  $\chi^2$  is not significantly smaller for any other simple curve; it is 52.8 for the solid line in the figure.

Three possible explanations of the large value of  $\chi^2$  need to be considered: (1) the Porter-Thomas

fluctuations are larger than was assumed, (2) non-random fluctuations caused by nuclear-structure effects are being detected, or (3) some of the intensities used in the analysis result from the summing of two or more unresolved lines. Of these, the first explanation seems most unlikely since (a) the Porter-Thomas uncertainties calculated in the same way are consistent with the observed scatter in the data for some other nuclides, (b) the calculation of the capture spectrum is believed to be reliable, and (c) the value of  $\chi^2$  for the holmium data obtained with the 0.11-g/cm<sup>2</sup> absorber (for which Porter-Thomas fluctuations are relatively large) is consistent with our assumptions, since for it  $\chi^2 = 14.6$  for 18 degrees of freedom.

The possibility of nonrandom nuclear-structure effects cannot be excluded for any particular nucleus such as <sup>166</sup>Ho, but it seems unlikely that such effects are important because (a) the intensities of the better-resolved transitions to low-energy states of <sup>166</sup>Ho are consistent with the statistical model, (b) *none* of the intensities of transitions observed in the nuclides considered in this paper definitely *require* a nuclear-structure interpretation, and (c) the probability of a superposition of unresolved *E1* and *M1* transitions is not small in regions of high level density. In the latter connection, let us assume that the density of negative-parity states is the same as the density of positive-parity states (about 57 states per MeV for  $E_x > 450$  keV) and also that an *E1*-*M1* pair is indistinguishable from a single line if they fall within  $\pm 2.5$  keV of each other. Then, one readily calculates that (on the average) summing is expected to increase the intensity of four points in Fig. 15—of one point by about 10%, of two points by 20%, and of one point by 40%. These estimates are not inconsistent with what is observed in the figure, where two points appear to be too high by roughly 40%. The summing of two *E1* transitions is less probable, since to be undetected the two lines would need to be closer together, and there is no evidence in the <sup>166</sup>Ho data for such summing. However, a pair of unresolved states with  $J=2$  or 5 could not be distinguished from a single state with  $J=3$  or 4.

Since the anomalous points in Fig. 15 can easily be explained in terms of the summing of unresolved lines, we will proceed by tentatively assuming that such summing is the cause for the unacceptably large value of  $\chi^2$  for the *E1* data. In any case, none of the parity assignments and few if any of the spin assignments given in columns 10 and 11 of Table IV would be changed if a nuclear-structure effect large enough ( $\pm 10\%$ ) to explain the observed fluctuations were assumed to be present. The question of the magnitude of fluctuations from nuclear-structure effects will be considered again in Sec. V after

all the data have been presented.

The tentative assumption that the widely scattered points in Fig. 15 result from the summing of unresolved lines leads to the conclusion that the high points at 5549 and 5608 keV should be ignored in fitting the data and this, in turn, leads to the conclusion that the solid line in Fig. 15 is a somewhat better fit than the dashed line. The failure of the giant-resonance formula to give the best fit is not unexpected in view of the assumptions involved in the model.

A final question about Fig. 15 is whether our conclusion about the energy dependence of  $I_\gamma E_\gamma^{-3}$  could be negated by wrong choices of  $Q_J$  for points with unknown  $J$ . It is almost certain that there was no error of this kind except possibly for the 5608-keV line, since a wrong choice for any other point would add at least 50 to the value of  $\chi^2$ .

The shapes and positions of the solid curves in Fig. 15 may now be transferred to Fig. 14 as a good description of the expected values of the average intensities. For the *M1* transitions, the absence of strong theoretical guidance about the energy dependence of the strength function prevents any reliable extrapolation to lower  $\gamma$ -ray energies.

Although a  $\chi^2$  test such as is outlined above is perhaps the most complete and objective way to test the reliability of the average-spectrum method, an intuitively more appealing demonstration of its validity is given by a histogram of the relative intensities of transitions to states with known spin and parity. Histograms of this kind are given in Fig. 16, where the intensities of states with  $J_j = J_0$

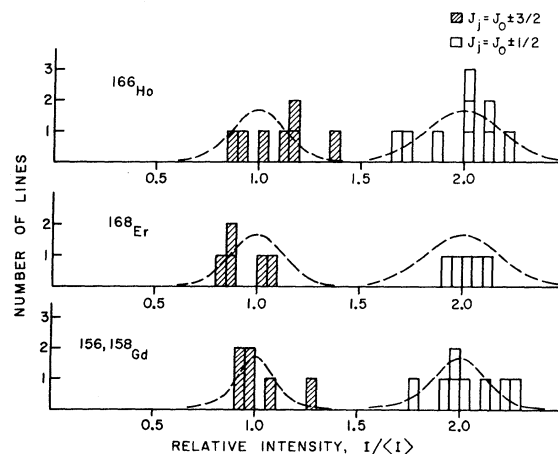


FIG. 16. Histograms of relative intensities of average-resonance-capture transitions, where the expected value ( $I$ ) is the value given by the smooth curve corresponding to the states with  $J_j = J_0 \pm \frac{3}{2}$ . Only the data for transitions to final states with previously well-established  $J^\pi$  values (Refs. 17, 31, 35, and 38) are used; also data with large experimental errors ( $\Delta I/I > 0.10$ ) are excluded.

TABLE IV. High-energy transitions in  $^{165}\text{Ho}(\bar{n},\gamma)^{166}\text{Ho}$  and states of  $^{166}\text{Ho}$ . The random errors for the gamma energies  $E_\gamma$  are the same as for the excitation energies  $E_x$ , and the absolute values of  $E_\gamma$  are uncertain by an additional 0.6 keV. The last significant figures of some values of  $E_x$  inferred from low-energy  $\gamma$  rays have been dropped. In column 3, excitation energies reported here for the first time are marked with an asterisk. Typically, the values of  $E_x$  obtained from the  $(d,p)$  data are uncertain by  $\pm 2$  keV. Parentheses around an excitation energy mean that the existence of the state is uncertain. The symbol  $n$  in columns 10 and 11 means  $J=2,3,4$ , or 5.

Present work $E_\gamma$ (keV)	$E_x$ (keV)	Excitation energies (keV) from other measurements <sup>a</sup> ( $n,\gamma$ )			Relative intensity $I_\gamma E_\gamma^{-3}$ for absorber thickness ( $\text{g}/\text{cm}^2$ $^{10}\text{B}$ )			Spin and parity assignments			Band label
		Low energy	High energy	( $d,p$ )	0.036	0.107	0.418	Others (Ref. a)	Ours	Adopted	
6242.5	0	0			<2	<7		0 <sup>-</sup>		0 <sup>-</sup>	A
								7 <sup>-</sup>		7 <sup>-</sup>	B
6188.3	54.2 $\pm$ 0.2	54.24		53	31 $\pm$ 1	73 $\pm$ 3	56 $\pm$ 3	2 <sup>-</sup>	2,5 <sup>-</sup>	2 <sup>-</sup>	A
6160.5	82.0 $\pm$ 1.0	82.47		82	<4	6 $\pm$ 3		1 <sup>-</sup>	(1,6 <sup>-</sup> )	1 <sup>-</sup>	C
				136	<4	<9		(8 <sup>-</sup> )		(8 <sup>-</sup> )	B
6071.6	170.9 $\pm$ 0.2	171.07	171	168	89 $\pm$ 4	89 $\pm$ 4	105 $\pm$ 5	3 <sup>-</sup>	3,4 <sup>-</sup>	3 <sup>-</sup>	C
6061.8	180.7 $\pm$ 0.2	180.47		181	106 $\pm$ 5	136 $\pm$ 6	123 $\pm$ 6	4 <sup>-</sup>	3,4 <sup>-</sup>	4 <sup>-</sup>	A
6051.8	190.7 $\pm$ 0.2	190.90	191		467 $\pm$ 14	585 $\pm$ 17	599 $\pm$ 12	3 <sup>+</sup>	3,4 <sup>+</sup>	3 <sup>+</sup>	D
			198		<4	<9					
5981.9	260.6 $\pm$ 0.2	260.66			526 $\pm$ 37	570 $\pm$ 40	561 $\pm$ 40	4 <sup>+</sup>	3,4 <sup>+</sup>	4 <sup>+</sup>	D
5978.9	263.6 $\pm$ 0.2	263.79	263		136 $\pm$ 34	243 $\pm$ 45	179 $\pm$ 45	(5 <sup>+</sup> )	2,5 <sup>+</sup>	5 <sup>+</sup>	Q
5964.3	(278.2 $\pm$ 1.0)				18 $\pm$ 3	10 $\pm$ 3	<20		(1,6 <sup>-</sup> )		
5946.8	(295.7 $\pm$ 1.5)			294	10 $\pm$ 5	11 $\pm$ 4	<20	(6 <sup>+</sup> )	1,6 <sup>-</sup>	(6 <sup>+</sup> )	E
				308	<4	<7		(9 <sup>-</sup> )		(9 <sup>-</sup> )	B
5912.4	330.1 $\pm$ 1.0	329.77	331	330	37 $\pm$ 4	47 $\pm$ 5	58 $\pm$ 4	5 <sup>-</sup>	2,5 <sup>-</sup>	5 <sup>-</sup>	C
			339		<5	<9					
5894.3	348.2 $\pm$ 0.2	348.26		348	254 $\pm$ 8	332 $\pm$ 9	310 $\pm$ 9	5 <sup>+</sup>	2,5 <sup>+</sup>	5 <sup>+</sup>	D
5870.6	371.9 $\pm$ 0.2	371.98	372	373	617 $\pm$ 12	648 $\pm$ 12	573 $\pm$ 12	4 <sup>+</sup>	3,4 <sup>+</sup>	4 <sup>+</sup>	F
		373.08						0,1 <sup>-</sup>		0,1 <sup>-</sup>	
		377.81			<6	<10		6 <sup>-</sup>		6 <sup>-</sup>	A
				(386)	<4	<7					
				(401)	<4	<7					
5826.2	416.3 $\pm$ 0.4	416.08*		421	41 $\pm$ 4	46 $\pm$ 5	43 $\pm$ 6		2,5 <sup>-</sup>	2 <sup>-</sup>	G
		425.99			<6	<10		(7 <sup>+</sup> )		(7 <sup>+</sup> )	E
5812.4	430.1 $\pm$ 0.2	430.04	430		477 $\pm$ 10	293 $\pm$ 5	275 $\pm$ 5	1 <sup>+</sup>		1 <sup>+</sup>	H
5790.5	(452.0 $\pm$ 1.0)				<6	<10		(2 <sup>+</sup> )	2,5 <sup>+</sup>	2 <sup>+</sup>	I
		453.77		457					(1,6 <sup>-</sup> )		
		464.48						6 <sup>+</sup>		6 <sup>+</sup>	D
5778.5	464.0 $\pm$ 0.5	464.48			105 $\pm$ 11	187 $\pm$ 13	215 $\pm$ 15	2 <sup>+</sup>	2,5 <sup>+</sup>	2 <sup>+</sup>	H
5771.8	470.7 $\pm$ 0.2	470.84	472	469	380 $\pm$ 19	326 $\pm$ 23	242 $\pm$ 17	5 <sup>+</sup>	2,5 <sup>+</sup>	5 <sup>+</sup>	F
5767.0	475.5 $\pm$ 1.0			476	112 $\pm$ 17	82 $\pm$ 16	59 $\pm$ 20		$n^-$	$n^-$	
5760.9	481.6 $\pm$ 0.2	481.84	482		312 $\pm$ 9	352 $\pm$ 7	393 $\pm$ 8	(3 <sup>+</sup> )	3,4 <sup>+</sup>	3 <sup>+</sup>	I
				514	<4	<8					
5720.6	521.9 $\pm$ 0.2	522.00	522	524	383 $\pm$ 11	480 $\pm$ 15	399 $\pm$ 12	3 <sup>+</sup>	3,4 <sup>+</sup>	3 <sup>+</sup>	H
5699.6	542.9 $\pm$ 1.0				43 $\pm$ 9	36 $\pm$ 12	52 $\pm$ 17		$n^-$	(4) <sup>-</sup>	(G)
5694.9	547.6 $\pm$ 0.2	547.96	545	546	307 $\pm$ 9	374 $\pm$ 12	413 $\pm$ 12	(4 <sup>+</sup> )	3,4 <sup>+</sup>	4 <sup>+</sup>	I
		(557.69)						7 <sup>-</sup>		7 <sup>-</sup>	C
5684.2	558.3 $\pm$ 0.2	558.56		557	350 $\pm$ 12	450 $\pm$ 13	456 $\pm$ 14	(5,4 <sup>+</sup> )	3,4 <sup>+</sup>	4 <sup>+</sup>	J
5680.0	562.5 $\pm$ 0.7	562.91*			68 $\pm$ 13	69 $\pm$ 17	65 $\pm$ 16		$n^-$	3 <sup>-</sup>	K
		567.58*		(566)	<10	<17				1 <sup>+</sup>	M
		(577.21)		(578)				(7 <sup>+</sup> )		(7 <sup>+</sup> )	D
		(588.10)		589		<8		(6 <sup>+</sup> )		(6 <sup>+</sup> )	F
5650.5	592.0 $\pm$ 0.3	592.50*	595		414 $\pm$ 21	524 $\pm$ 25	405 $\pm$ 20		3,4 <sup>+</sup>	3 <sup>+</sup>	L
5644.6	597.9 $\pm$ 0.3	598.46		599	416 $\pm$ 21	493 $\pm$ 25	458 $\pm$ 22	4 <sup>+</sup>	3,4 <sup>+</sup>	4 <sup>+</sup>	H
5637.7	604.8 $\pm$ 0.3	605.03*	602		167 $\pm$ 12	247 $\pm$ 12	244 $\pm$ 25		2,5 <sup>+</sup>	2 <sup>+</sup>	M
				(610)		<8					
5614.5	628.0 $\pm$ 1.0				30 $\pm$ 8	17 $\pm$ 9	32 $\pm$ 16		$n^-$	(5) <sup>-</sup>	(G)
5608.3	634.2 $\pm$ 0.2	634.31*		632	271 $\pm$ 8	360 $\pm$ 18	318 $\pm$ 16		(2,5 <sup>+</sup> )	5 <sup>+</sup>	I
	(634.2 $\pm$ 2.5)								( $n^-$ )	(4) <sup>-</sup>	K
5604.4	638.1 $\pm$ 1.5	638.32*	637		32 $\pm$ 11	17 $\pm$ 10			$n^-$	2 <sup>-</sup>	N
5587.6	654.9 $\pm$ 0.5			653	232 $\pm$ 7	279 $\pm$ 15			$n^+$	(5) <sup>+</sup>	J

TABLE IV (Continued)

Present work		Excitation energies (keV) from other measurements <sup>a</sup>			Relative intensity $I_\gamma E_\gamma^{-3}$ for absorber thickness (g/cm <sup>2</sup> <sup>10</sup> B)			Spin and parity assignments			Band label
$E_\gamma$ (keV)	$E_x$ (keV)	Low energy	High energy	( $n, \gamma$ ) ( $d, p$ )	0.036	0.107	0.418	Others (Ref. a)	Ours	Adopted	
5584.4	658.1±1.5				45±13				$n^-$	$n^-$	
5580.2	662.3±0.5		660		310±10	399±20			$n^+$	3 <sup>+</sup>	M
5574.8	667.7±1.0		667	668	100±10	39±10			$n^-$	$n^-$	
5571.4	671.1±0.5				234±11	358±15			$n^+$	4 <sup>+</sup>	L
5559.1	683.4±0.3				78±8	94±6	89±22		$n^-$	$n^-$	
			687		<10	<20					
5549.5	693.0±0.2 (693.0±2.5)	693.65	694	691	225±7	267±8	282±14	5 <sup>+</sup>	(2, 5) <sup>+</sup> ( $n^-$ )	5 <sup>+</sup> (3 <sup>-</sup> )	H N
5538.2	704.3±0.3				60±6	76±5	83±21		-	$n^-$	
5523.5	719.0±0.2		719	721	392±12	367±11	426±22		3, 4 <sup>+</sup>	(4) <sup>+</sup>	O
5516.7	725.8±1.5				14±7	30±7			$n^-$	(5) <sup>-</sup>	K
5506.5	736.0±0.2				288±8	380±11	360±18		3, 4 <sup>+</sup>	4 <sup>+</sup>	M
5501.2	741.3±0.4		742	739	79±12	93±18	85±21		$n^-$	$n^-$	
5486.5	756.0±1.0				28±5	50±20	58±20		$n^-$	$n^-$	
5483.5	759.0±1.0				80±8	75±20	69±24		$n^-$	$n^-$	
5473.7	768.8±0.3		768	767	194±6	199±10	215±11		2, 5 <sup>+</sup>	5 <sup>+</sup>	L
5471.2	771.3±1.5				27±14	51±20	28±14		$n^-$	(4) <sup>-</sup>	N
5459.0	783.5±1.5		784		13±5				1 <sup>-</sup>	-	
5453.0	789.5±1.0				65±15	86±20	77±39		$n^-$	$n^-$	
5450.2	792.3±1.0				93±20	94±20	70±39		$n^-$	$n^-$	
5436.7	805.8±0.2				169±5	225±7	183±18		2, 5 <sup>+</sup>	(5) <sup>+</sup>	O
5428.2	814.3±0.2		816	814	490±15	416±12	373±18		3, 4 <sup>+</sup>	(3) <sup>+</sup>	P
5418.8	823.7±0.4				91±6	91±6	79±40		$n^-$	$n^-$	
5411.4	831.1±0.2		830		198±6	252±7	266±13		(2, 5) <sup>+</sup>	5 <sup>+</sup>	M
5406.0	836.5±1.5				28±7	47±12			$n^-$	$n^-$	
5384.4	858.1±1.5				33±8	27±6			$n^-$	$n^-$	
5381.8	860.7±1.5					18±5			$n^-$	$n^-$	
5375.4	867.1±1.5				60±20	65±17			$n^-$	$n^-$	
5373.8	869.4±1.5				30±15	63±17			$n^-$	$n^-$	
5367.7	874.8±1.5				34±8	50±20			$n^-$	$n^-$	
5363.9	878.6±1.0				157±23	106±26					
5360.9	881.6±1.5		882			115±46					
5358.3	884.2±1.5					112±39					
5352.7	889.8±0.3		891	891	211±10	322±16			$n^+$	(4) <sup>+</sup>	P
5340.3	902.2±1.0				18±7	119±36					
5338.5	904.0±0.5		905	907	248±12	165±50					
5318.1	924.4±0.2			925	120±6	192±10					
5296.3	946.2±0.7			(942)	96±6	109±11					
5291.9	950.6±0.7				57±6	77±8					
5281.9	960.6±0.3		962	961	216±11	302±15					
5266.4	976.1±0.5				232±11	284±20					
5263.5	979.0±1.0				58±14	170±25					
5257.9	984.6±0.5			982	108±7	182±13			$n^+$	(5) <sup>+</sup>	P
5243.7	998.8±0.5				55±5	132±13					
5239.0	1003.5±0.3				243±12	321±16					
5233.6	1008.9±0.3		1006	1007	165±8	272±13					
5226.4	1016.1±1.0				42±8	71±14					
5222.5	1020.0±1.5				32±11	63±22					
5218.0	1024.5±1.5				43±15	122±42					
5214.2	1028.3±0.4		1030		515±26	676±10					
5210.2	1032.3±0.7			1035	161±24	271±41					
5201.6	1040.9±1.5					20±5					
5196.8	1045.7±1.5					30±10					
5189.5	1053.0±0.2			1057	283±14	351±17					
5182.0	1060.5±0.2		1062		547±27	510±25					
5165.3	1077.2±0.2			1080	97±4	112±5					

TABLE IV (Continued)

Present work		Excitation energies (keV) from other measurements <sup>a</sup>			Relative intensity $I_\gamma E_\gamma^{-3}$ for absorber thickness (g/cm <sup>2</sup> <sup>10</sup> B)			Spin and parity assignments			
$E_\gamma$ (keV)	$E_x$ (keV)	Low energy	High energy	( $n, \gamma$ ) ( $d, p$ )	0.036	0.107	0.418	Others (Ref. a)	Ours	Adopted	Band label
5156.1	1086.4 ± 0.3				244 ± 12	281 ± 14					
5151.8	1090.7 ± 1.5		1089			48 ± 16					
5146.2	1096.3 ± 1.0		1099		83 ± 8	60 ± 3					
5128.6	1113.9 ± 0.2			1105	554 ± 27	372 ± 18					
5123.8	1118.7 ± 1.0		1118	1122		130 ± 32					
5121.6	1120.9 ± 1.5					49 ± 17					
5112.9	1129.6 ± 0.7				194 ± 13	338 ± 23					
5108.5	1134.0 ± 1.5				137 ± 27	237 ± 47					
5105.9	1136.6 ± 1.0		1137	1137	344 ± 24	255 ± 25					
5095.8	1146.7 ± 0.5				138 ± 11	235 ± 47					
5089.5	1153.0 ± 0.5			1154	294 ± 30	317 ± 32					
5087.1	1155.4 ± 1.5					118 ± 47					
5084.0	1158.5 ± 1.0					351 ± 10					
5081.9	1160.6 ± 1.0		1160			352 ± 10					

<sup>a</sup>Motz *et al.*, Ref. 17.

$\pm \frac{3}{2}$  are seen to be well separated from those with  $J_j = J_0 \pm \frac{1}{2}$ , as expected from our model.

The foundation for a state-by-state consideration of <sup>166</sup>Ho has now been prepared. First notice in Table IV that the  $E2$  transition to the  $1^-$  state at 82 keV (although apparently detected in one spectrum) is weak enough to justify the neglect of the influence of quadrupole transitions to negative-parity states with  $J=2, 3, 4$ , or  $5$ .

The weak line at 5947 keV could be interpreted as an  $M2$  transition, since it seems to be associated with a proposed  $6^+$  state at 294 keV. However, this possibility cannot be accepted without further evidence because  $M2$  transitions are so weak in heavy nuclei that few if any have been reported and because the  $6^+$  assignment is tentative. On the other hand, the line has roughly the right intensity for an  $E2$  transition, and hence this is the tentative interpretation of the  $(\bar{n}, \gamma)$  data.

The very weak lines at 5790 and 5965 keV are also tentatively interpreted as  $E2$  transitions to states at 278 and 452 keV. However, there is a possibility (indicated by the parentheses on  $E_x$ ) that these lines are formed by an impurity in the sample, since a 0.2% impurity of some nuclides would be enough to allow  $E1$  transitions to yield the observed intensities.

Our failure to detect transitions to the states at 198, 339, and 687 keV (whose existence was inferred in Ref. 17 from high-energy thermal-capture  $\gamma$  rays) probably means that these states do not exist, since our measurements are believed to be more sensitive. On the other hand, our failure to detect a few states inferred from the  $(d, p)$  mea-

surements implies only that they are not accessible to dipole radiation.

The bases for most of the spin and parity assignments in column 10 of Table IV are obvious from the data given in the table and in Fig. 14. Note that the assignments inferred from our data alone are in complete agreement with the results of Motz *et al.*<sup>17</sup> This is perhaps the most direct and convincing evidence for the validity of our approach.

Several states require special mention. No attempt is made to assign spins to the six states in the range 650–685 keV on the basis of the  $(\bar{n}, \gamma)$  intensity alone, because discrepancies in the apparent energies observed in our three spectra suggest that more than the six states listed are present in this range.

The problem of interpreting the intensities of the lines associated with the states at 634 and 693 keV has already been discussed in connection with Fig. 15. Our preferred interpretation is that both lines are formed by a superposition of two states, one with  $J^\pi = 2^+$  or  $5^+$  and the other with  $J^\pi = 3^-$  or  $4^-$ , but there is no definite evidence for this multiplicity of states. On the other hand, the presence of the negative-parity states is supported by the fact that they combine with other states to form rotational bands, as is discussed in Sec. IV A2.

No attempt is made to assign spins for most of the states with  $E_x > 875$  keV because here the spectrum suddenly appears to become too complex to be analyzed reliably.

## 2. Rotational-Band Structure

Since our measurements reveal the presence of

TABLE V. Rotational-band structure of  $^{166}\text{Ho}$ . Values of excitation energy  $E_x$  in parentheses give the energies of hypothetical states that are implied by the rotational-band structure. The excitation energies marked with an asterisk are states that are linked strongly enough to other bands to indicate that they are band heads. Intensities are in units of  $\gamma$  rays per  $10^4$  neutrons captured.

$J^\pi$	$E_x$ (keV)	$\Delta E_x$ (keV)	$E_\gamma$ (Ref. a) (keV)	$I_\gamma$ (Ref. a)	$2b(J+1)$ (keV)	$E_0$ (keV)	$b$ (keV)	Band label
$0^-$	0					0	8.99	A
$7^-$	5					-496	8.94	B
$1^-$	82.5					+65	8.83	C
$3^+$	*190.9					+86	8.75	D
$5^+$	*263.8					-6	(9.0)	Q
$6^+$	*294					-87	9.08	E
$4^+$	*372.0					+174	9.88	F
$1^+$	*426.0					+407	9.53	H
$2^+$	*430.1±0.2	51.5±0.3	51.81	23	51.0	+379	8.50	I
$3^+$	481.6±0.2	66.0±0.3	66.10	20	68.0			
$4^+$	547.6±0.2	86.6±0.3	86.36	10	85.0			
$5^+$	634.2±0.2		102.55	2	102.0			
$6^+$	(736.7)							
$4^+$	*558.3±0.2	96.6±0.5	95.95	12	96.0	+366	9.60	J
$5^+$	654.9±0.5		115.17	9	115.1			
$6^+$	(770.1)							
$3^+$	*592.0±0.3	79.1±0.6	78.87	5	78.6	+474	9.82	L
$4^+$	671.1±0.5	97.7±0.6	98.20	3	98.2			
$5^+$	768.8±0.3		118.41	2	117.8			
$6^+$	(887.2)							
$1^+$	*(567.0)				37.8			
$2^+$	604.8±0.3	57.5±0.6	57.19	8	56.6	+548	9.45	M
$3^+$	662.3±0.5	73.7±0.6	74.26	9	75.6			
$4^+$	736.0±0.2	95.1±0.3	94.64	20	94.5			
$5^+$	831.1±0.2		113.37	12	113.4			
$6^+$	(944.5)							
$4^+$	719.0±0.2	86.8±0.3	87.19	4	86.8	+545	8.68	O
$5^+$	805.8±0.2		104.30	5	104.2			
$6^+$	(910.1)							
$3^+$	814.3±0.2	75.5±0.4	75.75	7	75.7	+701	9.46	P
$4^+$	889.8±0.3	94.8±0.6	94.53	4	94.6			
$5^+$	984.6±0.5		113.17	2	113.5			
$6^+$	(1097.8)							
$2^-$	*416.3±0.4	54.4±2.1	53.34	9	53.0	+363	8.84	G
$3^-$	(470.7±2.0)	72.2±2.5	69.76	?	70.7			
$4^-$	542.9±1.0	85.1±1.4			88.3			
$5^-$	628.0±1.0							
$3^-$	*562.5±0.7	71.7±2.5	70.99	18	72.6	+454	9.07	K
$4^-$	(634.2±2.5)	91.6±3.0	89.60	10	90.7			
$5^-$	725.8±1.5		107.18	4	108.8			
$2^-$	638.0±1.0	55.0±3.0	57.19	8	57.2	+581	9.54	N
$3^-$	(693.0±2.5)	78.3±3.0	75.98	7	76.3			
$4^-$	771.3±1.5	95.8±2.0	95.77	9	95.4			
$5^-$	867.1±1.5							

<sup>a</sup>Motz *et al.*, Ref. 17.

many states that had not been reported previously, it seems worth while to try to expand on the band-structure analysis reported by Motz *et al.*<sup>17</sup> We will start by using only the information available from the average-resonance-capture spectra. Then our analysis is limited to a search for states of a given parity whose energies  $E_J$  form a sequence with energies at

$$E_J = E_0 + bJ(J+1), \quad (17)$$

(where  $E_0$  and  $b$  are constants) and whose  $(\bar{n}, \gamma)$  intensities are consistent with what is required by the spin  $J$ . Because of the limited range of  $J$  accessible to the primary capture  $\gamma$  radiation, one does not expect that all of the bands present can be identified from the  $(\bar{n}, \gamma)$  data alone. However, *all* 26 of the positive-parity states with  $J=2, 3, 4,$  or  $5$  and with  $E_x < 850$  keV can easily be fitted into band patterns; and in addition, most of the negative-parity states with  $E_x < 650$  keV can be fitted into bands. The members of each band are identified in the last column of Table IV by means of arbitrary labels, the characteristics of the bands are given in Table V, and the bands are plotted in Figs. 17, 18, and 19. Seven bands (A+C, B, D, E, F, H, and I) had been reported previously and nine more are revealed by the  $(\bar{n}, \gamma)$  measurements. The total (16) is probably the largest number of rotational bands reported to date in any nucleus.

The characteristics of the bands identified previously are summarized in the upper part of Table

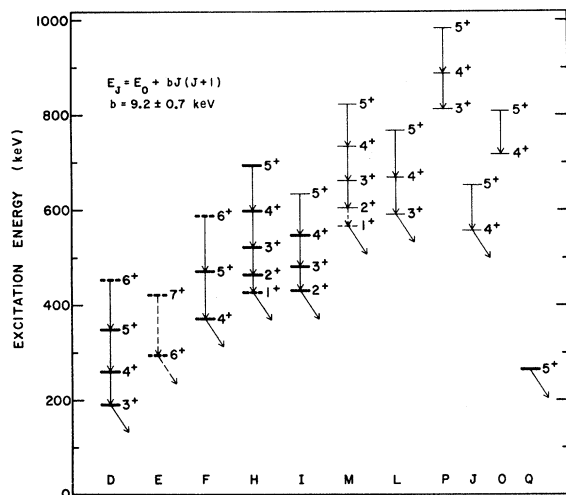


FIG. 17. Positive-parity rotational bands of  $^{166}\text{Ho}$ . The states represented by heavy lines were observed and identified previously by Motz *et al.* (Ref. 17). The connecting vertical lines represent  $\gamma$ -rays listed in Ref. 17, and the diagonal lines identify states from which relatively strong transitions are observed. The letters at the bottom are the band labels used in Tables IV and V.

V, where the spins and parities are listed only for the band heads. For each of the bands except A and B, the parameter  $b$  of Eq. (17) was calculated from the energies of the state with  $J=5$  and the state with the lowest  $J$  value observed; for band A, the upper limit for  $J$  was 6 rather than 5, and for band B it was 9.

Evidence for the new band structure in  $^{166}\text{Ho}$  is summarized in the lower part of Table V. Here the excitation energies  $E_x$  obtained from the average-resonance-capture measurements were used to construct sequences of states whose energies approximately satisfy Eq. (17) and whose spins are consistent with the average transition intensities; the constant  $b$  in Eq. (17) was allowed to vary by  $\pm 10\%$ . The optimum procedure in such an analysis is, starting with the lowest state, to search for sequences of states that form four-member bands. When all such bands have been formed, one then follows the same procedure for three-member bands; and then on to two-member bands and finally one-member bands. By first using up the states in the easily recognized four-member bands, this procedure minimizes the probability that a band pattern is formed by chance. Under the assumption that the excitation-energy differences  $\Delta E_x$  do not deviate from Eq. (17) by more than  $\pm 2\%$  (as seems to be the case for all except the  $0^-$  ground-state band, a special case), the chances that any of the positive-parity bands of Table V are formed by chance can be shown to be less than 1%; and the

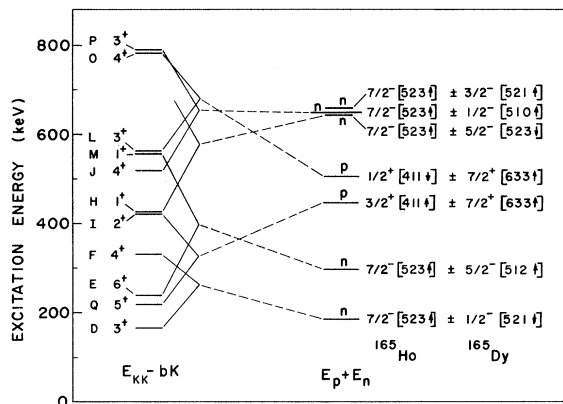


FIG. 18. Comparison of observed and predicted positive-parity bands in  $^{166}\text{Ho}$ . The labels and  $K$  values of the experimental bands are given on the left. The configurations of the single-particle states in  $^{165}\text{Ho}$  and  $^{165}\text{Dy}$  that combine to form states in  $^{166}\text{Ho}$  are given on the right. The letters  $n$  and  $p$  identify states that result from neutron-excited and proton-excited single-particle states, respectively. The first off-scale pair of bands is predicted to be at  $E_p + E_n = 1036$  keV.

fact that *all* of the positive-parity states with  $E_x < 850$  keV fit into bands suggests that the probability of any error is in fact much smaller than 1%.

A second step in the band analysis was to intercompare the energy differences  $\Delta E_x$ , the low-energy  $\gamma$  rays reported by Motz *et al.*,<sup>17</sup> and the excitation-energy differences  $2b(J+1)$  expected for an ideal rotational band. This comparison is shown in Table V. In all cases but one, there is a  $\gamma$  ray of the appropriate energy (within the experimental error) that has not been used in some other part of the decay scheme. These low-energy  $\gamma$  rays provide supporting evidence for the band structure, but little more, because the extremely large density of low-energy  $\gamma$ -ray lines allows some of the energy coincidences to occur by chance.

The spin assignments in column 11 of Table IV are based on the results of the band analysis and, for the lower-energy states, on the decay scheme constructed from the previously reported<sup>17</sup> low-energy  $\gamma$  rays. The justification for the assignments for bands A through F are given by Motz *et al.*<sup>17</sup> Our data confirm their analysis. The assignments based principally on the average-resonance-capture data are listed in columns 11 of Table IV as definite when three or more positive-parity states are fitted into the band, and are given as uncertain when only two states are involved. Also, the spins of all the negative-parity states fitted into new bands are listed as uncertain whenever the rotational pattern is the primary evidence, because not all states of this kind are detected and this greatly increases the probability of error.

Several aspects of Table V need to be mentioned.

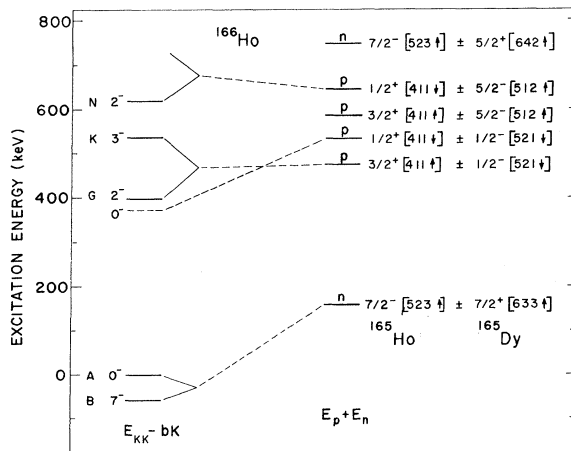


FIG. 19. Comparison of observed and predicted negative-parity bands in  $^{166}\text{Ho}$ . The notation and conventions in the figure are the same as in Fig. 18. Nine additional pairs of bands are predicted to lie in the range  $E_p + E_n = 900\text{--}1020$  keV.

The energy of each  $6^+$  state was calculated from the energy of the  $5^+$  state by adding the  $\gamma$ -ray energy (from the data of Motz *et al.*<sup>17</sup>) that appears to fit the rotational-band pattern. In no case has the  $6^+$  state been observed directly in our measurements, of course.

Band I was suggested previously, but the  $5^+$  member is new. Also, the spin information provided by the  $(\bar{n}, \gamma)$  data removes the former doubt about the reality of the band. Similarly, our data remove any doubt about the reality of band H.

TABLE VI. Decay patterns of low-energy states in  $^{166}\text{Ho}$ . Intensity  $I_\gamma$  is in units of  $\gamma$  rays per  $10^4$  neutrons captured.

Final state $J^\pi$	$\gamma$ ray (Ref. a)			Initial state	
	$E_x$ (eV)	$E_\gamma$ (eV)	$I_\gamma$	$E_x$ (eV)	$J^\pi$ from Decay Band
$1^-$	82 470	333 620	160	$416\,090 \pm 20$	
$3^-$	171 074	245 007	104	$416\,081 \pm 9$	
				$\langle E_x \rangle = 416\,084 \pm 8$	2 $2^-$
$2^-$	54 239	509 000	70	$563\,200 \pm 200$	
$3^-$	171 074	391 890	113	$562\,964 \pm 40$	
$4^-$	180 460	382 800	5	$563\,267 \pm 200$	
$(0, 1)^-$	373 080	189 890	1	$562\,970 \pm 60$	
$2^-$	416 084	146 808	9.5	$562\,892 \pm 12$	
				$\langle E_x \rangle = 562\,910 \pm 15$	2, 3 $3^-$
$2^-$	54 239	512 700	80	$566\,939 \pm 300$	
$(0, 1)^-$	373 080	194 529	13	$567\,609 \pm 35$	
$1^+$	425 990	141 599	13	$567\,589 \pm 35$	
$2^+$	430 030	137 510	2	$567\,540 \pm 25$	
$2^+$	464 480	103 116	5.2	$567\,596 \pm 40$	
				$\langle E_x \rangle = 567\,560 \pm 20$	1, 2 $1^+$
$3^+$	190 901	401 560	210	$592\,460 \pm 60$	
$4^+$	260 661	331 880	27	$592\,540 \pm 31$	
$2^+$	430 030	162 452	6.5	$592\,482 \pm 16$	
				$\langle E_x \rangle = 592\,500 \pm 15$	3 $3^+$
$(0, 1)^-$	373 080	231 957	24	$605\,037 \pm 40$	
$1^+$	425 990	179 032	25	$605\,022 \pm 32$	
$2^+$	464 480	140 544	9	$605\,024 \pm 35$	
$3^+$	522 000	83 049	5	$605\,049 \pm 40$	
				$\langle E_x \rangle = 605\,030 \pm 20$	2 $2^+$
$3^+$	481 845	152 450	1.6	$634\,295 \pm 35$	
$4^+$	547 956	86 359	10	$634\,315 \pm 20$	
				$\langle E_x \rangle = 634\,310 \pm 18$	3, 4, 5 $5^+$
$3^-$	171 074	467 300	30	$638\,374 \pm 300$	
$(0, 1)^-$	373 080	265 120	18	$638\,200 \pm 65$	
$1^+$	425 990	212 300	4	$638\,290 \pm 70$	
$2^+$	430 030	208 340	6.5	$638\,370 \pm 45$	
$3^+$	481 845	156 450	1.4	$638\,295 \pm 35$	
				$\langle E_x \rangle = 638\,320 \pm 30$	2 $2^-$
$4^+$	371 984	347 240	20	$719\,224 \pm 81$	
$3^+$	521 996	197 110	3	$719\,106 \pm 59$	
$4^+$	558 562	160 630	4	$719\,192 \pm 27$	
				$\langle E_x \rangle = 719\,170 \pm 25$	3, 4 $4^+$

<sup>a</sup>Motz *et al.*, Ref. 17.

Bands K and N depend on the assumption that the anomalously high intensities of the lines at 5549 and 5608 keV are caused by the presence of unresolved positive- and negative-parity states, as was discussed in Sec. IV A1. The fact that bands with reasonable characteristics can be formed in this way provides strong support for the reality of the unresolved states.

Similarly, band G depends on the assumption that a  $3^-$  state at roughly 470.7 keV is hidden by the  $E1$  transition to the  $5^+$  state at about the same energy. However, this assumption is just barely tenable, since it would reduce the intensity of the  $E1$  transition to an anomalously small value. Thus, the existence of band G is in some doubt, although the decay data (Sec. IV A3) imply that the 416-keV state is a band head.

The  $(\bar{n}, \gamma)$  data show that  $J^\pi = 2^+$  or  $5^+$  for the state at 263.8 keV. From this and the decay data presented in Ref. 17, one obtains a definite  $5^+$  assignment for the state. Thus, unless it is the only positive-parity state below 800 keV that is not in a rotational band, the 263.8-keV state must be a band head, since there is no  $4^+$  state that could be a member of its band.

### 3. Decay Scheme

Supporting evidence about some of the new states observed in our measurements can be obtained by using the low-energy  $\gamma$ -ray data of Motz *et al.*<sup>17</sup> to extend the decay scheme given by these authors. The newly derived decay patterns are summarized in Table VI. Here columns 1 and 2 describe groups of final states that appear to be fed from the initial state described by the last three columns. Within each such group, the initial-state energy given by  $E_x(\text{initial}) = E_x(\text{final}) + E_\gamma$  must be the same (within the experimental uncertainty) for all final states.

In spite of the possibility that the indicated coincidences in energy could occur by chance, most of the links shown in Table VI are believed to be reliable because they involve a fairly large fraction of the final states that can be fed by dipole transitions from the various initial states. All of the other states revealed by our measurements were also examined, but no convincing energy coincidences were observed. Even the decays out of the apparent band head at 814 keV cannot be convincingly identified, because the large number of accessible states at lower energy magnify the probability of chance coincidences. However, it should be mentioned that we looked only for coincidences involving decays from a given initial state to several final states, and it is possible that a more exhaustive search involving more complex patterns would yield other meaningful results.

The decay data in Table VI may be used to set restrictions on the spins of the initial states, if  $M1$  transitions are assumed to be much stronger than  $E2$  transitions—as is true<sup>17</sup> for the well-understood transitions between the states at lowest energy. In every case the results obtained in this way are consistent with the rotational-band assignments, as shown in Table VI. Moreover, when combined with the  $(\bar{n}, \gamma)$  results, the decay data allow the assignment of definite spins and parities to the states at 416, 592, 605, and 638 keV. These assignments are the same as those indicated by the band analysis.

The total intensity of transitions out of a band head is expected to be relatively large, since it should contain the intensity funneled down through the band. On this basis, the data in Table VI show that the states at 416, 563, and 592 keV are almost surely band heads, and that the  $5^+$  state at 634 keV is not a band head. The evidence concerning the other states of Table VI is inconclusive because it is uncertain whether certain strong lines with large errors in energy are in fact associated with the state in question. However, the decay data are at least consistent with our expectation that the states at 567, 638, and 719 keV are band heads.

The  $1^+$  state at 567 keV requires special mention, since it was not observed in the  $(\bar{n}, \gamma)$  measurements. The initial indication that the state might exist came from the observation that the total intensity emanating from the  $2^+$  state at 605 keV is less than would be expected for a band head. This led to the hypothesis that the band head is a previously undetected  $1^+$  state at the energy implied by the band, namely, at  $605 - 38 = 567$  keV. The decay data of Table VI confirm this hypothesis.

A similar search for a  $1^-$  state associated with the  $2^-$  state at 638 keV does not reveal any evidence for the  $1^-$  state. This implies that the 638-keV state is a band head.

An effort was made to obtain further information about the 373-keV state which is thought<sup>17</sup> to have negative parity and  $J=0$  or perhaps  $J=1$ . As discussed in Ref. 17, the low-energy  $\gamma$ -ray data suggest that the energy of the state is  $378.08 \pm 0.03$  keV. Table VI shows that several high-energy states appear to decay to the 373-keV state, and the energies involved imply that the excitation energy of the state in question is  $373.06 \pm 0.02$  keV. Also, the spins of the states involved suggest that the 373-keV state has  $J=1$ . However, this result is not considered to be definite, since some of the decay lines may be misplaced.

An effort to fit the 373-keV state into a rotational band also gave inconclusive results, although the intensities in the average-resonance-capture spectra are probably consistent with the existence

of a band made up of a  $0^-$  state at 373 keV, a  $1^-$  at  $387.4 \pm 3$  keV, a  $2^-$  at  $430 \pm 3$  keV, a  $3^-$  at  $475.5 \pm 1$  keV, a  $4^-$  at  $558 \pm 3$  keV, and a  $5^-$  at  $634 \pm 3$  keV. If present, the lines for the  $2^-$ ,  $4^-$ , and  $5^-$  states are hidden under the much stronger lines for positive-parity states. As is the case<sup>17</sup> for the  $0^-$  ground-state band, the even and odd members of the possible band based on a  $0^-$  state at 373 keV are displaced relative to each other. The  $b$  values are reasonable, namely, 9.25 keV for the even members and 8.81 keV for the odd members.

In summary, we have seen that *all* of the positive-parity states observed in average resonance capture can be fitted into rotational bands. Moreover, both the energies and the intensities of the low-energy  $\gamma$  rays that appear to be associated with these bands are consistent with what is expected. Thus, it seems highly probable that all of the spin assignments for the positive-parity states are correct, since a change in even one assignment would make it impossible to fit the others with a simple rotational pattern. This result is a most convincing demonstration of the importance of the *completeness* of the  $(\bar{n}, \gamma)$  data.

#### 4. Interpretation of Rotational Bands

As a final step in the analysis of the  $^{166}\text{Ho}$  bands we now attempt to interpret them in terms of a model in which  $^{166}\text{Ho}$  is assumed to consist of a  $^{164}\text{Dy}$  core strongly coupled to an extra neutron and proton; the states of this neutron and proton are described independently by Nilsson wave functions. Then as described elsewhere,<sup>17, 21-23</sup> each proton single-particle state combines with a neutron single-particle state to generate two rotational bands in  $^{166}\text{Ho}$ , and the spins of their band heads are  $K \equiv |\Omega_p \pm \Omega_n|$ , where  $\Omega_p$  and  $\Omega_n$  are the projections of the angular momenta of the odd proton and odd neutron on the body-fixed  $z$  axis. The energies of the rotational states are given<sup>23</sup> by

$$E_{JK} = E_p + E_n + b[J(J+1) - K^2], \quad (18)$$

where  $E_p$  and  $E_n$  are the single-particle energies of the odd proton and odd neutron.

The remarkable degree to which the model explains the essential features of the positive-parity bands in  $^{166}\text{Ho}$  is demonstrated in Fig. 18. Plotted on the left are values of  $(E_p + E_n)$  deduced from the  $^{166}\text{Ho}$  bands of Table IV by means of Eq. (18); that is, the quantities plotted are  $(E_{KK} - bK)$ , where  $E_{KK}$  is the experimental energy of the band head. On the right is given the corresponding quantity obtained from the measured single-particle energies of nuclear systems in which an odd proton or an odd neutron are coupled to a core of  $^{164}\text{Dy}$  or a nearby even-even nucleus. The energies of these

single-particle states were obtained from the experimental data recently summarized by Ogle *et al.*<sup>24</sup> The proton-excited states used are those listed for  $^{165}\text{Ho}$ ; and the neutron-excited states are those observed for  $^{165}\text{Dy}$ ,  $^{167}\text{Er}$ , and  $^{169}\text{Yb}$ , where the energies for  $^{165}\text{Dy}$  were used, when given. In view of the first-order nature of the comparison in Fig. 18, the experimental band-head energies were used without correction for various perturbing effects except that, in order to be consistent with Eq. (18), the values of  $E_p$  and  $E_n$  were calculated from the band-head energies by means of Eq. (5) in Chap. 4 of Ref. 23. The Nilsson orbitals involved are given on the right in the figure.

In the figure, the experimental bands of  $^{166}\text{Ho}$  were paired and linked to the available configurations in such a way as to satisfy the requirement  $K = |\Omega_p \pm \Omega_n|$ . Otherwise, the principal basis for the connections is the relative energies of the experimental and predicted bands, but the paired states are also required to be consistent with the Gallagher-Moszkowski coupling rules.<sup>23</sup> Also, the  $K^\pi = 1^+$  band at 426 keV is assigned to the configuration  $\frac{7}{2}^- [523] - \frac{5}{2}^- [523]$  because of the small  $\log ft$  value for the  $\beta$  decay from the ground state of  $^{166}\text{Dy}$  to the band head in  $^{166}\text{Ho}$ , as discussed in Ref. 17.

Although the observed positive-parity bands of  $^{166}\text{Ho}$  seem to be explained very well by Fig. 18, the indicated correspondence between the observed bands and the Nilsson orbitals cannot be considered definite because of the crudeness of the model. In particular, the states in the upper half of the figure probably do not have the simple single-particle character assumed by the model, and various coupling effects may pull other configurations into the energy-range of interest and exclude some of those that were used.

Probably some questions about the nature of the bands in Fig. 18 could be answered by quantitatively comparing the intensity "signature" of each band for  $(d, p)$  transitions with the theoretical prediction, as was done for the previously reported<sup>17, 22</sup> bands in  $^{166}\text{Ho}$ . However, this would demand  $(d, p)$  data of exceptional quality for  $E_x > 500$  keV because of the high density of states. In any case, we have not attempted to interpret the published  $(d, p)$  data in this way, since it would divert us from the main purpose of this paper—the exploration of a new experimental method.

Although much less complete, the results for the negative-parity bands are also consistent with the nuclear model outlined above, as is shown in Fig. 19. In particular, the low-lying  $0^-$  and  $7^-$  states are well explained and the new  $2^-$ ,  $3^-$ , and  $2^-$  bands are included among the 12 bands that are expected to lie in the energy range of interest. It would require another major advance in experi-

mental technique to permit the observation of the other predicted (Fig. 19) negative-parity bands.

#### 5. Radiative Transitions to Proton-Excited States

In an extensive series of  $(n, \gamma)$  and  $(d, p)$  measurements Sheline<sup>25</sup> and associates have found few if any cases in which high-energy transitions following thermal-neutron capture directly populate known proton-excited states in deformed heavy nuclei. This experimental observation has led to the suggestion that the high-energy transitions in the  $(n, \gamma)$  reaction result from a direct process with selection rules similar to the  $(d, p)$  reaction, as discussed earlier.<sup>25, 26</sup> This suggestion is, of course, in complete disagreement with our working hypothesis that radiative neutron capture is a compound-nucleus reaction whose cross section is insensitive to the structure of the final state.

Since all positive-parity states observed in our measurements on <sup>166</sup>Ho are fed with effectively equal intensity (except for well-understood factors such as the energy dependence), the results presented in Fig. 18 seem to contradict the direct-reaction hypothesis for the high-energy radiative transitions. The key question is whether any of these states are surely proton-excited states; in other words, is it possible that the bands attributed in Fig. 18 to the excitation of an odd proton could be explained in terms of either known or unknown intrinsic states in the odd-neutron system while the odd proton remains in the ground state? Clearly this possibility cannot be excluded for bands L and O or any other band at such a high excitation energy, in view of the complexity of the structure, the incompleteness of information about single-particle levels, and the crudeness of our nuclear model. However, the suggested assignments of bands Q and I to proton-excited configurations are less easily dismissed, since there is a considerable gap (Fig. 18) between the energy of the observed bands and the expected energy for the closest alternate neutron-excited configuration  $\frac{7}{2}^- [523] \pm \frac{3}{2}^- [521]$ .

Similarly, Fig. 19 strongly suggests that at least the lower  $2^-$  band fed by  $M1$  radiation involves excitation of an odd proton, since (according to the data of Ref. 24) the bands connected with the closest appropriate neutron-excited configuration  $\frac{7}{2}^- [523] \pm \frac{3}{2}^+ [402]$  are expected to be about 500 keV higher in energy than is observed.

In principle the  $(d, p)$  data should throw some light on the nature of the bands attributed in Fig. 18 to proton-excited configurations, since proton-excited states should be populated much more weakly by the  $(d, p)$  reaction than are neutron-excited states. A qualitative examination of the published  $(d, p)$  data<sup>17, 22</sup> show (a) that the  $(d, p)$  transi-

tion to the one state of band Q is not detected, very possibly because it is badly obscured by the strong line at 261 keV; (b) that the lines for the  $2^+$  and  $3^+$  states of band I also are unobserved and this shows that they are very weak, since there are no strong nearby lines to obscure them; (c) that there are  $(d, p)$  lines of intermediate intensity in the neighborhood of the  $4^+$  state of I and the  $4^+$  state of J, but there are at least three other states at about the same energies, so that the interpretation of the  $(d, p)$  data is not clear; and (d) that, similarly, at higher energy the density of states is too great to allow a convincing interpretation of the weak  $(d, p)$  lines at the energies that are consistent with some of the states attributed to excited-proton configurations. Thus, the  $(d, p)$  data are consistent with our interpretation of bands Q and I as proton-excited states.

Although the result is not conclusive, our data and the above discussion strongly suggest that the average widths of radiative transitions to some proton-excited states in <sup>166</sup>Ho are effectively the same as the widths for the neutron-excited states. What is needed to settle the issue conclusively, however, is a positive identification of proton-excited states in <sup>166</sup>Ho by means of a reaction such as <sup>167</sup>Er( $d, ^3$ He)<sup>166</sup>Ho.

### B. <sup>167</sup>Er( $n, \gamma$ )<sup>168</sup>Er

#### 1. Average-Resonance-Capture Data

An outline of our results for <sup>168</sup>Er has been reported previously.<sup>8</sup> Average-resonance-capture spectra were measured for the three samples of normal erbium described in Table II. In addition, a small sample of <sup>164</sup>Er was measured to identify lines from <sup>164</sup>Er( $n, \gamma$ )<sup>165</sup>Er.

Of the samples of natural erbium, the one with the 0.43-g/cm<sup>2</sup> absorber gives the best compromise between signal-to-background ratio and width of the neutron-capture spectrum, and hence it is the best source of information about average  $\gamma$ -ray intensities. The intensities observed with the 0.17-g/cm<sup>2</sup> absorber are also sufficiently free of Porter-Thomas fluctuations to be useful for spectroscopic purposes; a part of the spectrum for the 0.17-g/cm<sup>2</sup> absorber is given in Ref. 8.

By far the best run for determining  $\gamma$ -ray energies and for detecting unresolved lines is that for the thinnest absorber (0.03 g/cm<sup>2</sup>). A part of the spectrum is given in Fig. 20. The dominant contributors to this spectrum are the very-low-energy resonances that also contribute heavily to the thermal cross section. However, the  $(\bar{n}, \gamma)$  spectrum has the important advantage of being much freer from the influence of sample impurities than is the thermal-capture spectrum. Indeed, although

our Er sample is advertised as being at least 99.9% pure, the thermal-capture spectrum was found to be almost useless because of the presence of a large number of weak lines of unknown origin. None of these impurity lines are visible in the  $(\bar{n}, \gamma)$  spectrum.

The first task in the analysis of the Er spectra is the isotopic assignment of the transitions. The product isotopes  $^{165}\text{Er}$ ,  $^{167}\text{Er}$ ,  $^{168}\text{Er}$ , and  $^{169}\text{Er}$  are expected to have detectable lines in the energy range of interest. To identify the lines in  $^{168}\text{Er}$ , which are of principal interest to us, we assume that the work of Michaelis *et al.*<sup>27</sup> has revealed all states in  $^{167}\text{Er}$  that could be populated by dipole transitions with  $E_\gamma > 5600$  keV and that Harlan and Sheline<sup>28</sup> have revealed all such states in  $^{169}\text{Er}$ ; these states in  $^{167}\text{Er}$  and  $^{169}\text{Er}$  are considered in Sec. IV C. Because of the higher neutron binding energy of  $^{164}\text{Er}$ , it seemed unlikely that all of the transitions in  $^{165}\text{Er}$  could be identified from previous knowledge. Thus, we measured the spectrum of a small enriched sample of  $^{164}\text{Er}$ . The states attributed to  $^{165}\text{Er}$  from this measurement are discussed in Sec. IV D. Lines from  $^{162}\text{Er}(n, \gamma)^{168}\text{Er}$

are too weak to be detected in any of the spectra.

The  $\gamma$ -ray lines that are not attributable to  $^{165}\text{Er}$ ,  $^{167}\text{Er}$ , and  $^{169}\text{Er}$  (and to a few background lines) are assumed to be from  $^{168}\text{Er}$ . The characteristics of these transitions and the states inferred from them are given in Table VII. The energies and intensities for states with  $E_x < 1825$  keV are the same as reported previously.<sup>8</sup> At that time, many of the states had not been reported elsewhere, but their reality has recently been confirmed by Michaelis, Weller, and Ottmar (MWO).<sup>29</sup>

The energies of the  $\gamma$  rays were determined in the same way as was described above for holmium. For  $^{168}\text{Er}$ , the energy of the ground-state transition was established by using the value 1094.1 keV for the energy of the  $4^-$  state at about that energy. The excitation energies inferred from the  $\gamma$ -ray energy differences are seen to be in excellent agreement with the accurate values obtained from the low-energy  $\gamma$ -ray data.<sup>29,30</sup>

The  $\gamma$ -ray intensities measured in the run with the 0.43-g/cm<sup>2</sup> absorber are given in Table VII. The very small intensities of the transitions to the  $6^+$  states at 549 and 1264 keV show that the contri-

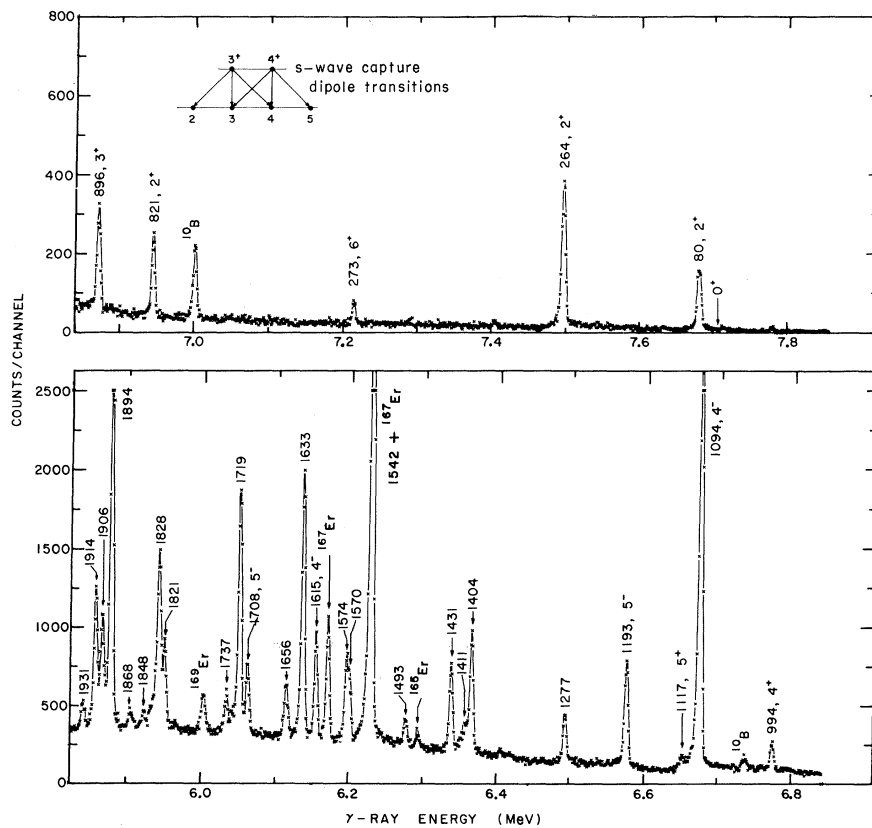


FIG. 20. Average-resonance-capture spectrum for the normal erbium sample with a very thin (0.027 g/cm<sup>2</sup>)  $^{10}\text{B}$  absorber. The lines from the reaction  $^{161}\text{Er}(n, \gamma)^{168}\text{Er}$  are labeled with the excitation energy (keV) and with the  $J^\pi$  value of the final state (if given in Ref. 31), and the transitions in  $^{165}\text{Er}$ ,  $^{167}\text{Er}$ , and  $^{169}\text{Er}$  are identified.

TABLE VII. High-energy transitions in  $^{167}\text{Er}(\bar{n}, \gamma)^{168}\text{Er}$  and states of  $^{168}\text{Er}$ . The random errors for  $E_\gamma$  are the same as those given for  $E_x$ , and the absolute values of  $E_\gamma$  are uncertain by an additional 0.6 keV. The symbol  $n$  under "spin assignments" means  $J=2, 3, 4$ , or 5.

This work		$E_x$ (keV) from other work		Relative intensity $I_\gamma E_\gamma^{-3}$	Spin and parity assignments			Band
$E_\gamma$ (keV)	$E_x$ (keV)	Low-energy $\gamma$ rays (Refs. a, b)	$(d, p)$ (Ref. c)		Previous work (Refs. b, c)	Present work	Composite	
7770.6	0	0	0	<2	0 <sup>+</sup>		0 <sup>+</sup>	A
7691.1	79.5±0.3	79.8 <sup>a</sup>	79	34±2	2 <sup>+</sup>	2, 5 <sup>+</sup>	2 <sup>+</sup>	A
7507.0	263.6±0.3	264.1 <sup>a</sup>	264	55±2	4 <sup>+</sup>	3, 4 <sup>+</sup>	4 <sup>+</sup>	A
7222.6	548.0±1.5	548.7 <sup>a</sup>	550	<6	6 <sup>+</sup>		6 <sup>+</sup>	A
6949.5	821.1±0.3	821.1 <sup>a</sup>	823	23±3	2 <sup>+</sup>	2, 3 <sup>+</sup>	2 <sup>+</sup>	B
6874.7	895.9±0.3	895.8 <sup>a</sup>	899	51±4	3 <sup>+</sup>	3, 4 <sup>+</sup>	3 <sup>+</sup>	B
6776.4	994.2±0.3	994.8 <sup>a</sup>	998	52±4	4 <sup>+</sup>	3, 4 <sup>+</sup>	4 <sup>+</sup>	B
6676.6	1094.0±0.2	1094.0 <sup>a</sup>	1094	375±7	4 <sup>-</sup>	3, 4 <sup>-</sup>	4 <sup>-</sup>	C
6653.7	1116.9±0.6	1117.6 <sup>a</sup>	~1110	27±4	5 <sup>+</sup>	2, 5 <sup>+</sup>	5 <sup>+</sup>	B
6577.4	1193.2±0.2	1193.0 <sup>a</sup>	1193	142±6	5 <sup>-</sup>	2, 5 <sup>-</sup>	5 <sup>-</sup>	C
		1263.9 <sup>a</sup>	~1265	<7	6 <sup>+</sup>		6 <sup>+</sup>	B
6494.1	1276.5±0.3	1276.5 <sup>a</sup>		25±4	2 <sup>+</sup>	2, 5 <sup>+</sup>	2 <sup>+</sup>	D
6366.7	1403.9±0.2	1403.9		151±6	2 <sup>-</sup>	2, 5 <sup>-</sup>	2 <sup>-</sup>	E
6359.3	1411.3±1.0	1411.1		28±9	4 <sup>+</sup>	$n^+$	4 <sup>+</sup>	D
6339.2	1431.4±0.2	1431.5 <sup>a</sup>		219±7	3 <sup>-</sup>	$n^-$	3 <sup>-</sup>	E
6277.4	1493.2±0.5	1493.4		39±7	3, 4 <sup>+</sup>	3, 4 <sup>+</sup>	3, 4 <sup>+</sup>	
6228.7	1541.9±1.0	1541.6 <sup>a</sup>	1542	~800	3 <sup>-</sup>	3, 4 <sup>-</sup>	3 <sup>-</sup>	F
	1541.9±1.0					3, 4 <sup>-</sup>	4 <sup>-</sup>	E
6200.9	1569.7±1.0	1569.5		103±25	2 <sup>-</sup>	2, 5 <sup>-</sup>	2 <sup>-</sup>	G
6196.7	1573.9±0.7	1574.2		160±30	5 <sup>-</sup>	2, 5 <sup>-</sup>	5 <sup>-</sup>	E
6155.3	1615.3±0.2	1615.4 <sup>a</sup>	1615	310±9	4 <sup>-</sup>	3, 4 <sup>-</sup>	4 <sup>-</sup>	F
6137.2	1633.4±0.2	1633.6		269±11	3 <sup>-</sup>	3, 4 <sup>-</sup>	3 <sup>-</sup>	G
6118.6	1652.0±1.0	1653.7		47±8	(4 <sup>+</sup> )	3, 4 <sup>+</sup>	(3) <sup>+</sup>	H
6114.8	1655.8±0.5	1656.6		52±8	3, 4 <sup>+</sup>	3, 4 <sup>+</sup>	3, 4 <sup>+</sup>	
6062.3	1708.3±0.3	1708.0 <sup>a</sup>	1709	112±12	5 <sup>-</sup>	2, 5 <sup>-</sup>	5 <sup>-</sup>	F
6051.3	1719.3±0.2	1719.2		226±9	4 <sup>-</sup>	3, 4 <sup>-</sup>	4 <sup>-</sup>	G
6034.1	1736.5±0.5	1737.5		51±8	4 <sup>+</sup>	3, 4 <sup>+</sup>	4 <sup>+</sup>	H
5950.0	1820.6±0.3	1820.3		241±24	3 <sup>-</sup>	3, 4 <sup>-</sup>	3 <sup>-</sup>	I
5942.3	1828.3±0.2	1827.6		276±50	5 <sup>-</sup>	3, 4 <sup>-</sup>	5 <sup>-</sup>	G
	1828.3±1.0					2, 5 <sup>-</sup>	(2) <sup>-</sup>	J
5922.3	1848.3±0.4			14±7		2, 5 <sup>+</sup>	(5) <sup>+</sup>	H
5876.9	1893.7±0.2	1893.0		381±25	3 <sup>-</sup>	3, 4 <sup>-</sup>	(4) <sup>-</sup>	I
5864.3	1906.3±0.3			271±25		3, 4 <sup>-</sup>	(3) <sup>-</sup>	J
5856.6	1914.0±0.3	1914.4		249±15	3 <sup>-</sup>	3, 4 <sup>-</sup>	3 <sup>-</sup>	
5839.8	1930.8±0.8			20±7		$n^+$		
5798.2	1972.4±0.5			108±15		2, 5 <sup>-</sup>	2, 5 <sup>-</sup>	
5787.5	1983.1±0.8	1983.1		122±15	(4 <sup>-</sup> )	2, 5 <sup>-</sup>	(5) <sup>-</sup>	I
5775.0	1995.6±2.0			96±30		2, 5 <sup>-</sup>	2, 5 <sup>-</sup>	
5770.5	2000.1±1.0			280±30		3, 4 <sup>-</sup>	(4) <sup>-</sup>	J
5748.4	2022.2±0.2			233±15		3, 4 <sup>-</sup>	3, 4 <sup>-</sup>	
5739.2	2031.4±0.8			30±10		$n^+$	$n^+$	
5714.6	2056.0±1.5			<30				
5710.5	2060.1±0.4			280±20		3, 4 <sup>-</sup>	3, 4 <sup>-</sup>	
5689.7	2080.9±2.0			60±20				
5661.7	2108.9±2.0			20±7		$n^+$	$n^+$	
5641.4	2129.2±0.5			106±20		2, 5 <sup>-</sup>	(5) <sup>-</sup>	J
5622.2	2148.4±0.2			104±10		2, 5 <sup>-</sup>	2, 5 <sup>-</sup>	

<sup>a</sup>Koch, Ref. 30.<sup>b</sup>Michaelis *et al.*, Ref. 29.<sup>c</sup>Harlan and Sheline, Ref. 31.

butions of  $E2$  transitions may be ignored. Also, the influence of  $p$ -wave capture is weak enough to be ignored, as is indicated by the fact that the  $\gamma$ -ray lines for transitions to positive-parity states are only slightly broader than those for transitions to negative-parity states. Thus, in the same way as for Ho, the  $\gamma$ -ray intensities for  $^{168}\text{Er}$  are expected to fall into the four groups allowed by  $s$ -wave capture followed by dipole radiation.

The general behavior of the  $\gamma$ -ray intensities is summarized in Fig. 21. Here one sees that most of the data points fall along four lines, as expected. This expected behavior is also demonstrated by the histogram given in Fig. 16.

The positions and shapes of the lines in Fig. 21 were determined in the same way as described for Ho, i.e., by making a plot of  $I_\gamma E_\gamma^{-3} Q_J^{-1}$  versus  $E_\gamma$ ; a plot of this kind is given in Ref. 26. All of the positive-parity points are consistent with the arbitrary straight lines drawn through them, if one takes account of the large error for the intensity of the  $4^+$  state at 1411 keV ( $E_\gamma = 6359$  keV). With a few exceptions, the negative-parity points are also consistent with a straight-line energy dependence, and the slope of the best fit is about what is expected from the giant-resonance description of the transitions.

The parities and limits on the spins of most of the states may be inferred immediately from Fig. 21. As is seen in Table VII, these  $(\bar{n}, \gamma)$  assignments are almost all consistent with those inferred<sup>29</sup> from the decay scheme constructed from the low-energy  $\gamma$  rays and from a band-structure analysis<sup>29,31</sup> of the states. This agreement is especially significant since many of our assignments were published<sup>8</sup> before part of the band-structure analysis was made. Significant problems arise only for a few states.

*1431 keV.* This state is bothersome, since its intensity is intermediate between what is expected for  $J=3$  or 4 and  $J=2$  or 5. It is tempting to suggest that the line results from a pair of unresolved states, one with  $J^\pi = 2^-$  or  $5^-$  and one with  $J^\pi = 3^+$  or  $4^+$ . The line shape provides some support for this suggestion, since in two out of the three spectra the line in question is about 10% wider than any neighboring line. However, MWO<sup>29</sup> assign  $J^\pi = 3^-$  to this state. For this assignment, our data are difficult to reconcile with the statistical model, since an intensity as low as was observed can occur with a probability of only about 0.1%.

*1542 keV.* The line associated with this state coincides in energy with a transition in  $^{167}\text{Er}$ , and the intensity given in Table VII has had this contri-

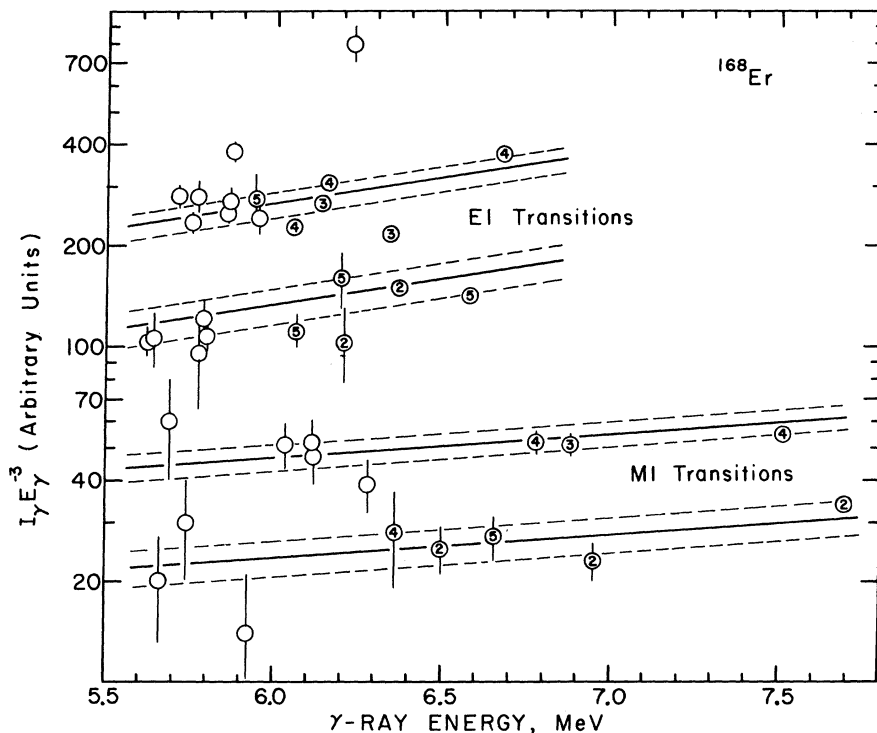


FIG. 21. Plot of  $I_\gamma E_\gamma^{-3}$  versus  $E_\gamma$  for transitions from  $^{167}\text{Er}(\bar{n}, \gamma)^{168}\text{Er}$ . The numbers in some of the circles are the final-state spins given by MWO (Ref. 29). The error bars represent rms experimental errors; when no error bar is given, the error is smaller than the data point. The dashed lines show the magnitudes of the standard errors expected from Porter-Thomas fluctuations.

bution subtracted. The remainder is very much larger than any other intensity for  $^{168}\text{Er}$ , and this indicates that two unresolved states are present in  $^{168}\text{Er}$ . Indeed, the intensity is so great that one can be confident that both of these states have  $J^\pi = 3^-$  or  $4^-$ .

*1828 keV.* Our spin assignment for this state is tentative because the spectrum is so complex at this energy. Thus the apparent discrepancy between our spin assignment and that inferred by MWO<sup>29</sup> from a band-structure analysis is not very surprising. The discrepancy strongly suggests that there are two states at about 1828 keV with  $J^\pi = 2^-$  or  $5^-$ .

*1866 keV.* A transition originally attributed<sup>8</sup> to a state in  $^{168}\text{Er}$  at this energy is now assigned to  $^{167}\text{Er}$ .

*1893 keV.* The intensity associated with this state is so high as to imply the presence of two unresolved states, one with  $J^\pi = 3^-$  or  $4^-$  and one with  $J^\pi = 2^-$  or  $5^-$ .

*>1700 keV.* It should be borne in mind that the numerous strong lines in  $^{167}\text{Er}$  and  $^{169}\text{Er}$  with  $E_\gamma < 6000$  keV might obscure even  $E1$  transitions to some states in  $^{168}\text{Er}$  with  $E_x > 1700$  keV.

No effort was made to analyze the spectrum for  $E_\gamma < 5600$  keV because of uncertainties about the isotopic assignments of the lines.

## 2. Rotational-Band Structure

Most of the low-energy states of  $^{168}\text{Er}$  have already been ordered into rotational bands. Bands A, B, C, and F in Table VII were reported by Harlan and Sheline<sup>31</sup> and bands D, E, and G were recently added by MWO.<sup>29</sup> The  $(\bar{n}, \gamma)$  data are in every case consistent with these assignments (with the possible exception of the 1431-keV state, as discussed in Sec. IV B1), but bands D and E could

TABLE VIII. Some possible rotational bands of  $^{168}\text{Er}$ . The energies  $E_x$  and  $\Delta E_x$  come from the  $(\bar{n}, \gamma)$  data, and the quantity  $2b(J+1)$  is the energy difference between adjacent states in an ideal rotational band.

$J^\pi$	$E_x$ (keV)	$\Delta E_x$ (keV)	$2b(J+1)$ (keV)	$E_0$ (keV)	$b$ (keV)	Band label
$3^+$	$1652.0 \pm 1.0$	$84.5 \pm 1.2$	84.5	1527	10.57	H
$4^+$	$1736.5 \pm 0.5$	$111.8 \pm 0.7$	105.7			
$5^+$	$1848.3 \pm 0.4$					
$3^-$	$1820.6 \pm 0.3$	$73.1 \pm 0.4$	73.1	1711	9.13	I
$4^-$	$1893.7 \pm 0.2$	$89.3 \pm 0.9$	91.3			
$5^-$	$1983.0 \pm 0.8$					
$2^-$	$1828.3 \pm 1.0$	$78.0 \pm 1.1$	75.2	1753	12.52	J
$3^-$	$1906.3 \pm 0.3$	$93.8 \pm 1.1$	100.2			
$4^-$	$2000.1 \pm 1.0$	$129.1 \pm 1.2$	125.2			
$5^-$	$2129.2 \pm 0.5$					

not have been identified reliably from our data alone. On the other hand, only the average-resonance-capture data have directly revealed the presence of two states with  $J^\pi = 3^-$  or  $4^-$  at about 1592 keV, and one of these states is required as the  $4^-$  state of the octopole band E, which Coriolis mixing has badly distorted<sup>29</sup> from a simple rotational pattern.

Bands H, I, and J in Tables VII and VIII result from an effort to fit the remaining states into rotational-band patterns in the same way as was done for  $^{166}\text{Ho}$ . Here, however, the procedure is much less successful than for  $^{166}\text{Ho}$ , perhaps because the spectra are so complex that many positive-parity and some negative-parity states could have been missed. Consequently, the new bands are not considered to be well established.

Band H is little more than a suggestion, since it depends principally on the spacing of two states with  $J^\pi = 3^+$  or  $4^+$ . The 1848-keV state may not be the  $5^+$  member of this band, since the energy difference between the  $5^+$  and  $4^+$  members is too great and a  $5^+$  state at a more appropriate energy would probably be obscured by a strong line in  $^{169}\text{Er}$ .

Band I is fairly convincing in that its three members conform well to a simple rotational pattern. However, the  $4^-$  assignment for the 1893-keV state disagrees with the  $3^-$  assignment of MWO.<sup>29</sup> We choose to ignore the  $3^-$  assignment because it is based mainly on the intensities of three low-energy  $\gamma$  rays, and an error in the placement of one of these in the decay scheme would negate the assignment.

Band J is not very convincing because the energy differences do not satisfy a simple rotational pattern.

The "composite" spin assignments given in the next to the last column of Table VII are the values required by the rotational bands listed in the last column. Obviously, the assignments in parentheses are quite uncertain.

## C. $^{166}\text{Er}(n, \gamma)^{167}\text{Er}$ and $^{168}\text{Er}(n, \gamma)^{169}\text{Er}$

As mentioned in Sec. IV B1, lines in the spectra obtained with natural Er samples were assigned to the reaction  $^{166}\text{Er}(n, \gamma)^{167}\text{Er}$  when they correspond to  $^{167}\text{Er}$  states observed by Michaelis *et al.*,<sup>27</sup> and others were assigned to  $^{168}\text{Er}(n, \gamma)^{169}\text{Er}$  on the basis of the binding energy of  $^{168}\text{Er}$  and the states of  $^{169}\text{Er}$  reported by Harlan and Sheline.<sup>28</sup> These transitions are listed in Table IX. For  $^{167}\text{Er}$ , the energy of the ground-state transition is determined by assuming that the excitation energy of the first  $\frac{3}{2}^-$  state is 264.6 keV. We observe transitions to all of the previously reported states that

can be reached by dipole transitions, and the  $\gamma$ -ray intensities are consistent with the previous spin and parity assignments. The ratio of  $E1$  to  $M1$  transition strengths in  $^{167}\text{Er}$  is about the same as for  $^{168}\text{Er}$ .

#### D. $^{164}\text{Er}(n,\gamma)^{165}\text{Er}$

The reaction  $^{164}\text{Er}(n,\gamma)^{165}\text{Er}$  was studied with a 1-g sample enriched in  $^{164}\text{Er}$  and with the  $^{10}\text{B}$  absorber described in Table II. The isotopic composition of the sample was 0.1%  $^{162}\text{Er}$ , 62.7%  $^{164}\text{Er}$ , 20.6%  $^{166}\text{Er}$ , 7.9%  $^{167}\text{Er}$ , 6.4%  $^{168}\text{Er}$ , and 2.3%  $^{170}\text{Er}$ . Thus, in the energy range of interest, the spectrum contains strong lines from capture in  $^{164}\text{Er}$ ,  $^{166}\text{Er}$ ,  $^{167}\text{Er}$ , and  $^{168}\text{Er}$ , but the relative intensities of these lines are different from those for the natural Er sample.

A sensitive and objective way to identify the lines from  $^{164}\text{Er}(n,\gamma)^{165}\text{Er}$  is to calculate the ratio of the intensity of each line in the spectrum for the enriched sample to that for the normal sample. This ratio is about 250 (arbitrary normalization) for  $^{165}\text{Er}$  lines and  $8 \pm 4$  for all other lines observed. Thus, even when a line in  $^{165}\text{Er}$  is unre-

solved from one in another isotope, its presence is easily detected.

The transitions assigned to  $^{165}\text{Er}$  are listed in Table X. All but one of these transitions are associated with states reported by Abdurazakov *et al.*,<sup>32</sup> and the intensities are consistent with their spin and parity assignments except for the states they report at 746 and 1032 keV.

#### E. $^{155}\text{Gd}(n,\gamma)^{156}\text{Gd}$ and $^{157}\text{Gd}(n,\gamma)^{158}\text{Gd}$

Only one sample of gadolinium was studied – a metallic sample of the natural element with a thick (0.48 g/cm<sup>2</sup>) absorber of  $^{10}\text{B}$ . A part of the spectrum obtained is given in Fig. 22.

Because of the high neutron binding energies of  $^{155}\text{Gd}$  and  $^{157}\text{Gd}$ , capture in these nuclides is expected to dominate the high-energy part of the spectrum. Since both of these targets have  $J^\pi = \frac{3}{2}^-$ , the initial states formed by  $s$ -wave capture have  $J_i^\pi = 1^-$  or  $2^-$ , and  $E1$  transitions from these states feed positive-parity final states with  $J = 0, 1, 2$ , or  $3$ . Calculations based on Eq. (11) show that the relative values of the average intensities of lines associated with these final states should be 0.93,

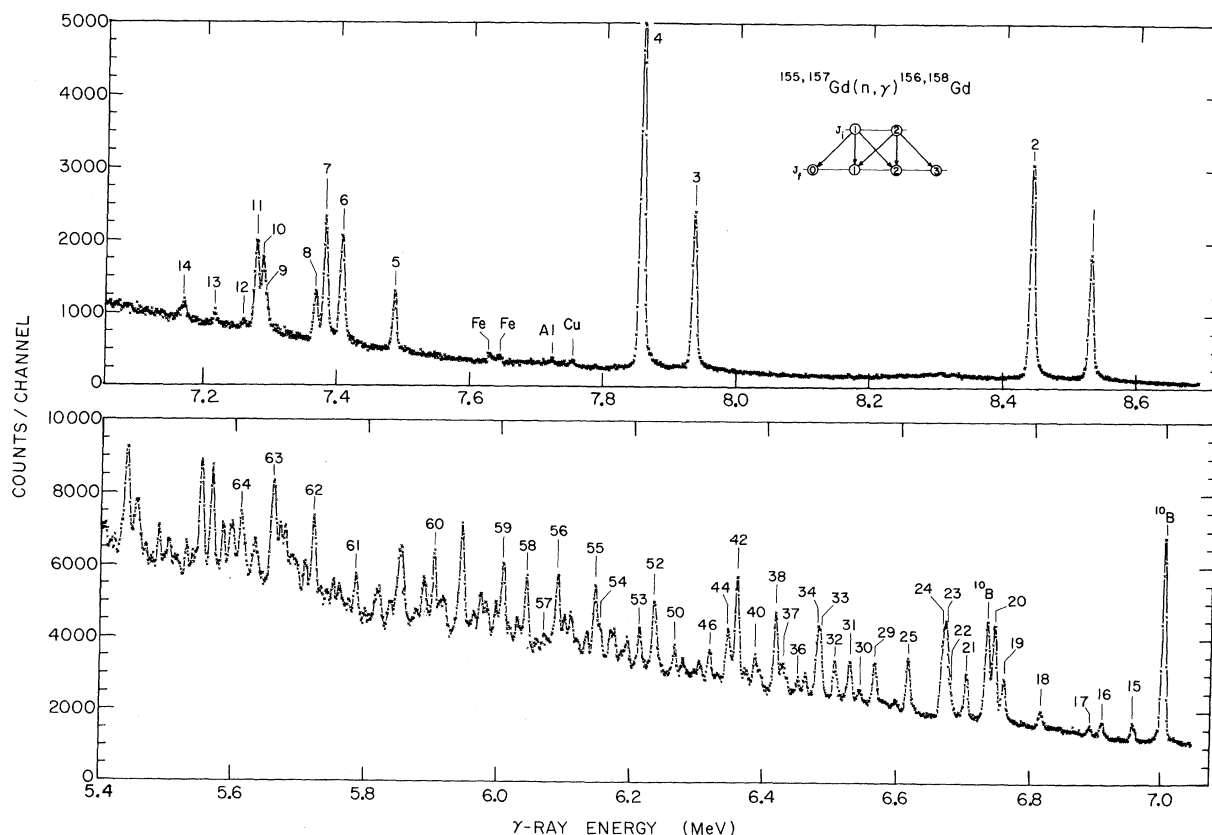


FIG. 22. Average-resonance-capture spectrum for normal gadolinium. The line numbers are the same as are used in Tables XI, XII, and XIII.

TABLE IX. States of  $^{167}\text{Er}$  and  $^{169}\text{Er}$ . The random errors for  $E_\gamma$  are the same as those given for  $E_x$ , and the absolute values of  $E_\gamma$  are uncertain by an additional 0.6 keV. Excitation energies used for normalization are marked with an asterisk.  $\gamma$ -ray intensities are in arbitrary units.

This work		Previous work		
$E_\gamma$ (keV)	$E_x$ (keV)	$I_\gamma E_\gamma^{-3}$	$E_x$ (keV)	$J^\pi$ Ref.
States of $^{167}\text{Er}$				
6435.8		<5	0	$\frac{7}{2}^+$ a
6228.6	207.2±1.0	<990	207.8	$\frac{1}{2}^-$ a
6171.2	*264.6±0.2	503±25	264.6	$\frac{3}{2}^-$ a
5904.0	531.8±0.4	100±15	531.5	$\frac{3}{2}^-$ a
		<10	591.8	$\frac{5}{2}^+$ a
5682.0	753.8±0.8	500±40	752.8	$\frac{3}{2}^-$ a
5673.1	762.7±0.8	478±40	763.5	$\frac{1}{2}^-$ a
5634.8	801.0±0.3	576±25	801.7	$\frac{3}{2}^-$ a
States of $^{169}\text{Er}$				
6002.5	*0 ±0.5	403±20	0	$\frac{1}{2}^-$ b
5936.9	65.6±2.0	250±90	69	$\frac{3}{2}^-$ b

<sup>a</sup>Michaelis *et al.*, Ref. 27.

<sup>b</sup>Harlan and Sheline, Ref. 28.

2.0, 2.0, and 1.07, respectively, and in the discussion below we assume that 0.93 and 1.07 are not distinguishable from unity.

The interpretation of the Gd data is complicated by the presence of several isotopes, and our first task is the isotopic identification of the observed lines. This is done in Tables XI and XII by comparing the energies of our  $\gamma$ -ray lines and the states implied by them with the energies of the states reported previously. Here we make an isotopic assignment when the energy of a state derived from our spectrum is in good agreement with the energy of a previously reported state in which we have confidence. In this respect, the results of capture  $\gamma$ -ray measurements<sup>33-35</sup> with separated isotopes are especially useful, since the high-energy transitions in these data are almost surely the ones we observe. However, a drawback of these data is that the resolution width is sometimes<sup>33</sup> too broad to allow a one-to-one correspondence between the various sets of lines to be established with certainty. The columns labeled "(*d, p*)" in Tables XI and XII give the results compiled by Groshev *et al.*<sup>36</sup> from measurements on (*d, p*) and other reactions, excluding the (*n, \gamma*) reaction. These data are assumed to be reliable but, because of selection rules, the states observed in this way are not necessarily the ones that we observe. Similarly, the states obtained from radioactive decay<sup>37</sup> must be used with caution.

The intensities of the  $\gamma$ -ray lines in our spec-

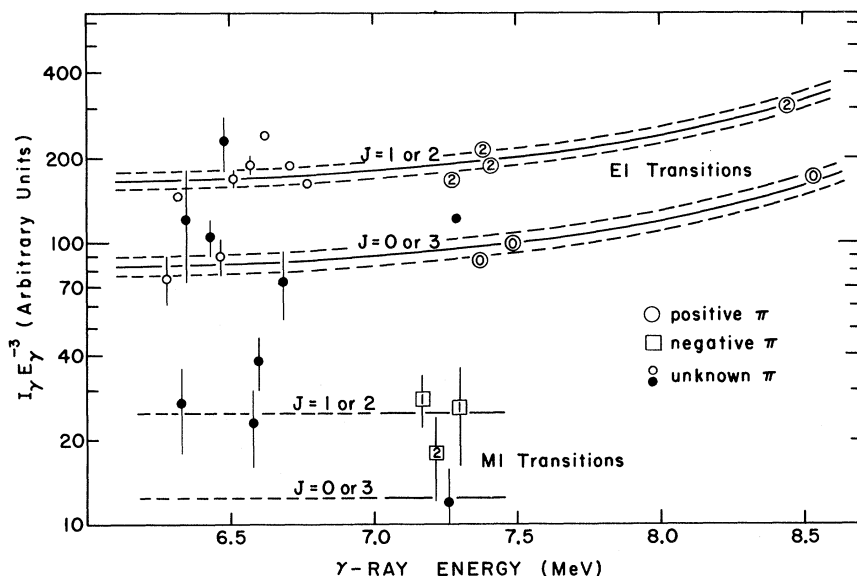


FIG. 23. Plot of  $I_\gamma E_\gamma^{-3}$  versus  $E_\gamma$  for  $^{155}\text{Gd}(n, \gamma)^{156}\text{Gd}$ . The spins given by numbers inside some points and the parities indicated by the shapes of the points are the assignments reported previously, as summarized in Table XI. The error bars are the rms experimental errors; when no error bar is given, it is smaller than the data point. The expected magnitudes of the Porter-Thomas fluctuations are shown by the dashed lines.

TABLE X. High-energy transitions in  $^{164}\text{Er}(\bar{n}, \gamma)^{165}\text{Er}$  and states of  $^{165}\text{Er}$ . The random errors in  $E_\gamma$  are the same as those given for  $E_x$ , and the absolute values of  $E_\gamma$  are uncertain by an additional 0.6 keV. Our values of  $E_x$  were normalized to the previous work at the state marked with an asterisk. The symbol  $n$  under "spin assignments" means  $J = \frac{1}{2}$  or  $\frac{3}{2}$ .

Line No.	This work		(Ref. a) $E_x$ (keV)	Relative intensity $I_\gamma E_\gamma^{-3}$	Spin and parity assignments		
	$E_\gamma$ (keV)	$E_x$ (keV)			Previous work (Ref. a)	This work	Composite
1	6649.9		0	<10	$\frac{5}{2}^-$		$\frac{5}{2}^-$
2	6602.7		47.2	<10	$\frac{5}{2}^+$		$\frac{5}{2}^+$
3	6572.7		77.3	<10	$\frac{7}{2}^-$		$\frac{7}{2}^-$
4	6407.2	*242.9 ± 0.3	242.9	149 ± 7	$\frac{3}{2}^-$	$n^-$	$\frac{3}{2}^-$
5	6352.5	297.6 ± 0.2	297.3	242 ± 10	$\frac{1}{2}^-$	$n^-$	$\frac{1}{2}^-$
6	6293.7	356.4 ± 0.2	356.5	245 ± 10	$\frac{3}{2}^-$	$n^-$	$\frac{3}{2}^-$
7	6143.7	506.4 ± 2.0	507.3	28 ± 10	$\frac{1}{2}^+$	$n^+$	$\frac{1}{2}^+$
8	6117.3	532.8 ± 1.5	534.5	34 ± 13	$\frac{3}{2}^+$	$n^+$	$\frac{3}{2}^+$
9	6059.9	590.2 ± 1.0	589.7	189 ± 15	$\frac{1}{2}^-$	$n^-$	$\frac{1}{2}^-$
			589.6		$\frac{3}{2}^+$		$\frac{3}{2}^+$
11	6041.6	608.5 ± 0.2	608.4	183 ± 9	$\frac{3}{2}^-$ or $\frac{5}{2}^-$	$n^-$	$\frac{3}{2}^-$
			745.7	<10	$\frac{1}{2}^+$	$>\frac{3}{2}$	$>\frac{3}{2}$
13	5796.8	853.3 ± 1.5	854.1	28 ± 6	$\frac{3}{2}^+$	$n^+$	$\frac{3}{2}^+$
14	5729.1	921.0 ± 0.3	920.5	145 ± 7	$\frac{1}{2}^-$	$n^-$	$\frac{1}{2}^-$
15	5687.6	962.5 ± 1.0	962.0	219 ± 20	$\frac{3}{2}^-$	$n^-$	$\frac{3}{2}^-$
			1032.1	<10	$\frac{3}{2}^+$	$>\frac{3}{2}$	$>\frac{3}{2}$
17	5605.1	1045.0 ± 0.3	1044.4	173 ± 9		$n^-$	$n^-$

<sup>a</sup>Adurazakov *et al.*, Ref. 32.

trum are given in the tables. Here we see that the lines in  $^{158}\text{Gd}$  are considerably stronger than those in  $^{156}\text{Gd}$ . This difference may be explained by the larger spacing of the initial states in  $^{158}\text{Gd}$ , which causes  $\Gamma_n/\Gamma$  (and hence  $\sigma_0$ ) to be considerably larger for the  $^{157}\text{Gd}$  resonances than for those in  $^{155}\text{Gd}$ .

The difference in the intensities of the  $^{156}\text{Gd}$  and  $^{158}\text{Gd}$  lines suggests that they can be separated on the basis of the observed  $\gamma$ -ray intensity. However, in practice this approach is not very useful because of various experimental uncertainties, but it does provide the information for the assignment of line 23 to  $^{158}\text{Gd}$  (Table XII).

In view of the complexity of the spectrum, a surprisingly large fraction of all the lines observed with energies greater than 6200 keV can be assigned to transitions in the individual isotopes  $^{156}\text{Gd}$  or  $^{158}\text{Gd}$ , as shown in Tables XI and XII. The few lines that cannot be assigned to one of these isotopes are listed in Table XIII. At  $\gamma$ -ray energies less than 6200 keV the spectrum becomes so complex (with four isotopes contributing lines) that

no effort was made to analyze all lines. Instead, the spectrum was used only to establish approximate intensities of the transitions in  $^{158}\text{Gd}$  previously reported by Groshev *et al.*<sup>33</sup> These  $^{158}\text{Gd}$  lines account for most of the strongest peaks observed down to an energy of 5600 keV, as may be seen in Fig. 22.

The excitation energies determined from our measurements are in excellent agreement with those reported previously. Thus the quoted experimental errors (a few hundred eV for well-resolved lines) appear to be reasonable. The listed  $\gamma$ -ray energies were obtained by reducing the observed energies by 1.1 keV because of the energy shift caused by neutron capture at epithermal energies.

The failure to detect transitions to the  $4^+$  states of  $^{156}\text{Gd}$  and  $^{158}\text{Gd}$  (especially to those at 288 and 262 keV, respectively) shows that  $E2$  transitions and also  $p$ -wave capture are too weak to have a significant influence on the spectra. Consequently, the only decay pattern that needs to be considered is the one at the top of Fig. 22, and the data points

TABLE XI. High-energy transitions in  $^{155}\text{Gd}(\bar{n}, \gamma)^{156}\text{Gd}$  and states in  $^{156}\text{Gd}$ . The random errors in  $E_\gamma$  are the same as those given for  $E_x$ , and the absolute values of  $E_\gamma$  are uncertain by an additional 0.8 keV. In columns 11 and 12, the symbol  $n$  means  $J=0, 1, 2$ , or 3.

Line No.	Present work		Excitation energies (keV)				Relative intensity $I_\gamma E_\gamma^{-3}$	Spin and parity assignments			
	$E_\gamma$ (keV)	$E_x$ (keV)	$(\bar{n}, \gamma)$ (Ref. a)	$\beta$ - $\gamma$ (Ref. b)	$(n, \gamma)$ (Refs. c, d)	$(d, p)$ (Ref. d)		Previous $(n, \gamma)$ (Ref. b)	This work (Refs. c, d)	Composite	
1	8535.0	0	0	0	0	0	176±6	0 <sup>+</sup>	0 <sup>+</sup>	0, 3 <sup>+</sup>	0 <sup>+</sup>
2	8446.3	88.7±0.3	88	89.0	89.0 <sup>e</sup>	89	306±10	2 <sup>+</sup>	2 <sup>+</sup>	1, 2 <sup>+</sup>	2 <sup>+</sup>
				288.2	288.2	288	<2	4 <sup>+</sup>	4 <sup>+</sup>		4 <sup>+</sup>
				1040.0			<4	0 <sup>+</sup>			
5	7485.8	1049.2±0.3	1048		1049.4	1048	99±4		0 <sup>+</sup>	0, 3 <sup>+</sup>	0 <sup>+</sup>
6	7406.3	1128.7±0.3	1128	(1133)	1129.3	1130	188±6	3, 2	2 <sup>+</sup>	1, 2 <sup>+</sup>	2 <sup>+</sup>
7	7381.2	1153.8±0.3	1154	1154.0	1154.0 <sup>e</sup>	1154	216±6	2 <sup>+</sup>	2 <sup>+</sup>	1, 2 <sup>+</sup>	2 <sup>+</sup>
8	7367.2	1167.8±0.3		1168.2	1168.1	1168	87±5	0, 1, 2 <sup>+</sup>	0 <sup>+</sup>	0, 3 <sup>+</sup>	0 <sup>+</sup>
9	7294.6	1240.4±1.5		1242.3	1242.6	1242	26±10	1 <sup>-</sup>	1 <sup>-</sup>	(1, 2) <sup>-</sup>	1 <sup>-</sup>
10	7287.6	1247.4±0.5 <sup>f</sup>	1248	1251	1248.1 <sup>e</sup>		123±9 <sup>f</sup>	3 <sup>+</sup>	3 <sup>+</sup> , 1 <sup>-</sup>	0, 3 <sup>+</sup>	3 <sup>+</sup>
11	7277.3	1257.7±0.3	1259		1268.0		168±8		2 <sup>+</sup>	1, 2 <sup>+</sup>	2 <sup>+</sup>
12	7259.2	1275.8±0.3	1275		1276.1	1277	12±4		3 <sup>-</sup> , 3 <sup>+</sup>	0, 3 <sup>-</sup>	3 <sup>-</sup>
13	7214.8	1320.2±1.0		1319.6	1319.7 <sup>e</sup>	1319	18±6	2 <sup>-</sup>	2 <sup>-</sup>	$n$ <sup>-</sup>	2 <sup>-</sup>
14	7168.5	1366.5±1.0		1366.3	1366.5	1366	28±6	1 <sup>-</sup>	1 <sup>-</sup>	1, 2 <sup>-</sup>	1 <sup>-</sup>
				1511	1510.6	1511	<9	4 <sup>+</sup>	4 <sup>+</sup>		4 <sup>+</sup>
					1538.8				3 <sup>-</sup>		3 <sup>-</sup>
19	6763.7	1771.3±	1772		1772 <sup>e</sup>		163±8			1, 2 <sup>+</sup>	1, 2 <sup>+</sup>
21	6706.9	1828.1±0.3	1828		1819 <sup>e</sup>	1827	189±8			1, 2 <sup>+</sup>	1, 2 <sup>+</sup>
22	6683.0	1852.0±1.0	1851			1852	73±20		3 <sup>-</sup>	0, 3 <sup>+</sup>	0, 3 <sup>+</sup>
25	6619.0	1916.0±0.6 <sup>f</sup>	1915	(1913)	1913 <sup>e</sup>		241±8 <sup>f</sup>			1, 2 <sup>+</sup>	1, 2 <sup>+</sup>
26	6600.3	1934.7±0.7		1937	1935		38±8	3 <sup>-</sup>		$n$ <sup>-</sup>	$n$ <sup>-</sup>
28	6580.8	1954.2±1.5			1954 <sup>e</sup>		23±7			$n$ <sup>-</sup>	$n$ <sup>-</sup>
29	6568.8	1966.2±0.3	1967	1965.7	1965	1966	189±13	1 <sup>+</sup>	2 <sup>+</sup>	1, 2 <sup>+</sup>	1, 2 <sup>+</sup>
32	6508.4	2026.6±0.3		2026.4	2026	2026	170±12	1 <sup>+</sup>	2 <sup>+</sup>	1, 2 <sup>+</sup>	1, 2 <sup>+</sup>
34	6482.0	2053.0±0.5		2053	2053 <sup>e</sup>		230±50			1, 2 <sup>+</sup>	1, 2 <sup>+</sup>
35	6463.5	2071.5±0.5		(2063)	2063 <sup>e</sup>		90±14			0, 3 <sup>+</sup>	0, 3 <sup>+</sup>
37	6430.3	2104.7±0.5		2104	2104 <sup>e</sup>	2100	105±15			0, 3 <sup>+</sup>	0, 3 <sup>+</sup>
				2180.7			<15	(1) <sup>+</sup>			
43	6348.4	2186.6±1.5		2186.6	2186 <sup>e</sup>		122±50	1 <sup>+</sup>	1 <sup>+</sup>	$n$ <sup>+</sup>	1 <sup>+</sup>
45	6331.5	2203.5±1.5		2203			27±9			$n$ <sup>-</sup>	$n$ <sup>-</sup>
46	6318.5	2216.5±0.3			2216 <sup>e</sup>		146±8			1, 2 <sup>+</sup>	1, 2 <sup>+</sup>
49	6278.9	2256.1±0.7			2252 <sup>e</sup>		75±15			0, 3 <sup>+</sup>	0, 3 <sup>+</sup>
52	6234.8	2300.2±0.5 <sup>f</sup>		(2302)	2299 <sup>e</sup>		367±18 <sup>f</sup>			$n$ <sup>+</sup>	$n$ <sup>+</sup>
54	6153.7	2381.3±1.0			2382 <sup>e</sup>		144±15			$n$ <sup>+</sup>	$n$ <sup>+</sup>
56	6089.1	2445.9±0.5 <sup>f</sup>			2443 <sup>e</sup>		440±60 <sup>f</sup>			$n$ <sup>+</sup>	$n$ <sup>+</sup>

<sup>a</sup>Spencer *et al.*, Ref. 34.

<sup>b</sup>Lederer *et al.*, Ref. 37.

<sup>c</sup>Bäcklin *et al.*, Ref. 35.

<sup>d</sup>Groshev *et al.*, Ref. 36.

<sup>e</sup>States fed by primary transitions (Groshev *et al.*, Ref. 33).

<sup>f</sup>Abnormal intensity suggests presence of unresolved states.

should fall along four lines in the way discussed for  $^{166}\text{Ho}$  and  $^{168}\text{Er}$  in Secs. IV A1 and IV B1.

The reduced intensity  $I_\gamma E_\gamma^{-3}$  is plotted versus  $E_\gamma$  in Fig. 23 for  $^{156}\text{Gd}$ . From this plot it is clear that the parity of a state can be determined easily and unambiguously from the measured intensity. However, an inspection of Fig. 23 shows that the points in the neighborhood of 6.5 MeV do not fall along straight lines drawn through the points associated with  $E1$  transitions to states of known

spin and positive parity. Thus, we need to establish some objective way of drawing curved lines through the data. The first step is to select the most reliable data by rejecting all lines that are not well resolved. Those remaining are the open circles (both small and large) in Fig. 23. Now these selected data points appear to fall into two clear-cut groups of intensities, as expected, and we may form a single curve by plotting  $I_\gamma E_\gamma^{-3} Q_J^{-1}$  versus  $E_\gamma$ , where the number  $Q_J$  of transition paths

TABLE XII. High-energy transitions in  $^{157}\text{Gd}(\bar{n}, \gamma)^{158}\text{Gd}$  and states in  $^{158}\text{Gd}$ . The random errors in  $E_\gamma$  are the same as those given for  $E_x$ , and the absolute values of  $E_\gamma$  are uncertain by an additional 0.8 keV. The symbol  $n$  in the last two columns means  $J=0, 1, 2$ , or  $3$ .

Line No.	Present work		Excitation energies (keV) from				Relative intensity $I_\gamma E_\gamma^{-3}$	Summary of spin and parity assignments				
	$E_\gamma$ (keV)	$E_x$ (keV)	other measurements (Ref. a)	other measurements (Ref. b)	$(n, \gamma)$ (Ref. c)	$(d, p)$		(Ref. a)	(Ref. b)	(Ref. c)	This work	Composite
3	7936.4	0	0	0	0	0	242±7	0 <sup>+</sup>	0 <sup>+</sup>	0 <sup>+</sup>	0, 3 <sup>+</sup>	0 <sup>+</sup>
4	7857.1	79.3±0.3	79.5	79.5	79 <sup>d</sup>	79	551±17	2 <sup>+</sup>	2 <sup>+</sup>	2 <sup>+</sup>	1, 2 <sup>+</sup>	2 <sup>+</sup>
			261.4	261.5	262	261	<2	4 <sup>+</sup>	4 <sup>+</sup>	4 <sup>+</sup>		4 <sup>+</sup>
15	6959.7	976.7±0.6	977.1	978	978 <sup>d</sup>	978	60±7	1 <sup>-</sup>	1 <sup>-</sup>	1 <sup>-</sup>	1, 2 <sup>-</sup>	1 <sup>-</sup>
16	6912.4	1024.0±0.6	1023.7	1025	1025 <sup>d</sup>	1025	51±6	2 <sup>-</sup>	(2) <sup>-</sup>	2 <sup>-</sup>	1, 2 <sup>-</sup>	2 <sup>-</sup>
17	6894.0	1042.4±1.0	1041.6	1043	1043	1044	35±7	3 <sup>-</sup>	3 <sup>-</sup>	3 <sup>-</sup>	$n^-$	3 <sup>-</sup>
20	6748.7	1187.7±0.4	1187.1	1185	1188 <sup>d</sup>	1188	403±20	2 <sup>+</sup>	2 <sup>+</sup>	2 <sup>+</sup>	1, 2 <sup>+</sup>	2 <sup>+</sup>
			1195.9					0 <sup>+</sup>				0 <sup>+</sup>
23	6675.5	1260.9±1.0	1259.9				318±50	2 <sup>+</sup>			(1, 2) <sup>+</sup>	2 <sup>+</sup>
24	6670.7	1265.7±1.5	1265.4	1268	1268 <sup>d</sup>	1268	255±40	3 <sup>+</sup>	3 <sup>+</sup>	3 <sup>+</sup>	(0, 3) <sup>+</sup>	3 <sup>+</sup>
31	6530.9	1405.1±0.4		1405	1405	1403	185±9		(3 <sup>-</sup> )		0, 3 <sup>+</sup>	0, 3 <sup>+</sup>
33	6486.2	1450.2±1.5	1451.6			1449	206±40	0 <sup>+</sup>			0, 3 <sup>+</sup>	0 <sup>+</sup>
38	6418.6	1517.8±0.4	1517.3	1521	1521 <sup>d</sup>	1518	366±11	2 <sup>+</sup>	(2 <sup>+</sup> )		1, 2 <sup>+</sup>	2 <sup>+</sup>
55	6145.8	1790.6±1.5	1792.4		1795 <sup>d</sup>	1795	427±40				$n^+$	$n^+$
57	6070.0	1865 ±4.0			1862 <sup>d</sup>	1856	~50				$n^-$	$n^-$
58	6042.1	1894.3±1.5	1894.5		1898 <sup>d</sup>		419±50				$n^+$	$n^+$
59	6006.5	1929.9±1.5	1930.7		1932 <sup>d</sup>	1924	482±60				$n^+$	$n^+$
60	5902.3	2034.1±1.5			2034 <sup>d</sup>	2030	521±80				$n^+$	$n^+$
61	5784.6	2151.8±1.5			2154 <sup>d</sup>	2154	308±50				$n^+$	$n^+$
62	5719.3	2217.1±2.0			2219 <sup>d</sup>		510±100				$n^+$	$n^+$
63	5655.9	2280.5±3.0			2280 <sup>d</sup>		580±150				$n^+$	$n^+$
64	5608.9	2327.5±3.0			2330 <sup>d</sup>		486±150				$n^+$	$n^+$

<sup>a</sup>Greenwood and Reich, Ref. 38.

<sup>b</sup>Lederer *et al.*, Ref. 37.

<sup>c</sup>Groshev *et al.*, Ref. 36.

<sup>d</sup>States fed by primary transitions (Groshev *et al.*, Ref. 33).

TABLE XIII. Transitions in the Gd spectrum that cannot be assigned with certainty to  $^{156}\text{Gd}$  or  $^{158}\text{Gd}$ .  $\gamma$ -ray intensities are in arbitrary units. The symbol  $n$  in the last column means  $J=0, 1, 2$ , or  $3$ .

Line No.	$E_\gamma$ (keV)	$I_\gamma E_\gamma^{-3}$	$A$	$J^\pi$
18	6820.1±0.6	60±6	(158)	1, 2 <sup>-</sup>
25	6619.0±2.0	>50	156 or 158	
27	6587.1±2.0	19±7	156 or 158	$n^-$
30	6546.4±1.0	58±6	(158)	1, 2 <sup>-</sup>
36	6452.7±1.5	60±15	(155)	$\frac{3}{2}^-$
39	6395.7±1.5	60±15	156 or 158	
40	6388.0±1.0	149±15	156 or 158	$n^+$
41	6373.2±3.0	50±15	156 or 158	
42	6359.6±0.3	543±25	(157)	$\frac{3}{2}^-$
44	6345.0±1.5	176±60	156 or 158	$n^+$
47	6303.9±1.5	78±15		
48	6295.8±2.0	28±10	156 or 158	$n^-$
50	6265.7±1.0	133±15	156 or 158	$n^+$
51	6242.5±3.0	36±15		
53	6212.4±0.5	215±11	156 or 158	$n^+$

is inferred from the observed intensity when it is not known from the spin. The result is given in Fig. 24, where the data for  $^{158}\text{Gd}$  are also included. Here one sees that, with the exception of the one high point at 6.62 MeV, all of the data points appear to fall along a smooth curve with a scatter that is consistent with the indicated uncertainties for the individual points. This qualitative impression is confirmed by a  $\chi^2$  test. When all points are used,  $\chi^2 = 34.3$ , an unacceptably large value for only about  $20 - 4 = 16$  degrees of freedom; but if the single high point is removed,  $\chi^2 = 14.7$ , almost exactly the expected value. Here again, as in the holmium and erbium data, the high point is almost surely caused by the summing of unresolved lines, and we proceed on this assumption.

The  $\chi^2$  test shows that the random errors in the intensities of the Gd lines are dominated by Porter-Thomas fluctuations and by errors in measurement. Also, it shows that our trial values of  $Q_\gamma$  for the data in Fig. 24 are all correct, since a change of any one of them would increase  $\chi^2$  by at

least 30. Thus the energy dependence given by the solid line in Fig. 24 may be transferred to Fig. 23 and used with confidence to infer the spins of states not involved in Fig. 24.

The arguments behind most of the conclusions stated in Tables XI and XII are self-evident from the data given in the tables. However, the following states in  $^{156}\text{Gd}$  deserve some comment.

*1040 keV.* The  $0^+$  state at 1040 keV accepted by Lederer, Hollander, and Perlman (LHP)<sup>37</sup> cannot exist (as a  $0^+$  state), in view of our failure to detect a line at about 7495 keV.

*1247.4 keV.* LHP<sup>37</sup> and Groshev *et al.*<sup>36</sup> give  $3^+$  and  $1^-$ , respectively, for this state. Our intensity is high enough to ensure that a positive-parity state is present, but the observed intensity is not consistent with the expected intensity for either set of possible  $J$  values. The observed intensity is in good agreement with the hypothesis that both a  $3^+$  and a  $1^-$  state are present at about the same energy, but the shape of the observed line does not give additional evidence for two states.

*1538.8 keV.* This state reported by Bäcklin *et al.*<sup>35</sup> is largely obscured in our data by the 7006-keV line in  $^{11}\text{B}$ .

*1916.0 keV.* As discussed in connection with Fig. 24, there are almost surely two transitions with  $E_\gamma \approx 6619$  keV, and one of them must be in  $^{156}\text{Gd}$ . The observed intensity would be explained by any one of three combinations:

- $1^+$  or  $2^+$  state in  $^{156}\text{Gd}$  and  $0^+$  or  $3^+$  in  $^{156}\text{Gd}$ ;
- $1^+$  or  $2^+$  in  $^{156}\text{Gd}$  and  $1^-$  or  $2^-$  in  $^{158}\text{Gd}$ ;
- $0^+$  or  $3^+$  in  $^{156}\text{Gd}$  and  $0^+$  or  $3^+$  in  $^{158}\text{Gd}$ .

*1954.2 keV.* Line 28 was assigned to  $^{156}\text{Gd}$  on the basis of the transition reported in Ref. 33. However, the errors are large enough that possibly

line 27 (Table XIII) should have been assigned to  $^{156}\text{Gd}$  instead. If so,  $E_x = 1960.5 \pm 2.0$  keV.

*2180.7 keV.* According to LHP,<sup>37</sup> this state has  $J^\pi = (1)^+$ . Our data show that it cannot have positive parity and  $J < 4$ .

*2186.6 keV.* Our spectrum contains two poorly resolved lines at an energy of about 6348 keV, namely, lines 43 and 44. Previous measurements<sup>33, 37</sup> showed that at least one of these is in  $^{156}\text{Gd}$ . Both lines are strong enough to be consistent with what is expected for a positive-parity state in  $^{156}\text{Gd}$ , but the data require only one of them to be assigned to  $^{156}\text{Gd}$ . The choice of line 43 for this assignment and the indicated spin assignment depend on the previous work.<sup>33, 37</sup>

*2300 keV.* There is a strong indication that summing is involved in the line associated with this state and for many states at higher excitation energy.

The basis for most of our conclusions about states in  $^{158}\text{Gd}$  is also evident from the data given in the tables. However, the following states require comment.

*1196 keV.* The presence of this positive-parity state reported by Greenwood and Reich<sup>38</sup> is obscured by the 6739-keV line in  $^{11}\text{B}$ .

*1116 and 1390 keV.* The observed intensities suggest that the 6820- and 6546-keV lines in Table XIII should be assigned to  $^{158}\text{Gd}$ . If so, the resulting states at  $1116.3 \pm 0.6$  and  $1390.0 \pm 1.0$  keV would both have  $J^\pi = 1^-$  or  $2^-$ .

*1317 keV.* As mentioned earlier, the anomalously intense 6619-keV line may be interpreted as evidence for an unresolved state at  $1317.4 \pm 1.5$  keV in  $^{158}\text{Gd}$ . If it exists, it would have  $J^\pi = 1^-, 2^-, 0^+$ , or  $3^+$ .

#### F. $^{154}\text{Gd}(n, \gamma)^{155}\text{Gd}$ and $^{156}\text{Gd}(n, \gamma)^{157}\text{Gd}$

The most we may expect to obtain for  $^{155}\text{Gd}$  and

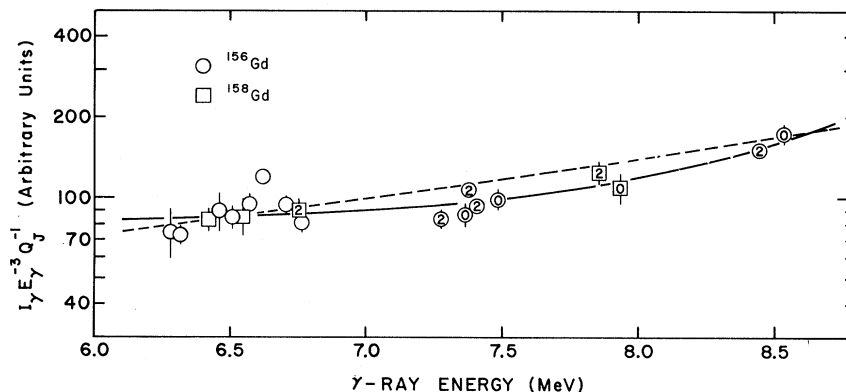


FIG. 24. The energy dependence of  $I_\gamma E_\gamma^{-3} Q_J^{-1}$  for  $^{155, 157}\text{Gd}(\bar{n}, \gamma)^{156, 158}\text{Gd}$ . The numbers within some of the points are the  $J$  values reported previously, as summarized in Tables XI and XII. The indicated errors include both Porter-Thomas fluctuations and errors of measurement. The dashed line was calculated from Eq. (16) with the parameters given in Ref. 20.

$^{157}\text{Gd}$  are reliable energies for the ground-state transition. The results are given in Table XIII.

The binding energies of  $^{154}\text{Gd}$  and  $^{156}\text{Gd}$  (see Table XVI) are known in advance with an accuracy of about  $\pm 10$  keV from the least-squares adjustment of Mattauch, Thiele, and Wapstra.<sup>39</sup> This requires that the ground-state transition in  $^{155}\text{Gd}$  (if detected) should be either line 35 or 36. We tentatively assign line 36 to  $^{155}\text{Gd}$  in order that line 35 ( $E_\gamma = 6463.5$  keV) may reasonably be associated with the 6467-keV line in  $^{156}\text{Gd}$  reported by Groshev *et al.*<sup>33</sup>; the energy of line 36 ( $E_\gamma = 6452.7$  keV) would seem to be too low to be consistent with the value 6467 keV.

In  $^{157}\text{Gd}$ , lines 42, 43, and 44 are all consistent with what is expected for the energy of the ground-state transition. However, line 43 is excluded because of its correspondence to what is expected for an accurately measured state in  $^{156}\text{Gd}$ . Line 42 is tentatively assigned to  $^{157}\text{Gd}$  on the basis of its intensity, which is about what is expected on the assumption that  $\langle \Gamma_{ij}/D \rangle$  is the same for all of the Gd isotopes (as seen in Table XVII). The other possibility, an assignment of line 44 to  $^{157}\text{Gd}$ , would require an anomalously weak  $\gamma$ -ray strength function for  $^{157}\text{Gd}$  relative to those for  $^{156}\text{Gd}$  and  $^{158}\text{Gd}$ .

The influence of the slight uncertainties in the identification of the ground-state transitions in  $^{155}\text{Gd}$  and  $^{157}\text{Gd}$  may be taken into account by increasing the experimental uncertainty enough to include all possible assignments. In this approach, the binding energy of  $^{154}\text{Gd}$  becomes  $6458 \pm 6$  keV, and that for  $^{156}\text{Gd}$  becomes  $6353 \pm 7$  keV.

#### G. $^{105}\text{Pd}(n, \gamma)^{106}\text{Pd}$

For all of the spectra discussed above, the only source of information about the quantum numbers of low-energy states is the intensity of the observed high-energy transitions. In this section we consider a nucleus for which the *shape* of the  $\gamma$ -ray line also gives useful spectroscopic information.

Average-resonance-capture spectra were measured for the three samples of natural palladium described in Table II. The spectrum for one of these was given in Fig. 5. Several features of the palladium spectra are noteworthy. First, the transition to the  $0^+$  ground state is easily observable, even though this state can be reached only by an  $E2$  transition or by  $p$ -wave capture followed by an  $E1$  transition. Second, there is no marked difference in the intensities of transitions to known negative-parity and positive-parity states. And finally, the lines associated with transitions to the known positive-parity states have prominent high-energy

tails, whereas the line associated with the  $3^-$  state at 2090 keV is much more symmetrical.

The  $\gamma$ -ray lines attributed to  $^{106}\text{Pd}$  and the corresponding final states are described in Table XIV. Capture in the even-even nuclides of the target also form a few lines in the energy range of interest, and these are identified in the ways outlined in Sec. IV H. As shown in Table XIV, most of the  $^{106}\text{Pd}$  states observed in our measurements have been detected in some previous measurement and especially in the  $(d, p)$  measurements of Dittmer and Daehnick.<sup>40</sup> Many of the states had not been reported previously<sup>41, 42</sup> as being observed from capture  $\gamma$  rays.

The remarkable degree to which the shape of the  $^{106}\text{Pd}$   $\gamma$ -ray lines depends on the parity of the final state is shown in Fig. 11. The cause for this dependence is the difference in the neutron-energy dependence of the cross sections for  $s$ -wave and  $p$ -wave neutron capture, as discussed in Sec. III D.

The line shapes of transitions to states of negative and positive parity are so different that the parity can be determined easily from the shape when the line is well resolved. However, at  $\gamma$ -ray energies below 7 MeV the density of lines is so great that the shape of the weaker lines cannot be determined with certainty. The spectrum for the thinner ( $0.23$  g/cm<sup>2</sup>) absorber gives the most information about the line shapes, because for it the average-resonance-capture line is somewhat narrower than it is for the thicker absorber. The parities obtained from the line shapes are given in column 10 of Table XIV.

The reduced intensities observed in the spectrum measured with the thicker ( $0.63$  g/cm<sup>2</sup>)  $^{10}\text{B}$  absorber are plotted in Fig. 25 as a function of  $E_\gamma$ . It is immediately obvious here that the observed intensity does not give such a clear-cut measure of the spin and parity as it does for the nuclides discussed in earlier sections. However, there is a very strong correlation between the  $\gamma$ -ray intensity and the parity determined from the shape. From this we conclude that, in spite of the small ratio of the intensities of  $E1$  and  $M1$  transitions in  $^{106}\text{Pd}$ , the intensity gives a reliable determination of the parity. With one exception (to be discussed later), the parities obtained from the intensities and the shapes are the same (as seen in Table XIV).

The use of  $\gamma$ -ray intensity to determine spin is more involved for  $^{106}\text{Pd}$  than for the nuclides treated earlier in this paper. First consider the  $E1$  transitions to negative-parity states. Here the intensities appear to separate into two groups for which the intensities differ by a factor of 2, as expected. The shape of the lines formed by these points is indeterminate because of the narrow en-

TABLE XIV. High-energy transitions in  $^{105}\text{Pd}(\bar{n}, \gamma)^{106}\text{Pd}$  and states of  $^{106}\text{Pd}$ . The random errors in  $E_\gamma$  are the same as those given for  $E_x$ , and the absolute values are uncertain by an additional 1.0 keV.  $\gamma$ -ray intensities are in arbitrary units. In columns 11 and 12, the symbol  $n$  means  $J=1, 2, 3$ , or 4 and  $m$  means  $J=0, 1, 4$ , or 5.

Line No.	This work		$E_x$ (keV) from other measurements			$I_\gamma E_\gamma^{-3}$ for absorber thickness (g/cm <sup>2</sup> <sup>10</sup> B)		Spin and parity assignments of final states			
	$E_\gamma$ (keV)	$E_x$ (keV)	$\beta$ - $\gamma$ (Ref. a)	$(n, \gamma)$ (Ref. b)	$(d, p)$ (Ref. c)	0.27	0.50	Previous work (Ref. c)	Parity from shape	$J^\pi$ from intensity	Composite
0	9562.4	-0.8±0.7	0	0	0	7±1	9±1	0 <sup>+</sup>	+	0, 5 <sup>+</sup>	0 <sup>+</sup>
1	9049.8	511.8±0.2	511.8	512	511	52±2	57±2	2 <sup>+</sup>	+	2, 3 <sup>+</sup>	2 <sup>+</sup>
2	8433.6	1128.0±0.2	1127.8	1125	1130	61±2	58±2	2 <sup>+</sup>	+	2, 3 <sup>+</sup>	2 <sup>+</sup>
3			1133.3			<15	<15	0 <sup>+</sup>		0, 5 <sup>+</sup>	0 <sup>+</sup>
4	8333.6	1228.0±0.3	1228.9	1226	1229	31±1	32±1	4 <sup>+</sup>	+	1, 4 <sup>+</sup>	4 <sup>+</sup>
5	8004.0	1557.6±1.0	1557.3	1556		35±5	32±7	(4, 3 <sup>+</sup> )	+	1, 4 <sup>+</sup>	(4) <sup>+</sup>
6	7999.2	1562.4±1.0	1562		1561	64±5	63±7	2 <sup>+</sup>	+	2, 3 <sup>+</sup>	2 <sup>+</sup>
7	7856.3	1705.3±2.0	1703			4±1	5±1	0, 1 <sup>+</sup>	+	0, 5 <sup>+</sup>	0 <sup>+</sup>
8	7651.2	1910.4±0.4			1910	34±2	34±5	2, 3 <sup>+</sup>	+	1, 4 <sup>+</sup>	1, 4 <sup>+</sup>
9	7629.0	1932.6±0.4	1932.0	1930	1936	40±2	36±3	3, 4 <sup>+</sup>	+	1, 4 <sup>+</sup>	4 <sup>+</sup>
10	7561.3	2000.3±2.0	2001			8±2		0 <sup>+</sup>	+	0, 5 <sup>+</sup>	0 <sup>+</sup>
12	7481.9	2079.7±1.0	2076.4			26±4	11±3	3, 4, 5 <sup>+</sup>		$m^+$	4, 5 <sup>+</sup>
13	7475.9	2085.7±0.3	2084	2083	2084	144±5	161±5	3 <sup>-</sup>	-	2, 3 <sup>-</sup>	3 <sup>-</sup>
14	7318.8	2242.8±0.5			2242	35±2	45±3	2 <sup>+</sup>	+	(2, 3) <sup>+</sup>	2 <sup>+</sup>
15	7278.6	2283.0±1.0			2282	25±3	28±4	(3, 4 <sup>+</sup> )	+	(1, 4) <sup>+</sup>	(4) <sup>+</sup>
16	7254.4	2307.2±0.6	2305.5			87±12	82±12	4 <sup>-</sup>	-	1, 4 <sup>-</sup>	4 <sup>-</sup>
17	7250.7	2310.9±2.0			2310	<35	(10)	2, 3 <sup>+</sup>		$m^+$	0-5 <sup>+</sup>
18	7210.4	2350.8±0.7	2350.3	2354	2353	25±3	21±3	3, 4 <sup>+</sup>	+	(1, 4) <sup>+</sup>	(4) <sup>+</sup>
19	7160.2	2401.4±0.2		2394	2398	160±4	149±7	3 <sup>-</sup> -8 <sup>-</sup>	-	2, 3 <sup>-</sup>	3 <sup>-</sup>
20	7123.2	2438.4±1.0	2440	2431	2441	29±3	49±5	(1, 2 <sup>+</sup> )	+	(2, 3) <sup>+</sup>	(2) <sup>+</sup>
21	7090	2472 ±2.0			2471	12±4	39±5	0-5 <sup>+</sup>		$n^+$	$n^+$
22	7076.2	2485.4±0.4		2484		68±4	66±7		-	1, 4 <sup>-</sup>	1, 4 <sup>-</sup>
23	7061.1	2500.5±0.2			2502	142±14	133±13		-	2, 3 <sup>-</sup>	2, 3 <sup>-</sup>
						(40)	(40)	2, 3 <sup>+</sup>			2, 3 <sup>+</sup>
24	6982.2	2579.4±0.3		2578		110±4	78±20		-	1, 4 <sup>-</sup>	1, 4 <sup>-</sup>
					2579			0-5 <sup>+</sup>			0-5 <sup>+</sup>
25	6971.1	2590.5±1.0			2592	33±3	19±6	2, 3 <sup>+</sup>	+	$n^+$	2, 3 <sup>+</sup>
26	6933.4	2628.2±1.0	2630		2627	27±3	33±5	1, 2 <sup>+</sup>	+	(2, 3) <sup>+</sup>	(2) <sup>+</sup>
27	6914.0	2647.6±2.0			2648	10±3	14±4	0 <sup>+</sup> -5 <sup>+</sup>		(1, 4) <sup>+</sup>	(1, 4) <sup>+</sup>
28	6899.1	(2662.5±2.0)				16±4				$m^+$	$m^+$
29	6856.5	(2705.1±3.0)				17±5				$m^+$	$m^+$
30	6848.0	2713.6±1.0			2714	36±4	37±7	2 <sup>+</sup>	+	(2, 3) <sup>+</sup>	2 <sup>+</sup>
					2736	<20		0-5 <sup>+</sup>		0-5 <sup>+</sup>	0-5 <sup>+</sup>
31	6812.9	2748.7±2.0		2744 <sup>d</sup>		>30		$n^-$	(-)		$n^-$
			2756.4		2757	<15		5 <sup>+</sup>		0-5 <sup>+</sup>	5 <sup>+</sup>
32	6785.6	2776.0±1.0			2776	63±7	78±7	2, 3 <sup>+</sup>	+		(2, 3 <sup>+</sup> )
33	6777.1	(2784.5±2.0)				(36±7)	(35±6)			$n^+$	$n^+$
					2791	<15	<20				
					2814			2, (3) <sup>+</sup>			2, (3 <sup>+</sup> )
			2827			<50		(1, 2 <sup>+</sup> )		0-5 <sup>+</sup>	(1, 2 <sup>+</sup> )
35	6713.5	2848.1±1.5			2852	51±7	22±8	2, 3 <sup>+</sup>	+	$n^+$	2, 3 <sup>+</sup>
36	6700.6	2861.0±1.0		2855 <sup>d</sup>		69±5	24±8			$n^+$	$n^+$
37	6683.6	2878.0±3.0	2880		2879	12±5	(4)	0-5 <sup>+</sup>		$m^+$	$m^+$
38	6675.5	2886.1±0.5				135±7	90±9		-	$n^-$	$n^-$
39	6662.8	2898.8±0.7		2898		108±9	56±15			(1, 4 <sup>-</sup> )	(1, 4 <sup>-</sup> )
					2903	<30	(29)	2, 3 <sup>+</sup>		(1, 4) <sup>+</sup>	$n^+$
40	6653.1	2908.5±0.7				136±7	95±15		(-)	1, 4 <sup>-</sup>	1, 4 <sup>-</sup>
41	6645.4	2916.2±2.0			2918	30±6	29±10	2 <sup>+</sup>	(+)	$n^+$	2 <sup>+</sup>
42	6625.4	2936.2±0.4		2924		160±8	146±15		-	2, 3 <sup>-</sup>	2, 3 <sup>-</sup>
			2951.3		2955	<10		5 <sup>+</sup>			5 <sup>+</sup>
43	6589.8	2971.7±0.5		2968		152±6	135±20		-	(2, 3) <sup>-</sup>	(2, 3) <sup>-</sup>
44	6584.2	2977.4±2.0			2975	47±15	28±10	0-6 <sup>+</sup>		$n^+$	$n^+$
					3026			0-5 <sup>+</sup>			0-5 <sup>+</sup>
46	6518.9	3042.7±1.5			3044	47±5	46±15	(1, 2 <sup>+</sup> )			(1, 2 <sup>+</sup> )
47	6505.2	3056.4±2.0			3055	53±8	53±15	2 <sup>+</sup>			2 <sup>+</sup>
48	6489.8	3071.8±0.5		3064	(3069)	204±10	155±10		-	2, 3 <sup>-</sup>	2, 3 <sup>-</sup>

<sup>a</sup>Lederer *et al.*, Ref. 37.<sup>b</sup>Bartholomew *et al.*, Ref. 41.<sup>c</sup>Dittmer and Daenick, Ref. 40.<sup>d</sup>Coceva *et al.*, Ref. 42.

ergy range involved, but the data are at least consistent with the giant-resonance model.

The energy dependence of the  $\gamma$ -ray strength function appears to be more complex for the  $M1$  radiation. First note that  $E2$  transitions and  $p$ -wave capture cannot be ignored, as shown by the fact that the lines associated with the  $0^+$  states at 0 and 1705 keV are easily detected. These intensities and those for other positive-parity states, when interpreted in terms of the decay patterns in Fig. 9 may be used to show that the transitions to  $2^+$  and  $3^+$  states should be about 1.8 times as strong as those to  $1^+$  and  $4^+$  states, rather than 2.0 times as strong.

In order to draw a curve through the positive-parity points, we proceed (as for other nuclides) by first selecting the lines that are well resolved and free from known uncertainties in interpretation. In Fig. 26 these data are plotted as  $I_\gamma E_\gamma^{-3} Q_J^{-1}$  versus  $E_\gamma$ , where  $Q_J = 1$  or  $1.8$  is inferred from  $J$  or from the observed intensity. With the exception of two points (to be discussed later in this subsection) the data form a smooth line that is consistent with the conclusions of Dittmer and Daehnick<sup>40</sup> about the spins of the final states. This curve is used in Fig. 25 to define the expected intensity for positive-parity states.

The two points in Fig. 26 that are widely scattered from the intensity curve for positive-parity states raise a question about the reliability of the curve. However, this element of doubt is largely removed by the fact that each of the anomalous points can be explained away, as follows.

1910.4 keV. Dittmer and Daehnick<sup>40</sup> conclude that

$J^\pi = 2^+$  or  $3^+$  for this state because an  $l=0$  component appears to be present in their  $(d, p)$  angular distribution. However, we feel that this assignment is inconclusive because of the poor quality of the angular distribution for this particular line. Thus, we judge that the intensity of our  $(\bar{n}, \gamma)$  line gives a more reliable indication of the spin, and we assign  $J^\pi = 1^+$  or  $4^+$  to this state.

2776.0 keV. Dittmer and Daehnick<sup>40</sup> give  $J^\pi = 2^+$  or  $3^+$  for a state at 2776 keV, whereas the line in our spectrum corresponding to this excitation energy is twice as strong as it should be for this  $J^\pi$  assignment. Since the  $\gamma$ -ray line has the appropriate shape for a positive-parity state, the simplest and not unlikely explanation of the discrepancy is that there are two states with  $J^\pi = 2^+$  or  $3^+$  at about 2776 keV.

Now we are ready to return to the main body of the <sup>106</sup>Pd data. In treating these data we were struck by the excellent agreement between the results obtained from the  $(\bar{n}, \gamma)$  data and the charged-particle measurements of Dittmer and Daehnick<sup>40</sup> for many states. Thus, when there is a discrepancy between the two kinds of data and when both kinds appear to be reliable, we have chosen to accept *both* results as valid. For example, the large  $(\bar{n}, \gamma)$  intensity of the state at 2500.5 keV indicates that it has negative parity, whereas the  $(d, p)$  angular distribution of a state at 2502 keV indicates that it has  $J^\pi = 2^+$  or  $3^+$ . We accept both statements as valid and proceed to obtain a corrected intensity for the negative-parity state under the assumption that the intensity for the unresolved positive-parity state may be read from the appropriate curve

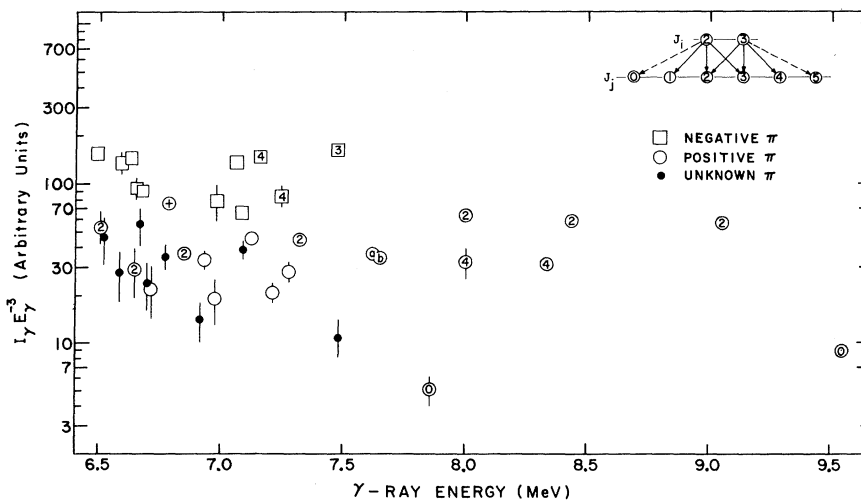


FIG. 25. Plot of  $I_\gamma E_\gamma^{-3}$  versus  $E_\gamma$ , for the reaction  $^{105}\text{Pd}(\bar{n}, \gamma)^{106}\text{Pd}$ . The parities were obtained from the  $\gamma$ -ray line shapes. The numbers within some of the points are the  $J$  values and the notation  $a$  and  $b$  means  $J=1$  or  $4$  and  $J=2$  or  $3$ , respectively, as given by the previous work summarized in Table XIV. The error bars are the rms experimental errors; when no error bar is given it is smaller than the data point.

in Fig. 26. The intensities in parentheses in Table XIV are assumed values of this kind. The scatter of the points in Fig. 26 was lessened considerably by this correction procedure.

Most of the arguments that led to the final spin and parity assignments given in Table XIV are easily understood from the data given in the table. However, several of the states require special comment.

*2055 keV.* A 7507-keV transition previously attributed<sup>43</sup> to a 2055-keV state in <sup>106</sup>Pd is now assigned to <sup>103</sup>Pd.

*2079.7 keV.* The weak transition to this state is too poorly resolved to allow its intensity to be determined well. Thus, the discrepancy between the values for the two absorbers is not very disturbing.

*2310.9 keV.* Reference 40 lists a state at 2310 keV with the tentative assignment  $J^\pi = 2^+ \text{ or } 3^+$ . In our spectra, the transition to this state is largely obscured by a strong transition to the nearby 2307.2-keV state. Nevertheless, the shape of the

composite  $\gamma$ -ray line appears to be inconsistent with what would be required if the state at 2310 keV had  $J^\pi = 2^+ \text{ or } 3^+$ . Our data are consistent with the possibilities  $J^\pi = 0, 1, 4, \text{ or } 5^+$ . In view of the element of doubt in the  $(d, p)$  assignment, we choose to reject it.

*2662.5 and 2705.1 keV.* These states, whose existence is based on the observation of weak lines at 6900 and 6858 keV, are uncertain because of the possibility that they result from neutron capture in <sup>102</sup>Pd.

*2784.5 keV.* The existence of this state is in some doubt because the  $\gamma$ -ray line involved can also be interpreted as a transition to a  $\frac{5}{2}^+$  state at 319 keV in <sup>105</sup>Pd.

#### H. <sup>102</sup>Pd( $n, \gamma$ )<sup>103</sup>Pd and <sup>104</sup>Pd( $n, \gamma$ )<sup>105</sup>Pd

The lines in the palladium spectrum that cannot be assigned to <sup>106</sup>Pd are listed in Table XV. Most of these can be assigned to <sup>103</sup>Pd or <sup>105</sup>Pd. The assignment of the 7507-keV line to <sup>103</sup>Pd depends on

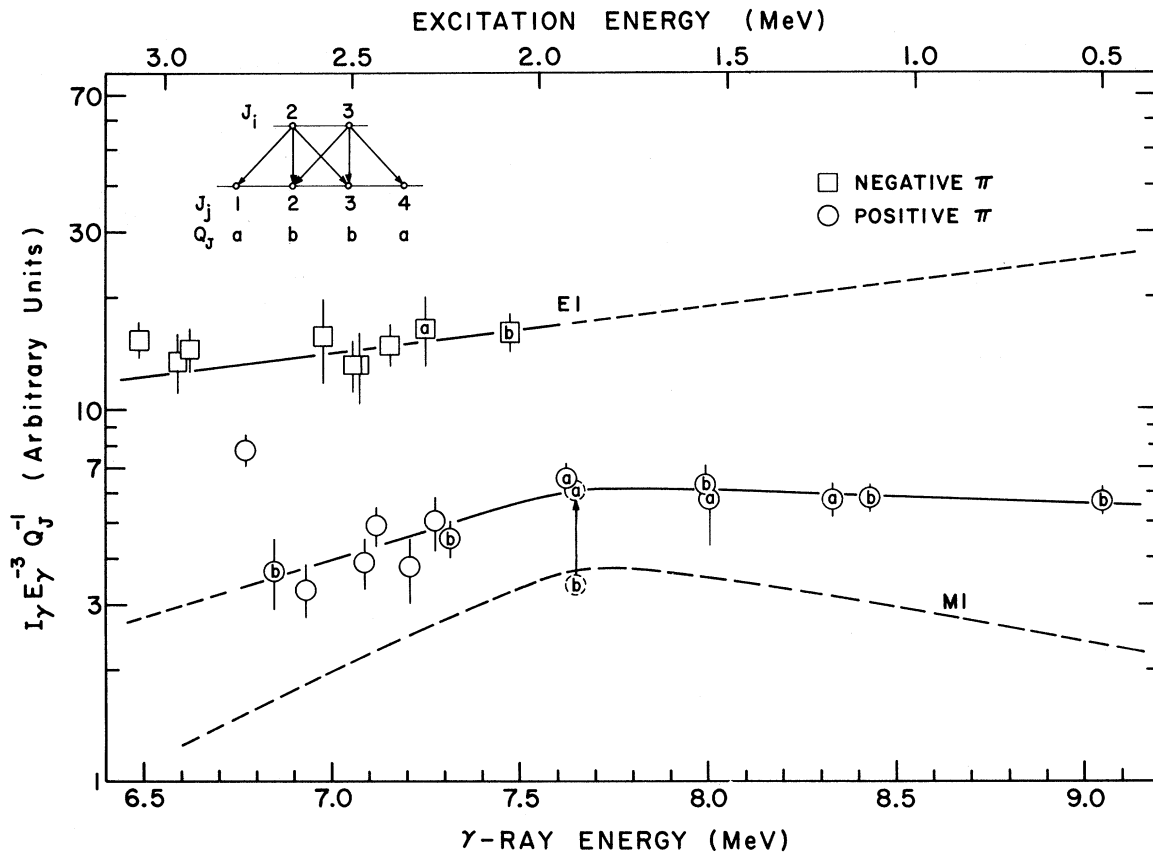


FIG. 26. Energy dependence of  $I_\gamma E_\gamma^{-3} Q_J^{-1}$  for <sup>105</sup>Pd( $\bar{n}, \gamma$ )<sup>106</sup>Pd in sample 10 of Table II. The letters  $a$  and  $b$  refer to  $J=1$  or  $4$  and  $J=2$  or  $3$ , respectively, as reported by Dittmer and Daehnick (Ref. 40). The indicated errors include both Porter-Thomas fluctuations and errors of measurement; when no error bar is given, the error is smaller than the data point. The line drawn through the E1 data points was calculated from Eq. (16) with the parameters given in Ref. 20 for rhodium. The dashed curve labeled M1 is a plot of  $\Gamma_{M1}/E_\gamma^3$ .

TABLE XV. High-energy transitions in  $^{102}\text{Pd}(\bar{n}, \gamma)^{103}\text{Pd}$  and  $^{104}\text{Pd}(\bar{n}, \gamma)^{105}\text{Pd}$ . The random errors in  $E_\gamma$  are the same as those given for  $E_x$ , and the absolute values are uncertain by an additional 0.7 keV.  $\gamma$ -ray intensities are in arbitrary units.

Line No.	$E_\gamma$ (keV)	Emitting nucleus	This work		Previous work		
			$E_x$ (keV)	$I_\gamma E_\gamma^{-3}$	$E_x$ (keV)	$J^\pi$	Ref.
11	7506.3	103	*118 $\pm$ 0.7	19 $\pm$ 4	118	( $\frac{3}{2}^+$ )	a
	7360.9	103	(263 $\pm$ 2.0)	5 $\pm$ 2	266		a
31	6812.9	105	280.9 $\pm$ 0.7	>50	280.4	$\frac{3}{2}^+$	b
34	6749.4	105	*344.4 $\pm$ 0.3	102 $\pm$ 10	344.4	$\frac{1}{2}^+$	b
45	6534.0	105	558.8 $\pm$ 0.3	186 $\pm$ 15	(560.7)	( $\frac{3}{2}^+$ )	b

<sup>a</sup>Bakru *et al.*, Ref. 44.

<sup>b</sup>Lederer *et al.*, Ref. 37.

both its energy and intensity. On the assumption that it is a transition to the 118-keV state,<sup>44</sup> the neutron separation energy of  $^{103}\text{Pd}$  is found to be consistent with previous data<sup>41</sup> and no other line in the spectrum would be consistent. Also, the intensity of the line is inconsistent with what is expected for a state of any spin and parity in  $^{106}\text{Pd}$ , the only other possibility permitted by the  $\gamma$ -ray energy. The assignment to  $^{103}\text{Pd}$  is supported by the presence of another weak line that may be associated with the 266-keV state in  $^{103}\text{Pd}$ .

The presence of the small  $^{102}\text{Pd}$  contaminant in the sample causes uncertainty in the interpretation of some of the lines at energies below 7.5 MeV, since an  $E1$  transition to states with  $J^\pi = \frac{1}{2}^-$  or  $\frac{3}{2}^-$  in  $^{103}\text{Pd}$  would be expected to have roughly the same intensity as the transitions to positive-parity states in  $^{106}\text{Pd}$ . In a well-resolved spectrum, the two kinds of transitions would be distinguishable since the  $^{103}\text{Pd}$  line would have the shape of a negative-parity state but the intensity of a positive-parity

state in  $^{106}\text{Pd}$ . However, in practice the shape is not always observable, so that there is a slight uncertainty about the isotopic assignment of some of the lines attributed in Table XIV to positive-parity states in  $^{106}\text{Pd}$ . On the other hand, except for those listed in parentheses, all of these positive-parity states were observed in at least one other kind of measurement.

The lines in  $^{105}\text{Pd}$  were identified by their pattern of energies<sup>37</sup> in relation to the known states of  $^{105}\text{Pd}$  and from the known binding energy.<sup>41</sup> The assignments are confirmed by the shapes of the  $\gamma$ -ray lines, which have the prominent tails characteristic of positive-parity states and at the same time a much greater intensity than such lines in  $^{106}\text{Pd}$ . Because the shape of a  $^{105}\text{Pd}$  line is easily recognized, it is certain that all states in  $^{105}\text{Pd}$  with  $J^\pi = \frac{1}{2}^+$  or  $\frac{3}{2}^+$  and with  $E_x < 560$  keV have been detected.

The presence of  $\frac{5}{2}^+$  states in  $^{105}\text{Pd}$  causes some uncertainty in the interpretation of two lines in the

TABLE XVI. Summary of binding energies.

Target nuclide	This work	(Ref. a)	Mass (Ref. b)	( $d, p$ ) (Ref. b)	Previous ( $n, \gamma$ )
$^{102}\text{Pd}$	7624.6 $\pm$ 1.5	7608 $\pm$ 23	7618 $\pm$ 34		
$^{104}\text{Pd}$	7094.1 $\pm$ 0.7	7091 $\pm$ 12	7065 $\pm$ 16	7092 $\pm$ 20	
$^{105}\text{Pd}$	9562.8 $\pm$ 1.1	9548 $\pm$ 12	9546 $\pm$ 13	9574 $\pm$ 30	9544 $\pm$ 4 <sup>b</sup>
$^{154}\text{Gd}$	(6452.9 $\pm$ 1.6)	6456 $\pm$ 9	6420 $\pm$ 40		
	6458 $\pm$ 6				
$^{155}\text{Gd}$	8535.4 $\pm$ 0.8	8527 $\pm$ 5	8510 $\pm$ 40		8530 $\pm$ 4 <sup>b</sup>
$^{156}\text{Gd}$	(6359.8 $\pm$ 0.6)	6347 $\pm$ 5	6360 $\pm$ 40		
	6353 $\pm$ 7				
$^{157}\text{Gd}$	7936.8 $\pm$ 0.8	7929.4 $\pm$ 3.7	7930 $\pm$ 40	7931 $\pm$ 5	7935 $\pm$ 4 <sup>b</sup>
$^{164}\text{Er}$	6650.1 $\pm$ 0.7	6645 $\pm$ 40			
$^{166}\text{Er}$	6436.0 $\pm$ 0.6	6438 $\pm$ 10	6467 $\pm$ 22	6434 $\pm$ 10	6436.15 $\pm$ 0.48 <sup>c</sup>
$^{167}\text{Er}$	7770.9 $\pm$ 0.6	7770 $\pm$ 21	7770 $\pm$ 40	7763 $\pm$ 3	7771.4 $\pm$ 0.5 <sup>d</sup>
$^{168}\text{Er}$	6002.7 $\pm$ 0.8	5997 $\pm$ 12	5970 $\pm$ 200	5998 $\pm$ 12	
$^{165}\text{Ho}$	6242.7 $\pm$ 0.6	6331 $\pm$ 33	6110 $\pm$ 200	6250 $\pm$ 7	6243 $\pm$ 3 <sup>b</sup>

<sup>a</sup>Mattauch *et al.*, Ref. 39.

<sup>b</sup>See Refs. 36 and 41.

<sup>c</sup>Michaelis *et al.*, Ref. 27.

<sup>d</sup>Michaelis *et al.*, Ref. 29.

spectrum. One of these is a weak line at about 7090 keV, which is approximately the energy expected for a transition to the  $\frac{5}{2}^+$  ground state of  $^{105}\text{Pd}$ . However, a careful examination shows that this interpretation would place the excitation energy of the state at  $-6$  keV (relative to the  $\frac{3}{2}^+$  state at 280 keV), and this value is thought to differ enough from zero to rule out the possibility that the line is formed mainly by the ground-state transition. Thus, the line is assigned to  $^{106}\text{Pd}$ . Similarly, the probable presence<sup>37</sup> of a  $\frac{5}{2}^+$  state at 319 keV in  $^{105}\text{Pd}$  raises the possibility that the 6777-keV line could be attributed either to  $^{105}\text{Pd}$  or  $^{106}\text{Pd}$ .

### I. Neutron Binding Energies

The neutron binding energies  $B_n$  measured in this investigation are summarized in Table XVI. The values of  $B_n$  were calculated from the relation  $B_n = E_x + E_\gamma + 0.537 \times 10^{-6} E_\gamma^2 / A$ , where the last term is the correction for recoil-energy loss, and all energies are in keV. Here it is assumed that  $E_\gamma$  has been corrected for the influence of nonzero neutron energies.

As mentioned in Sec. II, the spectrometer was calibrated by measuring the nitrogen capture  $\gamma$ -ray spectrum either immediately before or immediately after each sample run. The known errors in the binding energies determined from these measurements result from uncertainties in (a) the energies of the nitrogen lines used for calibration, (b) possible drifts in the characteristics of the detector system during a cycle of measurements, (c) the calculation of the amount by which  $\gamma$ -ray energies are shifted by the capture of neutrons with nonzero energy, (d) the determination of the centroids of the  $\gamma$ -ray lines, and (e) the energies of the final states of the transitions used to determine  $B_n$ . Tests with a pulse generator and the internal consistency of the data indicate that the differential nonlinearity of the detector system is not a significant source of error.

Typically, the energy shift, the centroid position, and the energy of the final state are accurately known (within about 0.1 keV), so that the uncertainties in  $B_n$  result mainly from a possible drift in the detector system and from the errors in the energies of the reference lines. The drift in the detector is expected to be small because the system is stabilized continuously on the output of a precision pulser. However, the counting rates during the sample and calibration runs are quite different, and it seems possible that this could cause some shift in the energy scale for the two kinds of runs. The internal consistency of the results for a given nuclide measured under different

experimental conditions indicates that the error caused by counting-rate differences (if present at all) is less than 0.3 keV.

The measured energy of the ubiquitous  $^{10}\text{B}(n, \gamma)\text{-}^{11}\text{B}$  line at about 7007 keV gives some additional information about the consistency and reliability of the energy calibration. In a set of 14 measurements, the mean value of the line is 7006.5 keV and the rms scatter is  $\pm 0.35$  keV; all values lie within 0.6 keV of the mean. Since the boron lines were measured under a variety of conditions, this result suggests that drifts in the calibration and errors in the determination of the centroids cause an uncertainty of about 0.35 keV in the energy of a line determined from a single measurement.

The energies of the nitrogen lines are known (Greenwood<sup>13</sup>) within an error that ranges from 0.35 keV for 5.5-MeV lines to 0.9 keV for the 9.1-MeV line. Thus, the uncertainties in the calibration standard cause the largest uncertainty in most of our determinations of binding energies.

The errors listed in Table XVI were calculated as the square root of the sum of the squares of the various kinds of uncertainties listed above. The systematic uncertainty in  $E_\gamma$  mentioned in the captions of many of the tables is a similar quantity, but the errors associated with the energy of the final state and with the determination of the centroid position are not included in it. In Table XVI, most of our values of binding energies are seen to be in satisfactory agreement with the previously reported results.

### V. SUMMARY OF RESULTS RELATED TO REACTION MECHANISMS

The main purpose of this investigation was to examine the usefulness of the average-resonance-capture method for nuclear spectroscopy. However, the data obtained also provide insight into the mechanisms of the capture process. In this section we briefly summarize the results of this kind that are closely related to the use of the  $(\bar{n}, \gamma)$  data in nuclear spectroscopy.

#### A. Energy Dependence of $E1$ Transitions

As was discussed in Sec. III A, the energy dependence of the average intensity of high-energy  $E1$  transitions in neutron-capture  $\gamma$  spectra may be inferred from the characteristics of the giant-dipole resonance observed in the photonuclear reaction. This approach involves two assumptions. Most basic is the assumption that each excited state  $E_x$  has built on it a giant resonance whose cross section  $\sigma_x$  at an excitation energy  $E$  is related to the cross section  $\sigma_0$  of the ground state by the relation  $\sigma_x(E) = \sigma_0(E - E_x)$ . Rosenzweig<sup>19</sup> has

justified this assumption in terms of a hydrodynamic model. If valid, this assumption implies that the  $\gamma$ -ray strength function depends only on the  $\gamma$ -ray energy, independent of the energy of the final state. A second, less fundamental assumption is that the photonuclear cross section is describable by a Lorentzian shape even at the very low energies involved in the capture  $\gamma$  radiation. If so, the  $\gamma$ -ray strength function is given by Eq. (16).

The relationship of our data to Eq. (16) has been given in Figs. 9, 13, 17, and 21. These comparisons show that the data for  $^{166}\text{Ho}$ ,  $^{168}\text{Er}$ , and  $^{106}\text{Pd}$  are at least consistent with Eq. (16); i.e., for each nuclide the radiation width seems to increase with  $E_\gamma$  more rapidly than  $E_\gamma^3$ , as expected, but the energy range covered by the data is too small to allow a good comparison between theory and experiment.

The data for the gadolinium isotopes cover a wide enough energy range to provide a rather good determination of the energy dependence of  $\Gamma_{E1}$ . As seen in Fig. 24, the total change in  $\Gamma_{E1}$  over the range 6.3–8.5 MeV is in good agreement with the change expected from the giant-resonance model, but there is some discrepancy at intermediate energies. This effect may be related to the kind of structure observed by Axel *et al.*<sup>45</sup> in the  $\gamma$ -ray strength function of  $^{92}\text{Zr}$  and  $^{210}\text{Bi}$ .

Although there are some discrepancies, the radiation widths in  $^{156}\text{Gd}$  are at least in qualitative agreement with what is expected from the giant-resonance model. Perhaps the most significant aspect of this result is that it supports the hypothesis that the giant resonance associated with each excited state is shifted in energy by an amount equal to the energy of the state, since in our experiment (in which only the energy of the final

state varies) the intensity would vary as  $E_\gamma^3$  if there were no shift.

For some purposes it is desirable to express Eq. (16) in terms of a mathematically-simple approximation. Axel<sup>18</sup> has pointed out that such a form is  $\langle \Gamma_{ij}/D_i \rangle = cE_\gamma^\alpha$ , where  $\alpha \approx 5$  for most nuclides when  $E_\gamma$  is in the neighborhood of 7 or 8 MeV. An even better approximation to Eq. (16) is  $\langle \Gamma_{ij}/D_i \rangle = cE_\gamma^3 e^{\beta E}$ , as is shown (for example) by the straightness of the dashed line in Fig. 24. The total variation in the radiation widths of  $^{156}\text{Gd}$  over the energy range 6.5–8.5 MeV corresponds to the values  $\alpha = 5.5 \pm 0.5$  and  $\beta = 0.34 \pm 0.06$ , where the errors include a generous allowance for the influence of possible errors in the efficiency calibration of the  $\gamma$ -ray detector. Clearly, these values of  $\alpha$  and  $\beta$  cannot conceivably be considered to be consistent with the values  $\alpha = 3$  and  $\beta = 0$  expected from the single-particle model.<sup>46</sup>

#### B. Relative Widths of $E1$ Transitions in Various Nuclei

As we have seen (Sec. V A), the hydrodynamic model of high-energy  $E1$  transitions predicts that the  $\gamma$ -ray strength function is a smooth function of  $\gamma$ -ray energy, and the data presented in this paper seem to be remarkably consistent with this expectation. Another implication of the model is that the absolute value of  $\langle \Gamma_{ij}/D \rangle$  should not differ much for neighboring nuclides, since they are expected to have roughly the same parameters for the  $E1$  giant resonance. Although our measurements were not made with this objective in mind, we can obtain some information on this subject by comparing the measured  $\gamma$ -ray intensities for the several isotopes in a given target.

TABLE XVII. Comparison of average values of reduced widths  $\langle \Gamma_{ij} D_i^{-1} E_\gamma^{-5} \rangle$  for various isotopes in a given sample. The  $\gamma$ -ray intensities, neutron-capture rates, and reduced widths are all in arbitrary units. The numbers in parentheses give the factors by which the capture rates and reduced widths are uncertain.

Sample No.	Emitting nucleus	$I_\gamma E_\gamma^{-3} Q_J^{-1}$	Neutron capture rate	$\langle \Gamma_{ij} D_i^{-1} E_\gamma^{-5} \rangle$	$\bar{E}_\gamma$ (keV)
8	$^{155}\text{Gd}$	$60 \pm 25$	144(2.0)	70(2.1)	6453
	$^{156}\text{Gd}$	$84 \pm 4$	145(1.15)	100(1.15)	6400
	$^{157}\text{Gd}$	$543 \pm 150$	537(1.40)	176(1.5)	6360
	$^{158}\text{Gd}$	$182 \pm 9$	264(1.15)	119(1.15)	6400
7	$^{165}\text{Er}$	$2060 \pm 200$	264(1.25)	76(1.30)	6250
	$^{167}\text{Er}$	$883 \pm 175$	156(1.25)	64(1.35)	5800
	$^{168}\text{Er}$	$188 \pm 20$	19(1.25)	100(1.30)	6110
	$^{169}\text{Er}$	$392 \pm 200$	72(1.25)	57(1.60)	6003
6	$^{165}\text{Er}$	$45 \pm 10$	63(1.20)	125(1.30)	6300
	$^{167}\text{Er}$	$500 \pm 70$	713(1.20)	145(1.25)	5800
	$^{168}\text{Er}$	$133 \pm 7$	258(1.15)	100(1.17)	6000
	$^{169}\text{Er}$	$403 \pm 130$	652(1.20)	120(1.35)	6003

The results of the comparison of  $\langle \Gamma_{ij}/D \rangle$  are given in Table XVII. Here the experimental values of  $I_\gamma E_\gamma^{-3} Q_J^{-1}$  are averaged over the  $E1$  transitions in the neighborhood of the indicated  $\gamma$ -ray energy. The neutron-capture rates were calculated from the integral in Eq. (11), and the indicated uncertainties in these rates include the influence of uncertainties in the nuclear parameters and in the accuracy of the equation.

The relative values of  $\langle \Gamma_{ij} D_i^{-1} E_\gamma^{-5} \rangle$  given in the last column of the table are proportional to the ratio of  $I_\gamma E_\gamma^{-5} Q_J^{-1}$  to the neutron-capture rate. These values of  $\langle \Gamma_{ij} D_i^{-1} E_\gamma^{-5} \rangle$  are seen to be equal within a factor of about 2 for all isotopes in each sample. None of the observed differences are accepted as evidence for real differences, in view of the magnitude of the indicated uncertainties and the possibility that the neutron-shielding action of the outer portions of samples of large diameter is not the same for all isotopes.

### C. Energy Dependence of $M1$ Transitions

The literature contains almost no experimental information and rather little theoretical analysis on the energy dependence of the widths of high-energy  $M1$  transitions. The most commonly used theoretical relationship comes from the single-particle model,<sup>46</sup> which predicts that the  $M1$  width varies as  $E_\gamma^3$ . Recently, Shapiro and Emery<sup>47</sup> have used a two-quasiparticle model to calculate the  $M1$  widths for deformed heavy nuclides. They find for many nuclides that  $\Gamma_{M1} E_\gamma^{-3}$  exhibits a broad peak with a maximum in the neighborhood of 7–8 MeV, depending on the structure of the nucleus involved.

The energy dependences for the widths of  $M1$  transitions observed in our spectra are given in Figs. 15, 23, and 26 of this paper and in Fig. 10 of Ref. 26. Of these, the  $^{168}\text{Er}$  data (Fig. 10 of Ref. 26) are interesting because  $\Gamma_{M1}$  clearly varies more rapidly than  $E_\gamma^3$ , and the  $^{106}\text{Pd}$  data (Fig. 26) are particularly interesting because they provide evidence for a broad peak in the curve of  $\Gamma_{M1} E_\gamma^{-3}$  versus  $E_\gamma$ . The intensity of a line associated with a positive-parity state in  $^{106}\text{Pd}$  results from three components:  $s$ -wave capture followed by  $M1$  radiation,  $s$ -wave capture followed by  $E2$  radiation, and  $p$ -wave capture followed by  $E1$  radiation. In principle, any one of these forms of electromagnetic radiation could be responsible for the abrupt change in the slope of the curve drawn through the positive-parity data in Fig. 26. However, the low intensities of the transitions to the  $0^+$  states at 1705 and 2000 keV show that the  $E2$  and  $E1$  components are not strong enough to explain the observed effect. Thus, we proceed under the assumption that the  $M1$  component is responsible.

The magnitude of the  $M1$  component can be deduced from the middle curve of Fig. 26 by using the observed intensities of the transitions to the  $0^+$  states at 0, 1705, and 2000 keV as a measure of the  $E2$  and  $E1$  components. This is done by solving the simultaneous equations that describe the intensity  $I_2$  of transitions to a  $2^+$  final state and the intensity  $I_0$  of transitions to a  $0^+$  final state. First note that a  $2^+$  state is fed by five initial states whereas a  $0^+$  state is fed by only two. Then, the ideas developed in Sec. III allow one to show that  $I_2$  and  $I_0$  may be written as  $I_2 = 2I_{sM1} + 2I_{sE2} + 5I_{pE1}$  and  $I_0 = I_{sE2} + I_{pE1}$ , where  $I_{sM1}$  is the intensity for  $s$ -wave capture in initial states with a given  $J$  value followed by  $M1$  radiation to a single final state,  $I_{sE2}$  is similarly defined, and  $I_{pE1}$  is the intensity for  $p$ -wave capture in  $1^-$  states followed by  $E1$  transitions to a  $0^+$  state. Now we assume that both  $\Gamma_{E1}$  and  $\Gamma_{E2}$  vary as  $E_\gamma^5$ , as is expected from the giant-resonance model<sup>18</sup> and the single-particle model,<sup>46</sup> respectively, and as is consistent with the data for the three  $0^+$  states. Then the ratio  $I_{sE2}/I_{pE1}$  is equal to a constant  $c$  which is independent of  $\gamma$ -ray energy. With the aid of this ratio, one now finds from the equations for  $I_2$  and  $I_0$  that the intensity of the  $M1$  component is  $2I_{sM1} = I_2 - (2c + 5)(c + 1)^{-1}I_0$ .

The ratio  $c$  may be determined by fitting the observed line associated with the  $0^+$  ground state with a shape calculated from Eq. (10) and broadened with a resolution function of the appropriate width, as is illustrated in Fig. 27. For the reasons discussed in Sec. V D, the uncertainties in this procedure are too large to allow  $c$  to be determined accurately. Nevertheless, the calculations show that  $c$  almost surely falls in the range  $0.2 < c < 0.8$  for the sample involved, and a variation of  $c$  over this range causes relatively little variation in  $(2c + 5)(c + 1)^{-1}$ . Thus, the intensity of the  $M1$  component can be determined fairly well in spite of the uncertainty in the relative strengths of the  $E2$  and  $E1$  components. The curve for  $\Gamma_{M1} E_\gamma^{-3}$  in Fig. 26 (labeled  $M1$ ) was calculated for  $c = 0.5$ , the most probable value.

The most interesting feature of the curve of  $\Gamma_{M1} E_\gamma^{-3}$  versus  $E_\gamma$  for  $^{106}\text{Pd}$  is that it has a giant-resonance-like shape. The energy of the peak (~7.8 MeV) and the width of the resonance (2.5–3.0 MeV) are similar to those calculated by Shapiro and Emery<sup>47</sup> for  $M1$  transitions in heavier, more deformed nuclides.

### D. Widths of $E2$ and $M1$ Transitions

A final state that has the same parity as the target nucleus and a spin that differs by  $\frac{5}{2}$  units can be fed only by  $E2$  radiation when  $p$ -wave capture

may be neglected, as is the case for the thin-absorber samples of gadolinium, holmium, and erbium. Thus, the ratio  $\Gamma_{E1}/\Gamma_{E2}$  may be obtained directly from the measured intensities for the appropriate negative-parity and positive-parity states. The results obtained from our spectra are summarized in Table XVIII.

For  $^{106}\text{Pd}$  the influence of  $p$ -wave capture is important, and hence it is more difficult to determine  $\Gamma_{E1}/\Gamma_{E2}$ . Two different calculational approaches may be followed. One involves a use of the measured intensity  $I_-$  of the line for a negative-parity state and the intensity of the  $s$ -wave component of the line for the  $0^+$  ground state. The main sources of error in the value of  $\Gamma_{E1}/\Gamma_{E2}$  derived from these data are the uncertainty in the value of the  $p$ -wave neutron strength function and the need to infer the intensity  $I_-$  for 9.5-MeV  $\gamma$  rays from the measured intensities at energies below 7.5 MeV; in this extrapolation of  $I_-$  the energy dependence of  $\Gamma_{E1}$  is assumed to be as given by Eq. (16).

The second approach consists of fitting the observed line for the ground-state transition with a calculated shape. Here Eq. (10) is used to calculate the energy dependence for both the  $p$ -wave and  $s$ -wave components, and the ratio of intensities for the two components is adjusted to give a good fit such as the one shown in Fig. 27. The ratio  $I_{pE1}/I_{sE2}$  is directly proportional to  $\Gamma_{E1}/\Gamma_{E2}$ , and the main sources of error in the value of  $\Gamma_{E1}/\Gamma_{E2}$  obtained from the intensity ratio are the uncertainties in the values of the  $s$ -wave and (especially) the  $p$ -wave neutron strength functions. Unfortunately, the measured line shape can be fitted by a fairly wide range of values, so that the strength functions

cannot be determined accurately from the line shape itself.

The values of  $\Gamma_{E1}/\Gamma_{E2}$  obtained in the two alternative ways outlined above are consistent when the  $s$ -wave and  $p$ -wave neutron strength functions are in the neighborhood of  $0.5 \times 10^{-4}$  and  $5 \times 10^{-4}$ , respectively—both reasonable values. This agreement generates confidence in the derived value of  $\Gamma_{E1}/\Gamma_{E2}$ , namely  $45 \pm 10$ . Also, it indicates that the  $\gamma$ -ray strength function  $\langle \Gamma_{ij}/D_i \rangle$  for  $E1$  transitions is roughly the same (within a factor of  $\sim 1.5$ ) for negative-parity and positive-parity initial states.

### E. Fluctuations in Widths

In recent years there have been a number of reports of  $\gamma$ -ray spectra that reveal the presence of specific nuclear-structure effects. Of particular interest for this investigation are the mechanisms (such as the channel resonance capture of Lane and Lynn<sup>48</sup>) that imply that the intensity of a radiative transition should depend on the structure of the final state. If present, such effects should be sensitively revealed by intensity variations in the  $(\bar{n}, \gamma)$  data that cannot be explained by random Porter-Thomas fluctuations.

As was shown in Sec. IV, the observed intensities of most of the high-energy radiative transitions fluctuate about their expected values (as inferred from a smooth energy dependence) to an extent that is consistent with the experimental errors and the Porter-Thomas distribution of partial radiation widths. Thus, we already know that the non-random effects caused by the structure of the final states are small. This matter is examined further in Table III, where the data on the observed scatter in the intensities of  $E1$  transitions are compared with what is expected under the assumption that the transitions between individual states satisfy the Porter-Thomas distribution and that the average intensity is independent of the structure of the final state.

The quantity  $(\Delta I/I)_{\text{PT}}^2$  in Table III is the expected relative variance in the intensity associated with a single transition path when only Porter-Thomas fluctuations are involved; it is calculated in the way outlined in Sec. III C. The quantity  $(\Delta I/I)_{\text{obs}}$  is the *observed* rms scatter for the selected data points plotted in Figs. 15, 21, and 26, and for a similar set of  $^{168}\text{Er}$  data selected because of their apparent reliability and small experimental errors. Note that  $(\Delta I/I)_{\text{obs}}$  is not the precise experimental equivalent of  $(\Delta I/I)_{\text{PT}}$ , since  $(\Delta I/I)_{\text{obs}}$  is influenced by experimental as well as Porter-Thomas errors and since the observed scatter includes the contributions of final states that are fed by both one and two initial states. However, these two complex-

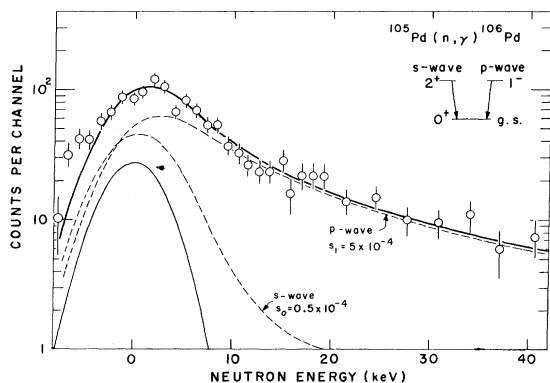


FIG. 27. Curve fit of the line associated with the  $0^+$  ground state in  $^{106}\text{Pd}$ . The diagram in the upper right-hand corner shows the transitions involved. The sample used in the measurements was sample 9 of Table II, and the parameters used in the calculation are those given in Table I; the  $p$ -wave strength function was  $5 \times 10^{-4}$ . The neutron-capture spectra were broadened with the Gaussian resolution function shown at zero neutron energy.

TABLE XVIII. Summary of widths for  $E2$  and  $M1$  transitions. The units for  $k_{E2}$  and  $k_{M1}$  are specified in Sec. V D. Predictions of the single-particle model (Ref. 46) are given in the last line for the case of a nuclide of mass 165. The numbers in parentheses are the factors by which  $\Gamma_{E1}/\Gamma_{E2}$  are uncertain.

Emitting nucleus	Parameters for $E2$ transitions			Parameters for $M1$ transitions			
	$E_\gamma$ (MeV)	$\frac{\Gamma_{E1}}{\Gamma_{E2}}$	$10^9 k_{E2}$	$E_\gamma$ (MeV)	$\frac{\Gamma_{E1}}{\Gamma_{M1} + \Gamma_{E2}}$	$\frac{\Gamma_{E1}}{\Gamma_{M1}}$	$10^3 k_{M1}$
$^{106}\text{Pd}$	9.5	45(1.3)	35	7.7		$4.5 \pm 0.7$	10.6
$^{106}\text{Pd}$				6.8		$8.3 \pm 1.7$	4.5
$^{156}\text{Gd}$	8.2	>85	<31	7.2	$8.0 \pm 0.8$	$8.3 \pm 1.0$	15.0
$^{158}\text{Gd}$	7.7	>120	<23	6.9	$6.7 \pm 0.6$	$6.9 \pm 0.8$	16.1
$^{166}\text{Ho}$	6.2	50(1.7)	58	6.0	$4.9 \pm 0.3$	$5.4 \pm 0.7$	17.8
$^{165}\text{Er}$	...	...		6.0	$7.6 \pm 2.0$	$7.8 \pm 2.2$	12.1
$^{167}\text{Er}$	6.4	>100	<29	5.9	$5.0 \pm 1.2$	$5.2 \pm 1.4$	18.4
$^{168}\text{Er}$	6.8	65(1.7)	46	6.8	$6.7 \pm 0.3$	$7.4 \pm 0.7$	17.2
$^{165}\text{X}$	7.0	944	3.0	7.0		98	1.27

ties in the data work in opposite directions, so that the numerical values of  $(\Delta I/I)_{\text{PT}}$  and  $(\Delta I/I)_{\text{obs}}$  should be approximately equal. Note that they are almost equal for some of the measurements but not for others.

The quantity  $(\Delta I/I)_1^2$  is an experimentally derived relative variance that is intended to be accurately equivalent to  $(\Delta I/I)_{\text{PT}}^2$ . It is obtained as the value of the variance that, when combined with the errors of measurement, gives the same  $\chi^2$  as is obtained for each of the selected sets of data points mentioned in the preceding paragraph; again  $(\Delta I/I)_1$  refers to a single transition path. If the data satisfy our assumptions about randomness and independence of the final state, then  $(\Delta I/I)_1$  should be equal to  $(\Delta I/I)_{\text{PT}}$  within the uncertainties determined by the size of the statistical sample. Clearly, these two quantities are not always in satisfactory agreement, and hence the data do not all satisfy the assumptions. As was argued in Sec. IV A1, the differences probably result from the summing of transitions to unresolved final states.

The quantity  $(\Delta I/I)_2$  is the same as  $(\Delta I/I)_1$  except that it is computed for sets of data from which apparently anomalous members have been removed. The data removed are those discussed in Sec. IV, namely those for the states at 634 and 693 keV in  $^{166}\text{Ho}$ , at 1431, 1542, and 1893 keV in  $^{168}\text{Er}$ , and at 1916 keV in  $^{156}\text{Gd}$ . As shown earlier, most of these lines have anomalously large intensities that are consistent with what is expected from the summing of transitions to unresolved states. The only exception is the line associated with the 1431-keV state in  $^{168}\text{Er}$ , which cannot be explained by summing (if the assignment  $J=3$  is correct) because the observed intensity is lower than expected.

All of the values of  $(\Delta I/I)_2$  are in satisfactory agreement with the theoretical values  $(\Delta I/I)_{\text{PT}}$  if the uncertainty caused by the small size of the sta-

tistical sample is taken into account. This result indicates that the procedure outlined in Sec. III C may be used with confidence to calculate the magnitude of the random fluctuations in the intensities of average-resonance-capture lines.

The good agreement between the values of  $(\Delta I/I)_{\text{PT}}$  and  $(\Delta I/I)_2$  also suggests strongly that our two basic assumptions about the radiation widths are correct. That is, the agreement supports the assumptions (a) that the partial radiation widths obey the Porter-Thomas distribution and (b) that the widths are very insensitive to the structure of the final state. Of course, in principle it would be possible for both assumptions to fail simultaneously in such a way that one failure would counteract the influence of the other. However, if one excludes this unlikely possibility and allows only one or the other assumption to fail, then the data allow one to set qualitative limits on the degree to which each assumption could be in error. In particular, the calculated scatter in the intensities would be detectably smaller than is observed if the distribution of partial radiation widths were a  $\chi^2$  distribution with about two degrees of freedom rather than the Porter-Thomas distribution (one degree of freedom). And the intensity fluctuations caused by the structure of the final state have to be less than about  $\pm 10\%$  (rms) to go undetected. This insensitivity to the nature of the final state raises doubts about the reality of the large variations that have been reported in the average widths of high-energy transitions in several heavy deformed nuclides.

## VI. CONCLUSIONS

The most important result of this investigation is the general one that the average intensities of the high-energy neutron-capture  $\gamma$ -ray transitions in many nuclides are well described by the simple

statistical model introduced as a working hypothesis at the beginning of this paper. This finding permits the average-resonance-capture data to be used with confidence to assign the parities and set limits on the spins of the final states involved.

The examination (Secs. IV and V) of the degree to which the data agree with the statistical model reveal several things that are significant for the use of the average-resonance-capture data in nuclear spectroscopy. The most valuable property is that the average widths of both  $E1$  and  $M1$  transitions in a given nucleus are a smooth function of  $\gamma$ -ray energy and that the random scatter in the measured intensities is determined principally by the Porter-Thomas distribution of partial radiation widths. This behavior is observed not only in the data presented in this paper but also in many other nuclides, including the thoroughly analyzed transitions in the even-even nuclides of cadmium,<sup>49</sup> samarium,<sup>50</sup> hafnium,<sup>51</sup> osmium,<sup>52</sup> and platinum.<sup>7</sup>

An important implication of the regular behavior of the high-energy transitions is that an  $(\bar{n}, \gamma)$  measurement is uniformly sensitive to all states of a given kind in a given range of energy. Thus, the data are complete in the sense that *all* states of a given kind are detected except for those missed because of failure to resolve individual  $\gamma$ -ray lines. This property is extremely valuable, as was shown by the interpretation of the <sup>166</sup>Ho data, and it is unusual, since most nuclear reactions are strongly influenced by the specific nuclear character of the states involved.

Several other properties of the transitions are also useful, though not essential. One of these is that the energy dependence of the widths of  $E1$  transitions is approximately describable in terms of the giant-resonance model outlined in Sec. IV A1. This property allows one to extrapolate average  $E1$  widths reliably from a few known values into an unknown region. Conversely, the lack of a good understanding of  $M1$  transitions is a handicap.

Another useful property of the high-energy transitions is that the ratio  $\langle \Gamma_{ij} D_i^{-1} E_\gamma^{-5} \rangle$  seems to be roughly the same for all nuclides in a given mass range. This property is sometimes useful for isotopic identification and it is essential for a quantitative understanding of the influence of impurities in the sample. Moreover, it implies that the average-resonance-capture spectra are relatively insensitive to impurities. An excellent example of this is a study<sup>49</sup> of <sup>111</sup>Cd( $n, \gamma$ )<sup>112</sup>Cd by means of an  $(\bar{n}, \gamma)$  measurement on a sample of normal cadmium, which yields lines of about the same intensity for <sup>111</sup>Cd( $\bar{n}, \gamma$ ) and <sup>113</sup>Cd( $\bar{n}, \gamma$ ); in contrast, in a thermal neutron-capture measurement on a highly enriched sample of <sup>111</sup>Cd, the lines of interest would be largely obscured by intense lines from

the <sup>113</sup>Cd impurity.

In spite of the insensitivity of the average-resonance-capture spectra to impurity isotopes in the sample, we have found that it is important to use isotopically enriched samples whenever possible. Otherwise, as shown for example by our measurement on a natural gadolinium sample, uncertainties about the isotopic identification of some lines and the increased difficulty of resolving lines prevent the method from being as useful as it can be. In order to obtain a good spectrum with our experimental system, the enriched sample should weigh at least 1 g and a 3-g sample is desirable.

All of our measurements have been carried out with an internal-sample experimental arrangement because of our conviction that it can provide a higher counting rate and lower background than is obtainable with the alternative arrangement in which a beam of neutrons is extracted from the reactor. These presumed advantages of the internal-sample arrangement are gained at the cost of an inflexibility in the way in which the neutron energy is selected and of a limitation to measurements of singles spectra. To some extent the relative merits of the two experimental arrangements may be judged from a comparison between our spectra and those recently reported by Greenwood *et al.*,<sup>53</sup> who have used a very thick filter of scandium to form a beam of neutrons with energies in the neighborhood of 2 keV. The full width of the energy distribution of the 2-keV beam is about 700 eV, so that the effective number of resonances excited is roughly the same as in one of our measurements with a <sup>10</sup>B absorber about 0.2 g/cm<sup>2</sup> thick, as may be seen from the values of  $w_e$  given in Table III. Thus, equivalent spectra obtained in the two alternative ways may be compared. Judging from the results reported to date, the principal advantage of the beam approach is that the sample becomes much less radioactive, and hence large (expensive) quantities of separated isotopes may be used freely. The principal disadvantage is that the spectra obtained are technically inferior to those obtainable with the internal-sample arrangement, as may be judged from a comparison between Fig. 2 of Ref. 53 and Fig. 12 of this paper, which give spectra for similar samples. An important reason for the difference in the quality of the spectra is that a pair spectrometer can be used without a serious loss of counting efficiency for the internal-sample but not for the external-sample arrangement.

Limitations on the usefulness of the average transition intensity may be inferred from the statistical properties of the intensity. For almost all nuclides, spectra of good quality can be measured with a <sup>10</sup>B absorber as thick as 0.5 g/cm<sup>2</sup>. As shown in Table III, such an absorber yields a neu-

tron-capture spectrum whose effective width is about 2000 eV for the typical nucleus, and the relative uncertainty in intensity is roughly  $\Delta I/I \approx (D_i/750)^{1/2}$ . Thus, in order to be able to detect the factor of 2 difference in intensity that is required to obtain information about *spins*, the spacing  $D_i$  must be fairly small – say < 50 eV. This condition is satisfied by almost all even-even and odd-odd product nuclides with  $A < 100$ ; here and later we refer only to those formed by neutron capture, of course. For even-odd nuclides, only states with  $J = \frac{1}{2}$  or  $\frac{3}{2}$  are reached by dipole transitions and, as shown below,  $E1$  and  $M1$  transitions can be distinguished if  $D_i < 200$ . Thus, an average-resonance-capture measurement can be used to obtain information about the spins of states in almost all nuclides with  $A > 100$ .

The *parities* of states fed by dipole transitions can be determined with even greater ease from the intensities of lines in the average-resonance-capture spectra. Since the ratio  $\Gamma_{E1}/\Gamma_{M1}$  is typically 6,  $E1$  transitions in even-odd nuclides can almost always be distinguished from  $M1$  transitions if  $D_i < 200$ , and this condition is satisfied by most even-odd nuclides with  $A > 100$ . Also, the minimum ratio of the intensities for positive-parity states to the intensities for negative-parity states is 3 for the typical even-even or odd-odd nucleus; hence the parity can usually be determined if  $D_i < 100$ , except that  $D_i$  may have to be somewhat smaller if  $75 < A < 140$  because for these nuclides  $p$ -wave capture decreases the ratio of the intensities for positive-parity states to those for negative-parity states.

The limitation  $p$ -wave capture imposes on the usefulness of the average intensity is counterbalanced by the fact that  $p$ -wave capture causes the *shape* of the observed lines to be a measure of the final-state parity. The results for  $^{105}\text{Pd}(n, \gamma)^{106}\text{Pd}$  reported in this paper and similar results for many other nuclides (to be reported later) show that the line shape gives a sensitive and reliable measure of the parity for all nuclides in the range  $73 < A < 139$  if  $D_i$  is less than a few hundred eV. Thus, either the  $\gamma$ -ray intensity or the line shape can be used to determine the parity of states in almost all nuclides with  $A > 100$  and in most even-even and odd-odd nuclides with  $A > 70$ .

In conclusion, the average-resonance-capture method is a powerful new tool for the investigation of low-energy states in nuclides with  $A > 100$ . In favorable circumstances the method is probably capable of detecting and identifying more states than is possible by means of any other single method now in use.

#### ACKNOWLEDGMENTS

The authors are indebted to their colleagues for vital assistance in many phases of this work – to W. V. Prestwich for the development of an excellent pair-spectrometer system, to H. M. Mann and J. J. Baum for supplying Ge(Li) detectors with special characteristics, to J. R. Specht for enthusiastic and skillful technical support in all phases of the work, to J. W. Tippie for the programs used to calculate neutron-capture spectra, and to J. R. Erskine for helpful discussions about rotational bands. We thank them all.

†Work performed under the auspices of the U. S. Atomic Energy Commission.

<sup>1</sup>G. A. Bartholomew, *Ann. Rev. Nucl. Sci.* **11**, 259 (1961).

<sup>2</sup>H. Motz and G. Bäckstrom, in *Alpha-, Beta-, and Gamma-Ray Spectroscopy*, edited by K. Siegbahn (North-Holland Publishing Company, Amsterdam, The Netherlands, 1965), p. 769.

<sup>3</sup>R. E. Chrien, in *Proceedings of the International Symposium on Neutron-Capture Gamma-Ray Spectroscopy, Studsvik, Sweden, 11–15 August 1969* (International Atomic Energy Agency, Vienna, Austria, 1969), p. 627.

<sup>4</sup>L. M. Bollinger, in “Experimental Neutron-Resonance Spectroscopy” (to be published).

<sup>5</sup>C. E. Porter and R. G. Thomas, *Phys. Rev.* **104**, 483 (1956).

<sup>6</sup>This result is obtained by applying Bayes’ theorem on conditional probability in the way outlined by L. M. Bollinger and G. E. Thomas, *Phys. Rev.* **171**, 1297 (1968).

<sup>7</sup>L. M. Bollinger and G. E. Thomas, *Phys. Rev.*

*Letters* **18**, 1143 (1967).

<sup>8</sup>L. M. Bollinger and G. E. Thomas, *Phys. Rev. Letters* **21**, 233 (1968).

<sup>9</sup>G. E. Thomas, D. E. Blatchley, and L. M. Bollinger, *Nucl. Instr. Methods* **56**, 325 (1967).

<sup>10</sup>This detector system was developed under the direction of W. V. Prestwich.

<sup>11</sup>M. G. Strauss, I. S. Sherman, R. Brenner, S. J. Rudnick, R. N. Larsen, and H. M. Mann, *Rev. Sci. Instr.* **38**, 725 (1967).

<sup>12</sup>M. G. Strauss, L. L. Sifter, E. R. Lenkszus, and R. Brenner, *IEEE Trans. Nucl. Sci.* **NS-15** (No. 3), 518 (1968).

<sup>13</sup>R. C. Greenwood, *Phys. Letters* **27B**, 274 (1968).

<sup>14</sup>A concise review of the relationships among the various neutron-resonance parameters used in this paper is given by L. M. Bollinger, in *Nuclear Spectroscopy*, edited by F. Ajzenberg-Selove (Academic Press Inc., New York, 1960), Pt. A, p. 416.

<sup>15</sup>M. D. Goldberg *et al.*, Brookhaven National Laboratory Report No. BNL-325, 1966 (unpublished), 2nd ed.,

Suppl. No. 2, Vols. II B and II C.

- <sup>16</sup>K. K. Seth, Nucl. Data A2, 299 (1966).
- <sup>17</sup>H. T. Motz *et al.*, Phys. Rev. 155, 1265 (1967).
- <sup>18</sup>P. Axel, Phys. Rev. 126, 671 (1962).
- <sup>19</sup>N. Rosenzweig, Nucl. Phys. A118, 650 (1968).
- <sup>20</sup>E. Hayward, in *Nuclear Structure and Electromagnetic Interactions*, edited by N. MacDonald (Plenum Press, Inc., New York, 1965), p. 141.
- <sup>21</sup>J. R. Erskine and W. W. Buechner, Phys. Rev. 133, 370 (1964).
- <sup>22</sup>G. L. Struble, J. Kern, and R. K. Sheline, Phys. Rev. 137, 772 (1965).
- <sup>23</sup>J. P. Davidson, *Collective Models of the Nucleus* (Academic Press Inc., New York, 1968).
- <sup>24</sup>W. Ogle, S. Wahlborn, R. Peipenbring, and S. Fredriksson, Los Alamos Scientific Laboratory Report No. LA-DC-11253, 1970 (unpublished).
- <sup>25</sup>R. K. Sheline *et al.*, Phys. Rev. 143, 857 (1966); also, private communication. The authors are indebted to Professor Sheline for critical comments concerning their interpretation of the <sup>166</sup>Ho data.
- <sup>26</sup>L. M. Bollinger, in *Proceedings of the International Symposium on Nuclear Structure, Dubna, 1968* (International Atomic Energy Agency, Vienna, Austria, 1968), p. 317. The argument concerning selection rules for the ( $n, \gamma$ ) reaction is outlined in the discussion following the paper.
- <sup>27</sup>W. Michaelis *et al.*, Nucl. Phys. A143, 225 (1970).
- <sup>28</sup>R. A. Harlan and R. K. Sheline, Phys. Rev. 168, 1373 (1968).
- <sup>29</sup>W. Michaelis, F. Weller, and H. Ottmar, Nucl. Phys. A150, 161 (1970).
- <sup>30</sup>H. R. Koch, Z. Physik 192, 142 (1966).
- <sup>31</sup>R. A. Harlan and R. K. Sheline, Phys. Rev. 160, 1005 (1967).
- <sup>32</sup>A. A. Abdurazakov, K. Ya. Gromov, V. Zvol'ska, T. A. Islamov, and H. Strusny, Joint Institute for Nuclear Research Report No. P6-4889, 1970 (to be published).
- <sup>33</sup>L. V. Groshev, A. M. Demidov, V. A. Ivanov, V. N. Lutsenko, and V. I. Pelekhov, Izv. Akad. Nauk SSSR Ser. Fiz. 26, 1119 (1962) [transl.: Bull. Acad. Sci. USSR, Phys. Ser. 26, 1127 (1962)].
- <sup>34</sup>R. R. Spencer, K. T. Faler, and R. A. Harlan, Idaho Nuclear Report No. IN-1218, 1968 (unpublished).
- <sup>35</sup>A. Bäcklin *et al.*, in *Proceedings of the International Symposium on Neutron-Capture Gamma-Ray Spectroscopy, Studsvik, Sweden, 11-15 August 1969* (International Atomic Energy Agency, Vienna, Austria, 1969), p. 147.
- <sup>36</sup>L. V. Groshev *et al.*, Nucl. Data A5, 175 (1968).
- <sup>37</sup>C. M. Lederer, J. M. Hollander, and I. Perlman, *Table of Isotopes* (John Wiley & Sons, Inc., New York, 1967), 6th ed.
- <sup>38</sup>R. C. Greenwood and C. W. Reich, Idaho Nuclear Report No. IN-1218, 1968 (unpublished); private communication.
- <sup>39</sup>J. H. E. Mattauch, W. Thiele, and A. H. Wapstra, Nucl. Phys. 67, 32 (1965).
- <sup>40</sup>D. L. Dittmer and W. W. Daehnick, Phys. Rev. 188, 1881 (1969).
- <sup>41</sup>G. A. Bartholomew, L. V. Groshev *et al.*, Nucl. Data A3, 367 (1967).
- <sup>42</sup>C. Coceva, F. Corvi, P. Giacobbe, M. Stefanon, and G. Carraro, in *Proceedings of the International Symposium on Neutron-Capture Gamma-Ray Spectroscopy, Studsvik, Sweden, 11-15 August 1969* (International Atomic Energy Agency, Vienna, Austria, 1969), p. 675.
- <sup>43</sup>G. E. Thomas and L. M. Bollinger, Bull. Am. Phys. Soc. 14, 515 (1969).
- <sup>44</sup>H. Bakhru, R. I. Morse, and I. L. Preiss, Can. J. Phys. 47, 419 (1969).
- <sup>45</sup>P. Axel, K. Min, N. Stein, and D. C. Sutton, Phys. Rev. Letters 10, 299 (1963).
- <sup>46</sup>For example, see D. H. Wilkinson, in *Nuclear Spectroscopy*, edited by F. Ajzenberg-Selove (Academic Press Inc., New York, 1960), Part B, p. 852. In the equations derived from the single-particle model, we use the value  $D_0 = 16.5$  MeV obtained by R. T. Carpenter, Argonne National Laboratory Report No. ANL-6589, 1962 (unpublished). See also Ref. 26.
- <sup>47</sup>C. S. Shapiro and G. T. Emery, Phys. Rev. Letters 23, 244 (1969).
- <sup>48</sup>A. M. Lane and J. E. Lynn, Nucl. Phys. 17, 563 (1960).
- <sup>49</sup>R. K. Smither, D. J. Buss, L. M. Bollinger, and G. E. Thomas, Bull. Am. Phys. Soc. 14, 513 (1969).
- <sup>50</sup>R. K. Smither and D. J. Buss, Bull. Am. Phys. Soc. 15, 86 (1970).
- <sup>51</sup>D. L. Bushnell, R. K. Smither, and D. J. Buss, Bull. Am. Phys. Soc. 15, 524 (1970).
- <sup>52</sup>G. E. Thomas and L. M. Bollinger, Bull. Am. Phys. Soc. 15, 549 (1970).
- <sup>53</sup>R. C. Greenwood, R. A. Harlan, R. G. Helmer, and C. W. Reich, in *Proceedings of the International Symposium on Neutron-Capture Gamma-Ray Spectroscopy, Studsvik, Sweden, 11-15 August 1969* (International Atomic Energy Agency, Vienna, Austria, 1969), p. 607.